General Disclaimer

One or more of the Following Statements may affect this Document

- This document has been reproduced from the best copy furnished by the organizational source. It is being released in the interest of making available as much information as possible.

- This document may contain data, which exceeds the sheet parameters. It was furnished in this condition by the organizational source and is the best copy available.

- This document may contain tone-on-tone or color graphs, charts and/or pictures, which have been reproduced in black and white.

- This document is paginated as submitted by the original source.

- Portions of this document are not fully legible due to the historical nature of some of the material. However, it is the best reproduction available from the original submission.

Produced by the NASA Center for Aerospace Information (CASI)

NASA CR-134984

NUMERICAL CALCULATION OF THE INTERNAL FLOW FIELD IN A CENTRIFUGAL COMPRESSOR IMPELLER

FINAL REPORT

REPORT NO. SR-27

DECEMBER 1975

(NASA-CR-134984) NUMERICAL CALCULATION OF THE INTERNAL FLOW FIELD IN A CENTRIFUGAL COMPRESSOR IMPELLER Final Report (Thermo Mechanical Systems Co., Canoga Park) 100 p HC $5.00 CSCL 20D G3/34

N76-22495

Unclas 27834

by

Leonard Walitt

James L. Harp, Jr.

C. Y. Liu

MAY 1976 RECEIVED NASA STI FACILITY INPUT BRANCH

Prepared For

NATIONAL AERONAUTICS AND SPACE ADMINISTRATION

Lewis Research Center

21000 Brookpark Road

Cleveland Ohio, 44135

MAY 1976 RECEIVED NASA STI FACILITY INPUT BRANCH

Contract No. NAS3-18016

THERMO MECHANICAL SYSTEMS COMPANY
7252 Remmet Avenue
Canoga Park, California 91303

TABLE OF CONTENTS

SECTION		PAGE
	SUMMARY	ii
1.0	INTRODUCTION	1
2.0	SYMBOLS	2
3.0	BACKGROUND	4
4.0	FORMULATION OF IMPELLER PROBLEM	7
5.0	DERIVATION OF THE INTEGRAL CONTINUITY EQUATION	13
6.0	TRANSITION AND TURBULENCE	16
7.0	RADIAL IMPELLER PROBLEM	25
8.0	BACKSWEPT IMPELLER PROBLEM	50
9.0	CONCLUDING REMARKS	81
10.0	REFERENCES	82
	APPENDICES: A	86
	B	92

SUMMARY

An iterative numerical method has been developed for the calculation of steady, three-dimensional, viscous, compressible flow fields in centrifugal compressor impellers. The computer code, which embodies the method, solves the steady three-dimensional, compressible Navier-Stokes equations in rotating, curvilinear coordinates. The solution takes place on blade-to-blade surfaces of revolution which move from the hub to the shroud during each iteration.

Numerical calculations were made for two centrifugal impellers, one with radial blades and the other with backswept blades. The radial impeller operated in a laminar Reynolds number regime. The backswept impeller problem was used to check out the turbulence model incorporated in the code. A large vortex was calculated on the suction blade surface of the radial impeller in the region of the discharge; such a vortex is qualitatively in agreement with observations. The backswept rotor calculation did not indicate an impeller separation. No conclusions can be drawn with regard to the effectiveness of backsweep in reducing or eliminating flow separation, because the radial impeller was calculated for laminar flow at a very low Reynolds number (5000), whereas the backswept impeller problem was calculated for turbulent flow conditions with the turbulence model operational. Contour plots are presented to show the calculated static pressure in the blade-to-blade channel. Relative velocity vector plots on various blade-to-blade surfaces show significant differences with inviscid potential flow solutions in common industry usage for centrifugal compressor design. It is concluded the viscous Navier-Stokes solution for flow fields in centrifugal compressors represents a significant advancement in the ability to analyze these complex types of turbomachinery.

1.0 INTRODUCTION

The principal objective of this research effort is to develop a computer program to calculate the three-dimensional, viscous, compressible flow field in blading passages of turbomachinery. At present the computer program is being applied to the rotating impeller of centrifugal compressors.

This submittal is a report on the work which has been completed in Phase I of a two phase program of research and development. Three main tasks have been completed in Phase I. They are as follows:

1. An impeller computer code was developed and debugged.
2. A radial centrifugal impeller problem was solved.
3. A backswept centrifugal impeller problem was solved.

Phase II of this research effort is comprised of two additional principal tasks.

4. To speed-up the computer code of Phase I by a factor between 3 and 5.
5. To revise the computer code of Phase I, which calculates the flow field on blade-to-blade surfaces, to calculate the flow field on cross-sectional surfaces.

The importance of the cross-sectional calculation is discussed in Section 4.0.

2.0 SYMBOLS

C_p	Heat Capacity at Constant Pressure
C_v	Heat Capacity at Constant Volume
E	Specific Internal Energy
H	Thermodynamic Heat Function or Enthalpy
h_x	Metrics of Transformation
h_y	Metrics of Transformation
h_z	Metrics of Transformation
$\underline{i}$	Unit Vector of Curvilinear Coordinate x
$\underline{i}_1$	Unit Vector of Rotating Cartesian Coordinate of x_1
$\underline{i}_2$	Unit Vector of Rotating Cartesian Coordinate of x_2
$\underline{i}_3$	Unit Vector of Rotating Cartesian Coordinate of x_3
$\underline{j}$	Unit Vector of Curvilinear Coordinate y
J	Index Specifying Streamlike-lines on blade-to-blade Surface
K	Index Specifying Potential-like-lines on Blade-to-blade surface
$\underline{k}$	Unit Vector of Curviliner Coordinate z
$\tilde{K}_s$	Von Karman's Constant
M	Momentum
m	Mass
n	Time Index for Finite Difference equation
P	Pressure
R_o	Maxium Radius of the Impeller (at the exit)
r	Radial Coordinate which together with $x_3$form a Cylindrical Coordinate System
S_x	Grid Velocity Component along x Direction
S_y	Grid Velocity Component along y Direction
T_{ij}	Total Laminar Stress Tensor
t	Time
u	Particle Velocity Component along x Direction
$\underline{u}$	Particle Velocity Vector
U_{oo}	Speed of March along z Direction
V	Particle Velocity Component along y Direction
W	Particle Velocity component along z Direction
$W'=W-U_{oo}$	Velocity along z on a Galilean Frame which moves with a Constant Speed U_{oo} along z with respect to the laboratory frame
X	Curvilinear Coordinate along Azimuthal Direction

X_1 Coordinate Axes of Rotating Cartesian Coordinate which Rotate about Axial Axis X_3 with Speed w

X_2 Coordinate Axes of Rotating Cartesian Coordinate which Rotate about Axial Axis X_3 with Speed w

X_3 Axial Coordinate

Y Curvilinear Coordinate along Streamwise Direction (from inlet to discharge)

Z Curvilinear Coordinate or Marching Direction (from hub to shroud)

Symbols in Greek Letters

γ Heat Capacity Ratio C_p/C_v

δ Boundary Layer Thickness

δ_i^* Incompressible Displacement Thickness

ϵ Eddy Viscosity

μ Molecular Viscosity Coefficient

ν Kinematic Viscosity Coefficient

ω Rotation Velocity of Impeller

σ_{ij} Total Stress Tensor

τ_{ij} Reynold Stress Tensor

α Pressure Blade Surface Meridional Angle

β Local Flow Angle Between Pressure Blade Surface and Meridional plane

ρ Density

τ_ω Shearing Stress at Wall

λ Viscosity Coefficient for the Deviatoril Strain $= -\frac{2}{3}\mu$

θ Azimuthal Coordinate Angle, together with r and X_3 form cylndrical coordinate system

3.0 BACKGROUND

In recent years, considerable effort has been spent in solving the time-dependent, compressible, Navier-Stokes equations for systems with plane two-dimensional and/or axial symmetry [1,2,3,5,6,7]. A single numerical method was used to solve these two-dimensional and/or axisymmetric problems. The numerical method* is an explicit time marching scheme in two spatial dimensions. Details of the method are presented in References 4 and 7.

In 1969, under sponsorship of NASA Ames Research Center, a research effort was initiated to apply the above time-dependent, two-dimensional method to solve steady flow problems in three spatial dimensions. The basic idea was based on the Equivalence Principle [8], which states that for slender bodies at hypersonic speeds the three-dimensional steady equations of motion for inviscid flow reduce identically to unsteady equations in two dimensions.

This principle was extended in an ad hoc manner to a viscous flow through a model which permits viscous cross flow together with inviscid axial flow. Figure 1 shows an ogive-cylinder body at angle-of-attack with respect to the freestream flow direction; leeward vortices are also indicated in the figure. The axial coordinate z was made proportional to a time-like-variable, t, according to the relation

$$z = U_\infty t \qquad (1)$$

where U_∞ is the freestream speed. The two-dimensional Navier-Stokes equations were solved in cross-sectional planes normal to the system's axis. The cross section planes were moved at freestream speed from the leading edge to the trailing base of the body. The time-dependent flow field at each cross-sectional plane corresponded to the steady flow at the z coordinate given by Equation (1). Since the leeward vortices of Figure 1 have axes which are almost parallel to the z axis, the cross-sectional

---

* The numerical method was originally developed by Trulio.

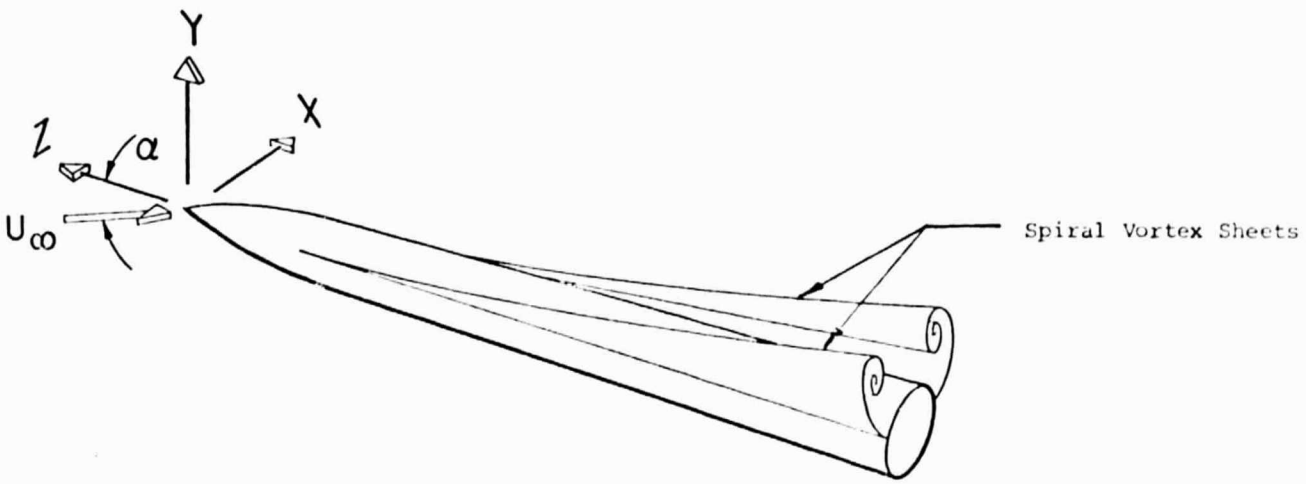

FIGURE 1: Flow field about an axisymmetric body at angle of attack; calculation takes place in (x,y) cross-sectional planes; the z-direction denotes the system's axis.

planes of calculation contain these vortices. Although all axial effects were neglected, this numerical procedure did calculate leeward vortices and produced other flow field results which were generally in accord with experiment [9].

Subsequent to the above research effort, a new study was launched, under NASA Ames Research Center sponsorship, whereby axial effects were incorporated in the numerical procedure and a numerical solution to the full Navier-Strokes equations were generated by iteration. A one-dimensional, time-dependent radial computer code was used to solve for the steady, viscous, compressible, supersonic flow field about a cone-cylinder-flare body at zero angle of attack. In three iterations the calculated boundary layer and shock wave structure converged. After five iterations a recirculation region formed at the cylinder-flare junction. Although the computed recirculation region was much smaller than measured, comparisions of calculated shock structure and boundary layer results with experimental data and boundary layer theory predictions were satisfactory*.

The above axisymmetric computer code was then revised to solve for two-dimensional time-independent flow fields. Trulio and Yeung solved for the supersonic viscous, compressible flow field in a ramp-compression corner**. As in the case of the cone-cylinder-flare junction, the iterative method did not accurately predict the recirculation region formed at the shock-wage-boundary layer interaction.

The iteration procedure employed for the axisymetric and two-dimensional flows, described above, was completely reformulated to account for boundary layer separation and the subsequent evolution of a recirculation regim. The re-formulated iteration procedure was then applied to the impeller of a centrifugal compressor in this research effort. Formulation of the iteration procedure for the impeller problem is discussed in the next section.

---

*Walitt, L., "Computation of Steady Axisymmetric Flow Using a One-Dimensional Time Dependent Method, "Applied Theory Report ATR-74-16-1, August 1974, to be published as a NASA Contractor Report.

**Truilo, J.G., and Yeung, H.W., "Iterative Solution of the Equations for Steady Viscous Compressible Flow Based on Similitude," Aerospace Research Laboratory, Report No. ARL74-0138, 1974.

4.0 FORMULATION OF IMPELLER PROBLEM

A set of finite difference analogs of the full three-dimensional, compressible, Navier-Stokes equations has been developed and programmed. In addition to three-dimensionality and compressibility, the following effects are included:

1. Centrifugal Force
2. Coriolis Force
3. Transition and Turbulence
4. Arbitrary Impeller Geometry
5. Impeller Tip Clearance

A solution to these finite difference equations is obtained in the following manner. For the radial impeller, an inviscid flow field was generated by the method of Reference 10. For the backswept impeller, an inviscid flow field was generated by the method of Reference 39. Starting from the known inviscid solution, the viscous effects are calculated through iteration. Certain terms of the finite difference equations (FDE) are evaluated from the inviscid solution and other terms are evaluated directly. Terms evaluated from the inviscid solution are designated "elliptic source terms", while those evaluated directly are designated, "parabolic terms".

The distribution of the elliptic source terms and parabolic terms in the FDE depends on the mode of marching. At present two modes of marching are contemplated.

1. The FDE are solved on blade-to-blade surfaces which move from the hub to the shroud.
2. The FDE are solved on cross-sectional surfaces which move from the inducer to discharge.

Each method of marching results in its own set of elliptic source terms and parabolic terms.

For illustrative purposes we start with a schematic of a typical impeller for a centrifugal compressor shown in Figure 2. In the blade-to-blade mode of marching, the computation takes place on a blade-to-blade surface, which extends from inducer to the discharge, and moves from the hub to the shroud during an iteration. The darkened surface of Figure 2 is the hub blade-to-blade surface. The blade-to-blade method of marching is

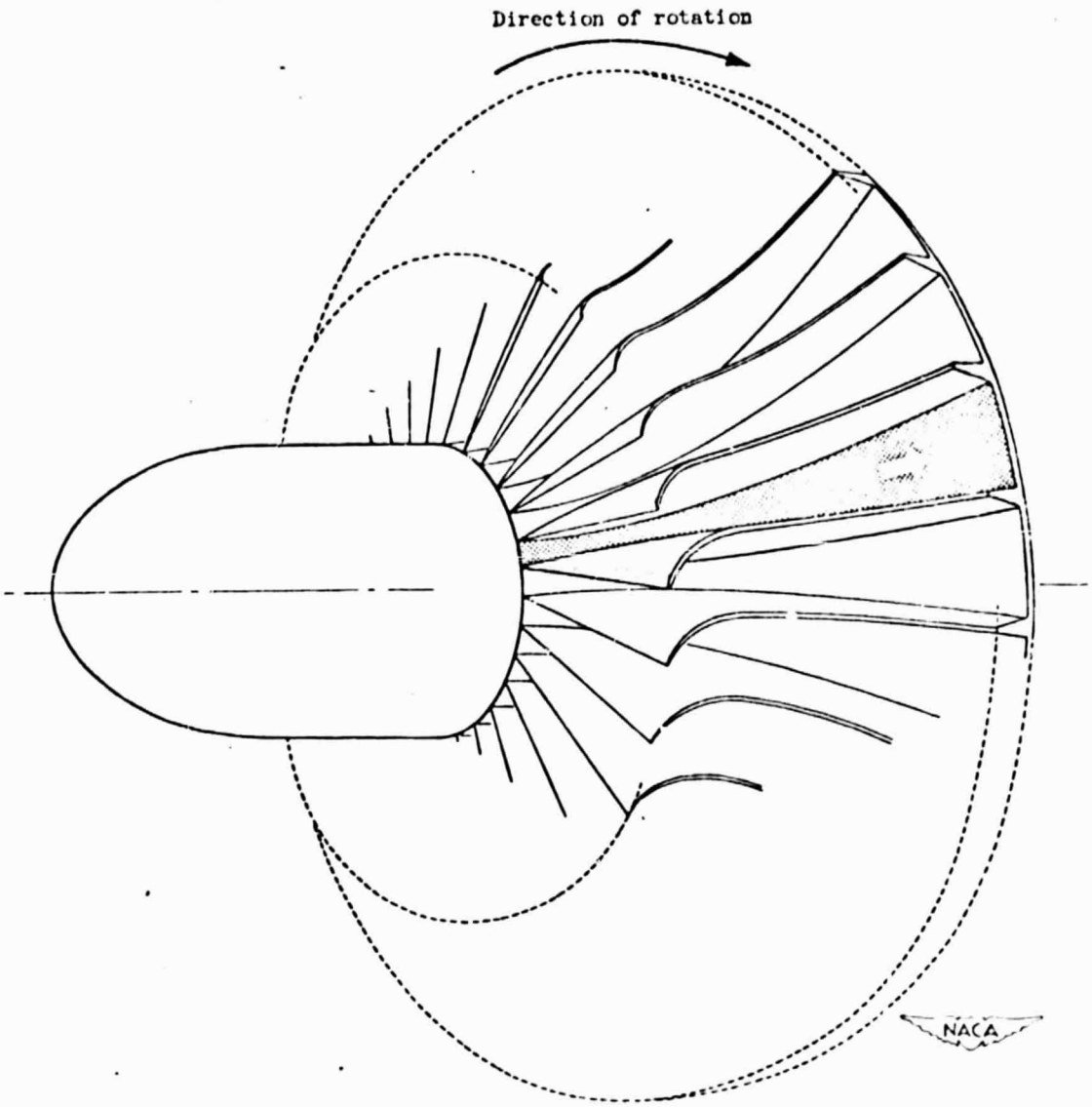

FIGURE 2: PASSAGE BETWEEN BLADES IN IMPELLER OF TYPICAL CENTRIFUGAL COMPRESSOR.

illustrated in the blade passage schematic shown in Figure 3. The x, y, and z coordinates of Figure 3 represent a left handed orthogonal, curvilinear coordinate system. The z - direction is proportional to the time-like-variable, t, with the calculation taking place in the (x,y) blade-to-blade surfaces. The (x,y) blade-to-blade surfaces move from the hub to the shroud of the impeller. This mode of marching accounts for two very important fluid mechanical effects that occur in impellers.

1. Upstream influence effects -

The flow is subsonic relative to the moving blades; hence, downstream conditions influence upstream conditions. Since each blade-to-blade surface extends from inducer to discharge, the downstream flow can influence the upstream flow as the blade-to-blade surface moves from the hub to shroud.

2. Blade boundary layer separation -

Separations, which occur on the blade surfaces, produce vortices whose axes are normal to the blade-to-blade surfaces. Thus, the vortices themselves are contained in the blade-to-blade surface and are easily calculable.

The cross-sectional mode of marching is analogous to the body-at-angle-of-attack problem discussed in Section 3.0. We march down the channel, from the inducer to discharge, in cross-sectional surfaces normal to the hub surface. A schematic of the blade passage with the cross-sectional surfaces indicated is presented in Figure 4. The z-coordinate, which varies with time, is now normal to the (x,y) cross-sectional surface of Figure 4. The (x,y) cross sectional surfaces move from the inducer to the discharge of the impeller. This mode of marching accounts for three additional fluid mechanical effects that occur in impellers.

4. Channel corner vortices

At the junctions of the blades and the hub, vortices usually form whose axes are generally normal to the cross-sectional surfaces; hence, the corner vortices would be contained in these surfaces and are easily calculable.

5. Shroud effects -

Relative to the blades, the shroud imposes a moving boundary condition. The effects of this moving boundary condition may induce separation in the neighborhood of the shroud. This separation is calculable in cross-sectional surfaces since each surface contains the shroud vortices.

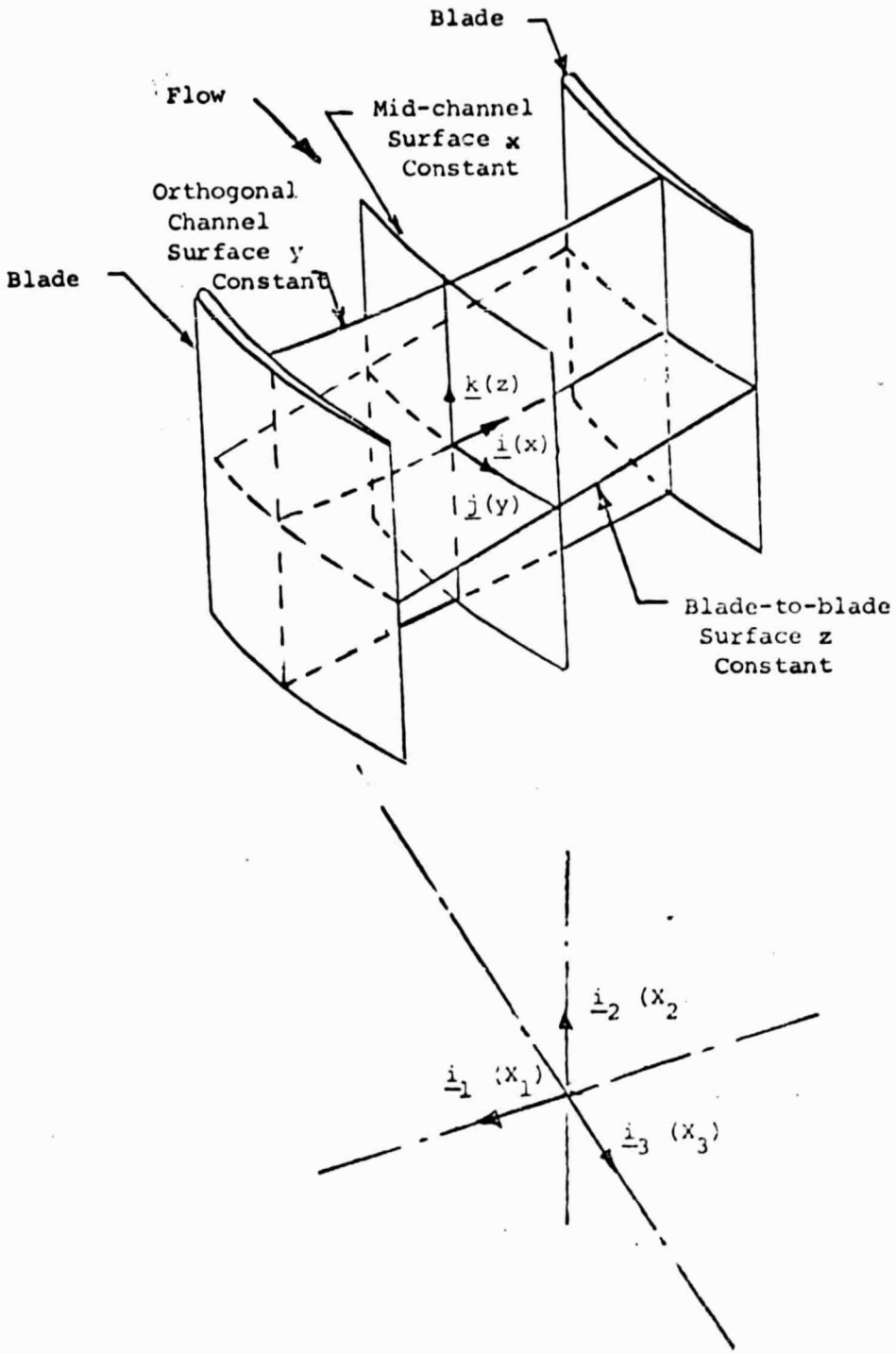

FIGURE 3 Revised orthogonal surfaces in the channel of a centrifugal impeller which define the curvilinear coordinates x, y, and z; surface of calculation is the blade-to-blade surface z constant.

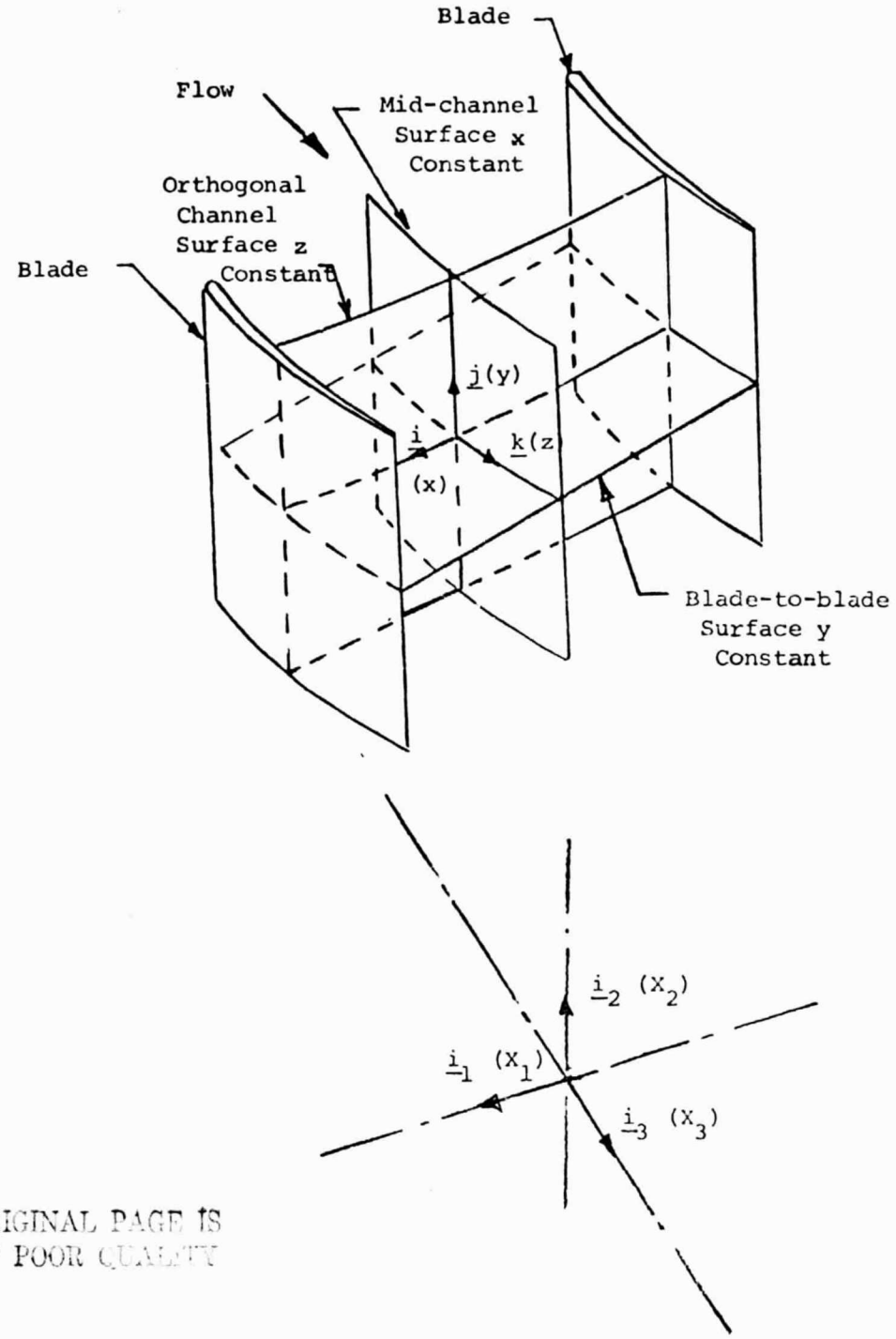

ORIGINAL PAGE IS
OF POOR QUALITY

FIGURE 4. Orthogonal surfaces in the channel of a centrifugal impeller which define the curvilinear coordinates x, y, and z; surface of calculation is the orthogonal surface z constant.

6. Blade tip clearance effects -

Since the shroud and blade tip are contained in each cross-sectional plane, spillage in the tip clearance region is calculable in this mode of marching

To properly solve for an impeller flow field, an iteration procedure with both modes of marching is required. The procedure is as follows. Starting from an inviscid solution as the "zeroth" iterate, we determine the first viscous iterate by marching in blade-to-blade surfaces which move from the hub to the shroud. Based on the first iterate we determine a second viscous iterate by marching in cross-sectional planes which move from the inducer to the discharge. In this way the six principal impeller fluid-mechanical effects, described above, can be accounted for. The second iterate will be a complete solution to the three-dimensional, compressible, Navier-Stokes equations for flow in a centrifugal impeller.

The blade-to-blade mode of marching has been developed in Phase I of this research effort. The blade-to-blade results generated are the subject of this report.

5.0 DERIVATION OF THE INTEGRAL CONTINUITY EQUATION

In this section the integral continuity equation solved on the (x,y) blade-to-blade surface is derived. This derivation is presented to illustrate the actual elliptic source terms and the parabolic terms of the equations of motion. The equations of motion in rotating, orthogonal, curvilinear, Eulerian coordinates x, y, and z are presented in Appendix A.

The steady three-dimensional equations of Appendix A, in Eulerian coordinates x, y, z, are transformed to (x,y,t) space according to the following relations:

$$z = U_\infty t, \quad \frac{\partial}{\partial z} = \frac{1}{U_\infty} \frac{\partial}{\partial \tau}, \quad w = U_\infty + w' \tag{2}$$

where t is a time-like-variable, U is the velocity of the blade-to-blade surface, w is the velocity component in the z-direction, and w' is the velocity in the z-direction. Equations (2) represent a mathematically convenient transformation and lead to a compact set of integral relations; however, they are somewhat non-physical in that the variable t may no longer be time-like, having the units z/U .

The conseravation of mass for steady motion relative to the rotating curvilinear coordinates (x,y,z) is (Appendix A) as follows:

$$\frac{\partial}{\partial z}(\rho w h_x h_y) + \frac{\partial}{\partial x}(\rho u h_y h_z) + \frac{\partial}{\partial y}(\rho u h_z h_x) = 0 \tag{3}$$

where ρ is the density, u the x-velocity component, v the y-velocity component, and (h_x, h_y, h_t) are the transformation metrics.

According to Equations (2) the continuity equation becomes:

$$\frac{\partial}{\partial t}(\rho h_x h_y) + \frac{\partial}{\partial x}(\rho u h_y h_z) + \frac{\partial}{\partial y}(\rho v h_z h_x) = -\frac{1}{U_\infty}\frac{\partial}{\partial t}(\rho w' h_x h_y) \tag{4}$$

The left-hand-side of Equation (4) closely resembles the continuity equation for unsteady flow in the (x,y) plane. The transformation metrics h_x, h_y, h_z on the left-hand-side account for the fact that the flow is not planar but

occurs on a curved surface. The term on the right-hand-side of Equation (4) represents a source term which accounts for the variation of axial velocity w from the constant reference velocity. This term must be considered known in the iteration process and is evaluated from the previous iterate in each successive iteration.

Equation (4) is formulated in the rotating, Eulerian coordinates x,y,t, however, the calculational process takes place on the (x,y) blade-to-blade surface (Figure 3) which distorts with time t according to the shape of the blade surfaces. Hence, we are really interested in the continuity equation in a generalized coordinate system ξ, η, τ, where

$$\begin{aligned} t &= \tau \\ x &= f(\xi, \eta, \tau) \\ y &= g(\xi, \eta, \tau) \end{aligned} \tag{5}$$

The transformed continuity relation in ξ, η, τ space, which is derived in Appendix B, is presented below.

$$\frac{\partial}{\partial t}\int_A \rho h_x h_y dA + \int_C \rho(\underline{q}-\underline{q}_s)\cdot\hat{n}dC - \frac{1}{U_\infty}\int_C \rho w' \underline{q}_s \cdot \hat{n} dC = -\frac{1}{U_\infty}\int_A \rho w' h_x h_y dA \tag{6}$$

where

$$\underline{q} = u h_y h_z \underline{i} + v h_x h_z \underline{j} \tag{7}$$

$$\underline{q}_s = S_x h_y h_z \underline{i} + S_y h_x h_z \underline{j} \tag{8}$$

, and dA = dxdy, A corresponds to the area in the (x,y) plane contained within the region bounded by the closed curve C, $\hat{n}$ is the unit normal to the curve C in the (x,y) plane, S_x is the coordinate velocity in direction X ($S_x = \frac{\partial x}{\partial t}$) and S_y is the coordinate velocity in direction y ($S_y = \frac{\partial y}{\partial t}$). Equations (6) to (8) represent the conservation of mass theorem in terms of area integrals in the (x,y) plane and line integrals evaluated on a curve c in the (x,y)

plane. The curvilinear effects are accounted for by the metrics h_x, h_y, h_z and their derivatives. The term on the right-hand-side of Equation (6) is an elliptic source term and the second and third terms on the left-hand-side of Equation (8) are parabolic terms.

6.0 TRANSITION AND TURBULENCE

In this section various models of transition and turbulence are investigated and the proper ones are selected for incorporation into impeller computer code. Subsection 6.1 deals with the turbulent models, Subsection 6.2 concerns the mixing length theory, and separation is discussed in Subsection 6.3, and Subsection 6.4 considers transition.

6.1 Turbulent Models

With the advance of high-speed computers, turbulent flow problems have become amenable to numerical studies in the past decade. The development of turbulent models has contributed substantially to these studies. Though their progress is still in a preliminary stage, there is no shortage in the supply of models. The difficulty, from a user's point of view, is to select an appropriate model for his particular problem. All models of turbulence are supposed to be general and few cross comparisons between models are available. However, at the present time there is no definitive verdict as to the best turbulence model to employ. Thus a good rule in selection seems to be "the simpler the better".

The adoption of models for turbulence naturally rules out the relatively more fundamental approach via statistical theory, which might be academically pleasing but unrealistic in engineering applications. In general, turbulence modelling is divided into two classes: those described by one algebric relation, such as the mixing length hypothesis, and those described by one or more differential equations governing some quantity like turbulence energy, turbulence vorticity or shearing stress. There are numerous examples in the latter class, generally referred to as the transport model, for example the classical Kolmogorov model (1942)[11] and recently the Saffman model (1970)[12] In adopting such a model, one must solve, in addition to the conservation laws, several differential equations from which turbulence stresses are determined. Limited success can be claimed in application of the transport models; they all seem to do quite well in simple problems like turbulent boundary layers with small pressure gradients.

Let us present herein the Saffman transport model for illustration. The model contains two variables: the energy density e and a pseudo-vorticity Ω, which are assumed to satisfy the following non-linear diffusion equations.

$$\frac{\partial}{\partial t}(\bar{\rho} e) + \frac{\partial}{\partial x_j}(\bar{\rho} \bar{u}_j e) = \left[\alpha^* (2 S_{ij} S_{ij})^{1/2} - \beta^* \rho \Omega\right] \bar{\rho} e + \frac{\partial}{\partial x_j}\left[(\mu + \sigma^* e/\Omega)\frac{\partial e}{\partial x_j}\right] - \frac{2}{3}\bar{\rho} e \frac{\partial u_k}{\partial x_k} \tag{9}$$

$$\frac{\partial}{\partial t}(\bar{\rho}\Omega^2) + \frac{\partial}{\partial x_j}(\bar{\rho} \bar{u}_j \Omega^2) = \left[\alpha \left\{\left(\frac{\partial \bar{u}_i}{\partial x_j}\right)\left(\frac{\partial \bar{u}_i}{\partial x_j}\right)\right\}^{1/2} - \beta \bar{\rho} \Omega\right] \bar{\rho} \Omega^2 + \frac{\partial}{\partial x_j}\left[(\mu + \frac{\sigma e}{\Omega})\frac{\partial \Omega^2}{\partial x_j}\right] \tag{10}$$

where: t = time,

x_j = Cartesian coordinates (j = 1,2,3)

$\bar{\rho}$ = mean density

u_j = mean velocity components in the j-th direction

μ = molecular viscosity coefficient

S_{ij} = mean rate of strain tensor

The numbers α, α^*, β, β^*, σ, σ^*, ξ are assumed by the model to be universal constants.

$\sigma = \sigma^* = 1/2$

$\alpha^* = 0.3$

$\beta^* = \alpha^{*2}$

$5/3 \leq \frac{\beta}{\beta^*} \leq 2$

$\alpha = \alpha^*(\frac{\beta}{\beta^*} - 4\sigma \frac{\tilde{K}^2}{\alpha^*})$

$\xi = 2.5$, based on experimental data,

and $\tilde{K}_s$ the Karman constant.

Equations (9) and (10) are integrated with an appropriate set of boundary conditions (which are not trivial) to yield e and Ω . The eddy viscosity ε is related to e and Ω by

$$\varepsilon = \frac{e}{\Omega} \quad . \tag{11}$$

Saffman's model is but one of the many available schemes governed by two equations; some of the others are Chou (1945)[13], Harlow-Nakayama (1968)[14] Jones-Launder (1972)[15] Ng-Spalding (1972)[16] etc. They all have a set of empirical constants, some even parametric functions. The complexity of the mathematical system and the uncertainty in those constants are inherent with all the models. Moreover, a set of non-linear diffusion equations generally introduces a new time scale in the computation, which is often substantially smaller than the convective or diffusive time scale for laminar type computation. The two-point boundary value problem also poses a tedious numerical task. However, the advantage in this kind of turbulence modelling is also clear; they all attempt to depict the physics of turbulence transport, generation, dissipation and diffusion. In addition, some models (such as Saffman's) show the correct analytical behaviour near the wall (as demanded by the law of wall). The predictive capabilities for incompressible boundary layer flows by those models are thoroughly established. Turbulent flows in more than two spatial dimensions, including separation, compressibility, rotational effects, and containing boundary layers interaction with shock waves have not been subject to examination by those models*. In short, the turbulence models, as promising as they are, have yet to be thoroughly tested by problems more complex than plane boundary layer flows.

In view of the three dimensionality of the compressor problem, the desired economy in computation, and the added degree of complication in

---

*Wilcox[17], applying Saffman's model, has shown good results in the study of turbulent boundary layer separation and reattachment at moderate (2.96) Mach number.

the nonlinear equations, we must seek an alternative to the formulation by turbulence model equations. The alternative should be able to render a reasonably good description of the turbulent boundary layer development without a disproportional amount of computation time.

6.2 Mixing Length Theory

The mixing length theory herein is the one originated by Prandtl[18] and subsequently modified by Van Driest[19], Cebeci[20] and other researchers to include the effect of compressibility. The formulation, in comparison with turbulence models, is quite simple. The Reynolds stress tensor** τ_{ij} is expressed by the eddy viscosity ε .

$$\tau_{ij} = \varepsilon\left[\frac{\partial \bar{u}_i}{\partial x_1} + \frac{\partial \bar{u}_j}{\partial x_i} - \frac{2}{3}\frac{\partial \bar{u}_k}{\partial x_k}\delta_{ij}\right] - \frac{2}{3}\bar{\rho} e_s \delta_{ij} \qquad (12)$$

where $\bar{\rho} e = -\frac{1}{2}\tau_{ij}$

The eddy viscosity ε is then estimated by the mixing length theory which subdivides the shear layer into an inner and an outer region. Near the wall, we have

$$\varepsilon_i = K_1^2 y^2 D^2 \left|\frac{\partial \bar{u}}{\partial y}\right| \bar{\rho} \qquad (13)$$

where: $K_1 = 0.4$

y = normal direction from the solid wall

$\bar{u}$ = velocity component parallel to the wall

$D = 1 - \exp\left(\frac{y}{A}\right)$

$$A = \frac{26\,\nu}{\sqrt{\frac{\tau_w}{\bar{\rho}} + \frac{d\bar{p}}{dx}\frac{y}{\bar{\rho}}}}$$

**Total stress tensor σ_{ij} is given by $\sigma_{ij} = T_{ij} - \tau_{ij}$, with T_{ij} being the mean laminar stress tensor.

ν = kinematic viscosity coefficient

τ_w = shearing stress at the wall

$d\bar{p}/dx$ = pressure gradient in the direction parallel to the wall.

In the outer region, the so-called Clauser defect law is used.

$$\varepsilon_o = k_2 \bar{u}_{max} \delta_i^* \bar{\rho} \tag{14}$$

where $k_2 = 0.0168$

$\bar{u}_{max}$ = maximum value of $\bar{u}$ in the direction normal to the wall

δ_i^* = incompressible displacement thickness

$$= \int_o^{\delta} \left(1 - \frac{\bar{u}}{\bar{u}_{max}}\right) dy$$

The upper limit δ in the δ_i^* integral has to be defined to suit the compressor problem. It can be taken either as the mid-point of the channel defined by the blade-to-blade surface or the location where u_{max} occurs+. The eddy viscosity ε is then evaluated by

$$\varepsilon = \begin{cases} \varepsilon_i & \text{if } \varepsilon_i \le \varepsilon_o \\ \varepsilon_o & \text{if } \varepsilon_o < \varepsilon_i \end{cases} \tag{15}$$

A typical variation of ε is sketched in Figure 5. When the flow field extends to infinity in the y-direction, ε_o is often multiplied by the Klebanoff intermittency factor[21] $\underset{\sim}{\gamma}$,

$$\underset{\sim}{\gamma} = \left[1 + 5.5 \left(\frac{y}{\delta}\right)^6\right]^{-1} \tag{16}$$

which effectively makes ε_o decay away from the wall as it should by physical reasoning. The introduction of $\underset{\sim}{\gamma}$ is not necessary in the compressor problem.

The mixing length theory has enjoyed a large number of followers and many successes in applications. Cebeci and Smith[22] have applied it successfully to incompressible and compressible boundary layers, with and without separation[23], with mass and heat transfer[20], as well as low Reynolds number turbulent flows[24,25]. Figure 6 shows a comparison of results obtained by the mixing length theory[22] with measurements for a wasted

---

+The definition of δ does not affect the value of δ_i^* for a monatomic velocity profile.

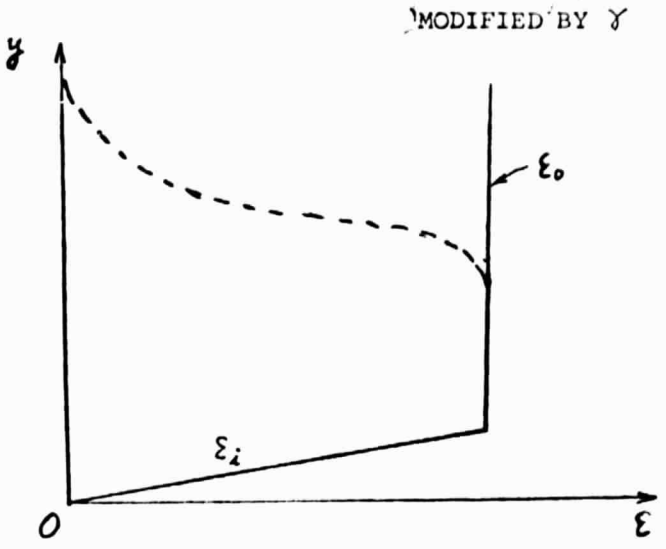

FIGURE 5. TYPICAL VARIATION OF EDDY VISCOSITY COEFFICIENT ε .

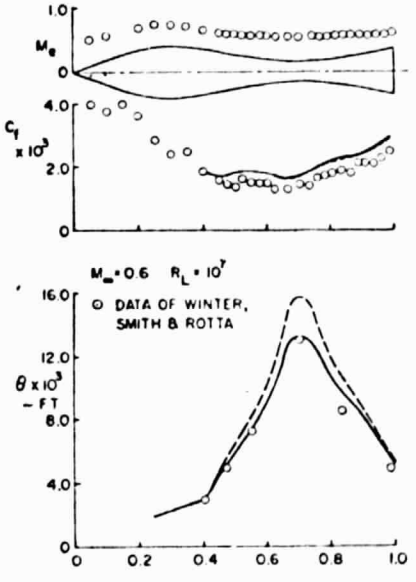

FIGURE 6 : COMPARISON OF RESULTS OBTAINED THROUGH THE MIXING LENGTH THEORY AND MEASUREMENTS OF WINTER, SMITH AND ROTTA FOR A WAISTED BODY OF REVOLUTION. THE EXTERNAL MACH NUMBER M_e IS GIVEN, THE SKIN FRICTION COEFFICIENT C_f AND THE MOMENTUM THICKNESS θ ARE COMPUTED ALONG THE AXIS. SOLID CURVE REPRESENTS CEBECI'S RESULT WITH CORRECTION FOR THE TRANSVERSE CURVATURE EFFECT, DOTTED CURVE SIGNIFIES RESULTS WITHOUT THE CORRECTION. THE EFFECT OF TRANSVERSE CURVATURE IS NEGLIGIBLE IN THE PREDICTION OF C_f. THE FREESTREAM MACH NUMBER M_∞ , AND THE REYNOLDS NUMBER R_L, BASED ON THE LENGTH OF THE BODY L, ARE ALSO GIVEN IN THE FIGURE.

body of revolution. The calculated skin friction coefficient C_f and momentum thickness θ seem to agree with experiment quite well. Most recently, Cebeci* successfully applied the mixing length theory to the study of internal flows in area-changing channels. However, the failure of the mixing length theory in the interaction problem of a strong shock with a hypersonic (free stream Mach number $\cong$ 8.5) turbulent boundary layer has also been reported by Baldwin and MacCormack[26]. It yields an incorrect pressure rise estimation on skin friction and heat transfer. However, the Saffman predictions were also found to be inaccurate in the same problem by the same authors. One may conclude that the mixing length theory, which is applicable to the attached boundary layer, is perhaps inadequate for the prediction of separated and reattached flows of the type examined by Baldwin and MacCormack. Again, the same conclusion is drawn for the transport model, Saffman's in this case. Fortunately, shock-boundary-layer interactions of this magnitude do not occur in the compressor problem. The track record of mixing length theory seems to certify its usefulness.

In almost any discussion concerning the mixing length theory (or equivalently, the concept of eddy viscosity), the criticism that eddy viscosity should not be a local property inevitably arises. It is indeed true that turbulence is a macroscopic phenomenon marked by eddies of finite size, and possesses a relaxation time similar to that of a visco-elastic solid. However, evidence has been gathered over the years to support the concept of a local eddy viscosity coefficient. It is believed that the mean-velocity gradient and the turbulent shearing stress generally go up and down together, in particular, they go to zero together. The concept of eddy viscosity leads to accurate predictions of velocity profiles over a vast range of parametric inputs.

In summary, the advantages of the mixing length theory are that[27]

1. It is simple, requiring no additional differential equation to solve. This is crucial in the compressor calculation, since the existing routine is complex enough because of the geometry of the compressor.

---

*Private communication.

2. It allows a realistic prediction to be made of the velocity and the shear-stresses, and the general behaviour of boundary layer flows.[28]

3. Much experience in the use of mixing length theory has been accummulated and is available in the literature.

Besides the comment on "local" property, the arguments against mixing length theory are as follows:

1. There is no successful evidence in predicting recirculating flows. However, the same comment applies to existing transport models.

2. It implies that the effective viscosity vanishes where the velocity gradient is zero, $\varepsilon_t \sim |\partial\bar{u}/\partial y|$. Transport models, on the other hand, do not provide a definitive relation between ε and $|\partial\bar{u}/\partial y|$, they provide a set of differential equations whose solution presumbaly defines that missing relation.

3. The mixing length theory takes no account of the convection or diffusion of turbulence.

The development of turbulence models is still in a preliminary stage; much modification to existing models is expected in the years ahead. In the absence of a clear-cut all purpose model, the one which has been experimented with the most, has shown the most success, and which is simplest to use should receive first attention in our compressor studies. Hence, we selected the mixing length theory as our tool in turbulence studies.

6.3 Separation

In general, there are two types of boundary layer separations: laminar and turbulent. Separations in compressors or diffusers may occur either way depending on the inlet conditions. In computational fluid dynamics, various criteria have been examined to identify the spearation point.

Separation on a plane or axisymmetric flow is defined by the point where the wall shear vanishes, namely, $\tau_w = 0$. In laminar flow, one can monitor the variation of the wall shear to locate separation. In addition, there are other simple criterion such as that based on the momentum integral method of Thwaites[29], and that of Stratford[30] through which laminar separation is defined. For example, laminar separation is predicted when $C_p^{1/2}\,(x\, dC_p/dx)$ reaches a value of 0.102, where C_p is the local pressure coefficient and x the streamwise distance from the leading edge. We shall simply monitor the wall shear and the pressure distribution to pinpoint the laminar separation point.

The prediction of turbulent separation is a much more difficult task. The current prediction methods can be divided into two groups. These methods are either of differential type (meaning that partial differential equations are solved) or of integral type (meaning that momentum integral or energy integral equations are solved)+. The simplest integral method involves the monitoring of the shape factor H, $H = \delta_i^*/\theta_i$ (δ_i^* is the incompressible displacement thickness, θ_i the incompressible momentum thickness). When H reaches a certain value (H = 2.8 is used by McNally[31], and the range between 1.8 and 2.4 is frequently cited), then separation of the turbulent flow is assumed to occur. Again, we shall just monitor the wall shear and extrapolate it to zero for the location of the separation point. In past computations, the peak of the wall pressure and the vanishing of the wall shear locate separation jointly.

In short, we shall introduce no additional criterion for the determination of laminar or turbulent separation other than its natural definition through the vanishing of wall shear. Since we solve the full Navier-Stokes equations numerically, we do not have to change governing equations after separation takes place.

+The 1968 AFOSR-IFP-Standard Conference on "Computation of Turbulent Boundary Layers" provides a critical evaluation of those methods[28].

7.0 RADIAL IMPELLER PROBLEM

To fully describe the debug problem selected, which was designated as "Problem 1.0", nine items are discussed. They are (1) input conditions, (2) geometry in cylindrical coordinates, (3) curvilinear coordinate system, (4) boundary conditions, (5) meshes, (6) inviscid solution, (7) medium viscosity, (8) constant speed, U_∞ , at which the blade-to-blade surfaces of calculation move from the hub-to-the-shroud, and finally, the results (9) of the numerical computation for problem 1.0.

7.1 Input Conditions

The radial impeller which served as the debug problem was selected by Dr. T. Katsansis of NASA Lewis Research Center. Input flow properties for the problem are as follows:

laboratory inlet total temperature = 536 ^{o}R

laboratory inlet total pressure = 861 psfa

rotational speed = 4031.70 rad/sec (38,600 rpm)

specific heat ratio = 1.667

gas constant = 38.73 ft/^{o}R

The above specific heat ratio and gas constant are for Argon.

7.2 Geometry

The radial impeller geometry is presented in the cylindrical coordinates r, θ, and x_3. These coordinates are defined in Figure 7 in terms of Cartesian coordinates X_1, X_2, and X_3. The sense of the angular rotation is also indicated. It is seen from Figure 7 that a left-handed coordinate system is being employed. Figure 8 presents traces of the hub and shroud lines in a half-plane through the axis of the impeller, i.e., a meridional plane. The hub and shroud radial coordinates are presented as functions of axial distance. Solid lines indicate the actual geometry of the machine, while dashed lines indicate formula approximations. The hub is approximated by an ellipse with its major axis on the radial axis, and the shroud is approximated by a super-ellipse having its major axis in the axial direction. The elliptic and super-elliptic formulas are also shown in Figure 8. The dashed hub and shroud lines extend above the discharge, so that the region of calculation contains the discharge. The hub elliptic formula approximation produces an inlet area about 9% greater than the

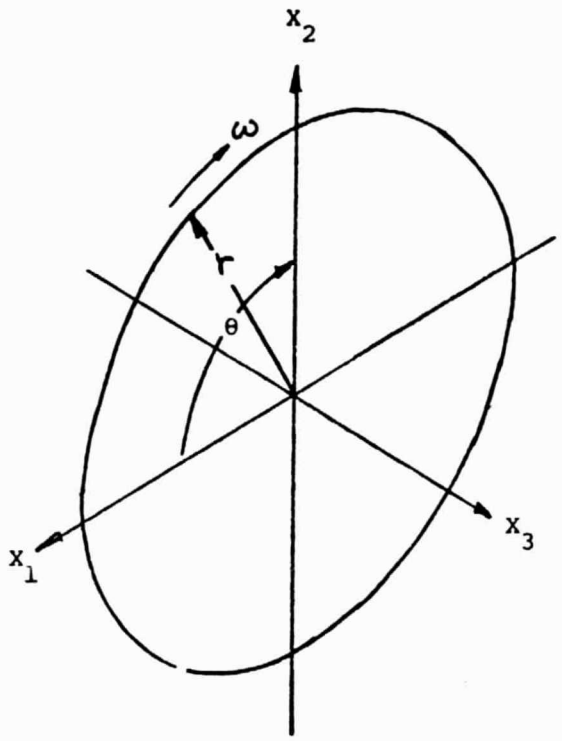

FIGURE 7: Cartesian and cylindrical coordinates for impeller debug problem.

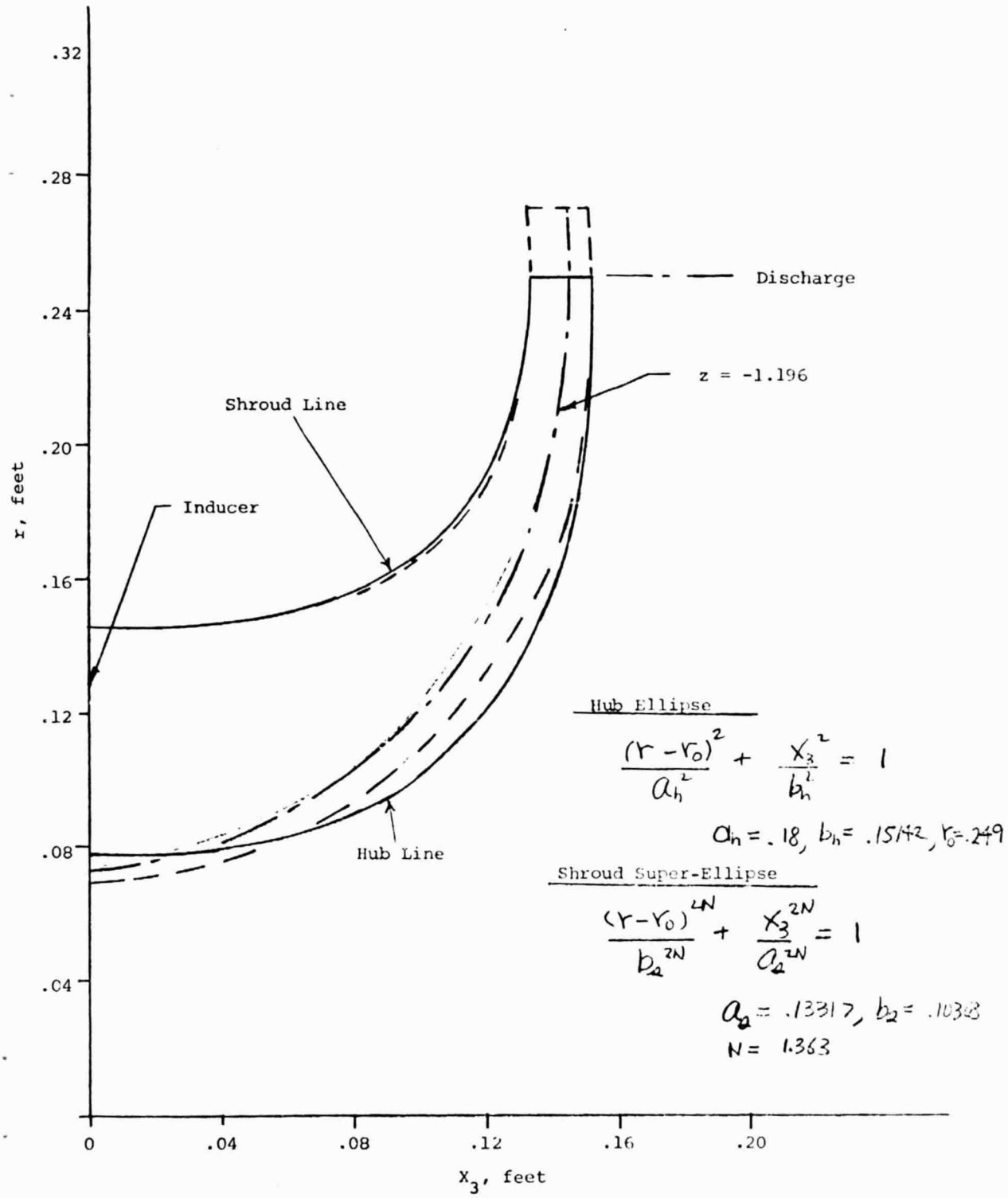

FIGURE 8: Radial and axial coordinates of the hub and shroud; solid lines indicate actual geometry; dashed lines indicate formula approximations.

actual inlet area. Although approximate, the hub formula simplified development of the IFFC computer code. The angular coordinates of the pressure and suction blade surfaces are shown in Figure 9 as functions of axial distance X_3. The solid lines indicate the traces of the blades on the hub, while the dashed lines indicate shroud blade traces.

7.3 Curvilinear Coordinate System

An axisymmetric orthogonal, curvilinear coordinate system was used to solve debug Problem 1.0. Consider the curvilinear coordinates x,y, and z. The surfaces x = constant were selected as half-planes through the axis of rotation of the machine, i.e., meridional planes. The surfaces y = constant and z = constant were obtained by rotating two orthogonal curves in the meridional plane about the axis of rotation of the machine. Since the hub was approximated as an ellipse, elliptic coordinates were used to establish the y and z surfaces. A family of confocal ellipses defined the z surfaces and a family of hyperbolas, orthogonal to the ellipses, defined the y-surfaces. Consider the interior ellipse shown in Figure 8. This ellipse is labelled with the constant value z =-1.196. The value of z is determined from the following formula:

$$\tanh z = -\frac{B}{A} \qquad (2)$$

where B and A are the lengths of the minor and major axis, respectively, of the interior ellipse. The negative sign permits z to increase as the blade-to-blade surface moves from the hub to the shroud. The orthogonal hyperbola to this ellipse is labelled with the constant value y. The value y is defined as the angle the asymptote of the hyperbola makes with the radial axis.

The transformation equations from cylindrical r, θ, x_3 space to curvilinear x,y, z space are shown below:

$$r = R_o = C \cosh Z \cos y$$

$$\theta = x \qquad (3)$$

$$X_3 = C \sinh Z \sin y$$

where R_o is the maxium radius of the impeller and C is the focus of the elliptic and hyperbolic coordinates. Formulas for the metrics of trans-

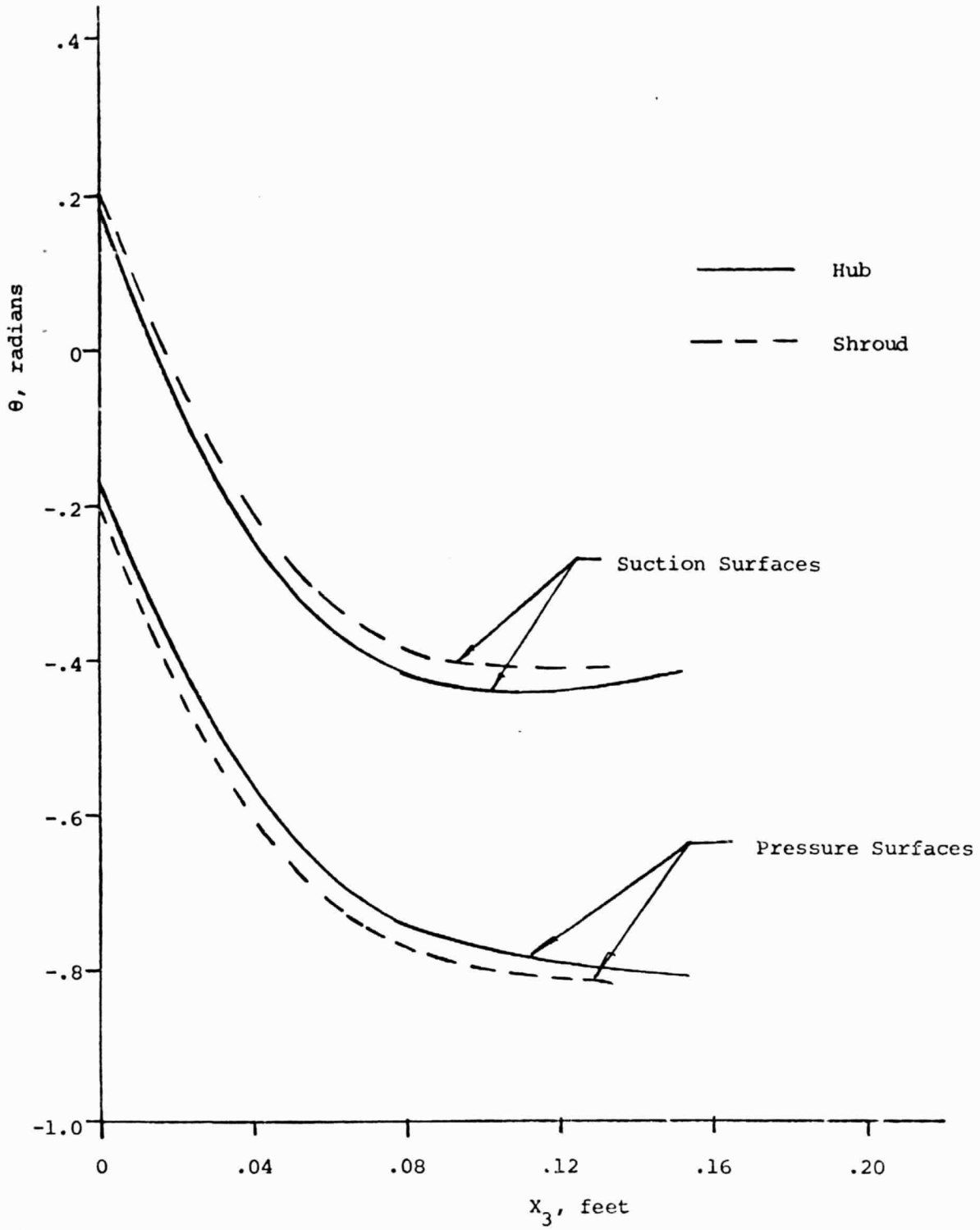

FIGURE 9: Angular and axial coordinates of the blading surfaces on the hub and shroud.

formation Equations (3),i.e., hx,hy,hz are derived in Table I as well as their derivatives. Application of Equation (3) to the geometry of Figures 8 and 9 results in the transformed geometry in the x,y,z space. The transformed geometry is shown in Figures 10 and 11. Figure 10 presents the hub and shroud lines in the y,z, plane. The hub is a horizontal straight line, since it is an ellipse. The shroud is still a curve, since it is a super-ellipse with a reversal of major and minor axis with respect to the hub ellipse. The interior ellipse of Figure 8, corresponding to z = -1.196 radians, is shown as a dashed horizontal straight line. Figure 11 shows the pressure and suction blade surfaces in the (x,y) plane. The solid lines indicate the blade traces on the hub, while the dashed lines indicate the blade traces on the shroud. In curvilinear space the calculation will take place in (x,y) planes which move from the hub to the shroud as the parameter z increases.

7.4 Boundary Conditions

Boundary conditions for the impeller problem in the (x,y) planes of calculation are indicated in Figure 12. At the upstream boundary of the region of calculation uniform inlet conditions are specified. Along the pressure and suction blade surfaces no slip flow is enforced. At the lateral boundaries upstream of the inducer and downstream of the discharge periodic boundary conditions are enforced. Finally, the back pressure is specified at the downstream boundary of the region of calculation.

To expedite development of the IFFC computer code, the upstream boundary was placed at the inducer in the solution of debug Problem 1.0. Inviscid conditions, discussed in Section 7.6, were prescribed along the upstream boundary. However, it is emphasized that boundary conditions of Figure 12 will be employed in the solution of all problems subsequent to the debug problem.

7.5 Meshes

From Figure 11 it is seen that the (x,y) blade-to-blade surface distorts as z increases from its value at the hub of z =-1.22524 radians to z= -1.14 radians near the shroud. Since the blade shape in the (x,y) plane distorts with z, the finite difference mesh must distort as well. Thus, a subroutine was developed to automatically distort the finite difference mesh in accordance with the blade geometry. Two meshes,

$h_x = R_o + C \cosh z \cos y$	$h_y = C(\sinh^2 z + \sin^2 y)^{1/2}$	$h_z = C(\sinh^2 z + \sin^2 y)^{1/2}$
$\frac{\partial h_x}{\partial x} = 0$	$\frac{\partial h_y}{\partial x} = 0$	$\frac{\partial h_z}{\partial x} = 0$
$\frac{\partial h_x}{\partial y} = -C \cosh z \sin y$	$\frac{\partial h_y}{\partial y} = \frac{C^2}{2h_2} \sin 2y$	$\frac{\partial h_z}{\partial y} = \frac{C^2}{2h_3} \sin 2y$
$\frac{\partial h_x}{\partial z} = C \sinh z \cos y$	$\frac{\partial h_y}{\partial z} = \frac{C^2}{2h_2} \sinh 2z$	$\frac{\partial h_z}{\partial z} = \frac{C^2}{2h_3} \sinh 2z$

TABLE I: VALUES AND DERIVATIVES OF THE TRANSFORMATION METRICS FOR THE AXISYMETRIC, ELLIPTIC COORDINATE SYSTEM OF PROBLEM 1.0.

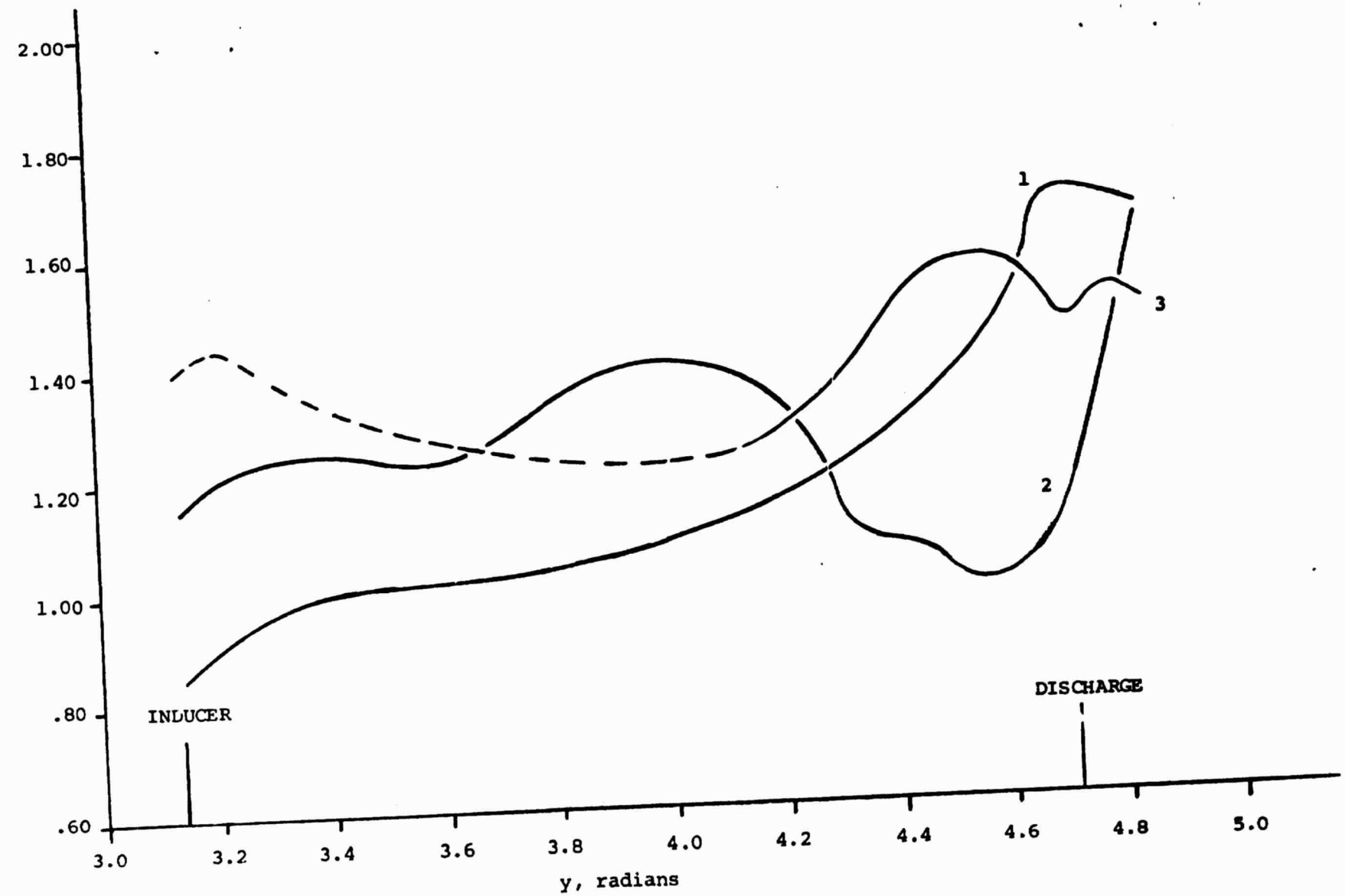

FIGURE16 : PRESSURE DISTRIBUTIONS ON THE PRESSURE BLADE SURFACE ALONG VARIOUS SURFACES OF REVOLUTION; CURVE 1 DENOTES THE INITIAL PRESSURE DISTRIBUTION AT z = -1.22524; CURVE 2 DENOTES THE PRESSURE DISTRIBUTION SHORTLY AFTER THE START OF THE CALCULATION AT z = -1.21892; CURVE 3 DENOTES THE PARTIALLY CONVERGED DISTRIBUTION AT z = -1.1960; THE UNCONVERGED PORTION OF CURVE 3 IS DASHED.

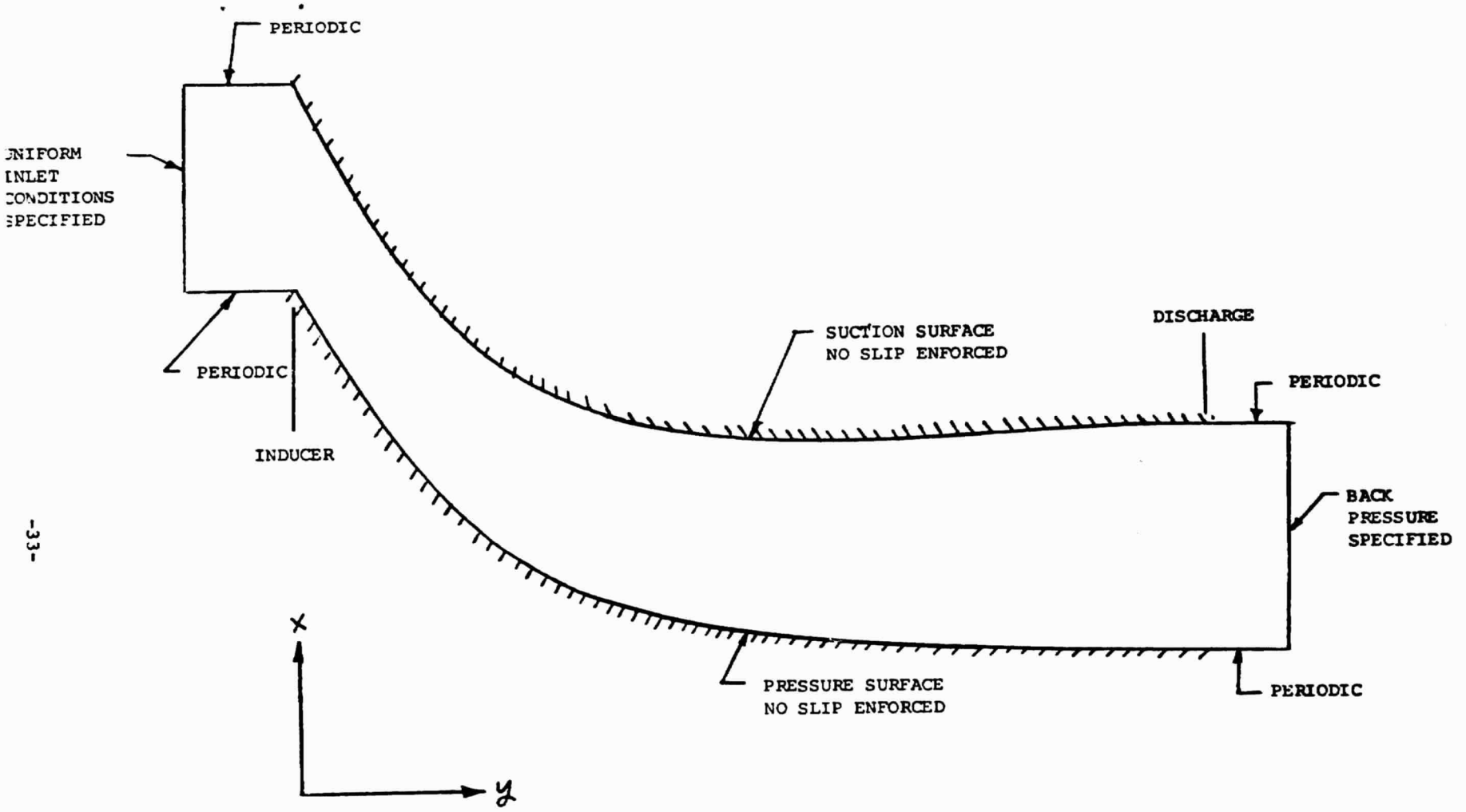

FIGURE 12: BOUNDARY CONDITIONS FOR IMPELLER BLADE-TO-BLADE SURFACE CALCULATION

corresponding to z = - 1.22524 radians and z =-1.14 radians are shown in Figures 13 and 14, respectively. Each mesh is formed by the intersection of 20 streamline-like-lines and 39 potential-like-lines, i.e., 780 points. The streamline-like lines are spaced closer in the vicinity of the blades than in the center of the blade passage.

7.6 Inviscid Solution

In order to solve the equations of motion shown in Appendix A, the inviscid solution is required. The inviscid flow field serves two purposes. First, the inviscid field at the hub provides initial conditions for the viscous calculation: for debug Problem 1.0 the hub boundary layer was neglected. Second, as discussed in Section 4.0 the inviscid flow field is the zeroth iterate in the interation procedure.

The inviscid flow field for debug Problem 1.0 was solved for by Vanco (Ref. 36) using the meridional velocity gradient method of Katsanis (Ref. 10). The velocity vector and pressure fields were calculated on the mean mean hub-to-shroud stream surface of the impeller channel. These properties were specified along five streamlines, as well as the suction and pressure blade velocities associated with each r, X_3 point along the streamlines.

At a given mesh point in the flow field the velocity vector, specific internal energy, pressure, and density were determined in the following manner. First the velocity vector was found by linear interpolation in the inviscid field of Vanco. The rothalpy, $H = E + W^2/2 - r^2\omega^2/2$ which is invarient along inviscid streamlines, was then used to compute the specific internal energy in terms of the velocity and radius at the given point, i.e.,

$$E = E_o \left[1 - \frac{W^2 \quad \omega^2 r^2}{2 \gamma E_o} \right] \qquad (4)$$

where E_0 is the inlet stagnation specific internal energy in the laboratory frame, W is the magnitude of the relative velocity vector, r is the local radius, ω is the angular velocity and γ is the specific heat ratio. Pressure was calculated from the given mean stream surface pressure by assuming insetropic flow along each blade-to-blade circular arc associated with r and X_3. The density was then determined from the equation of state.

$$\rho = \frac{p}{(\gamma-1)\, E}$$

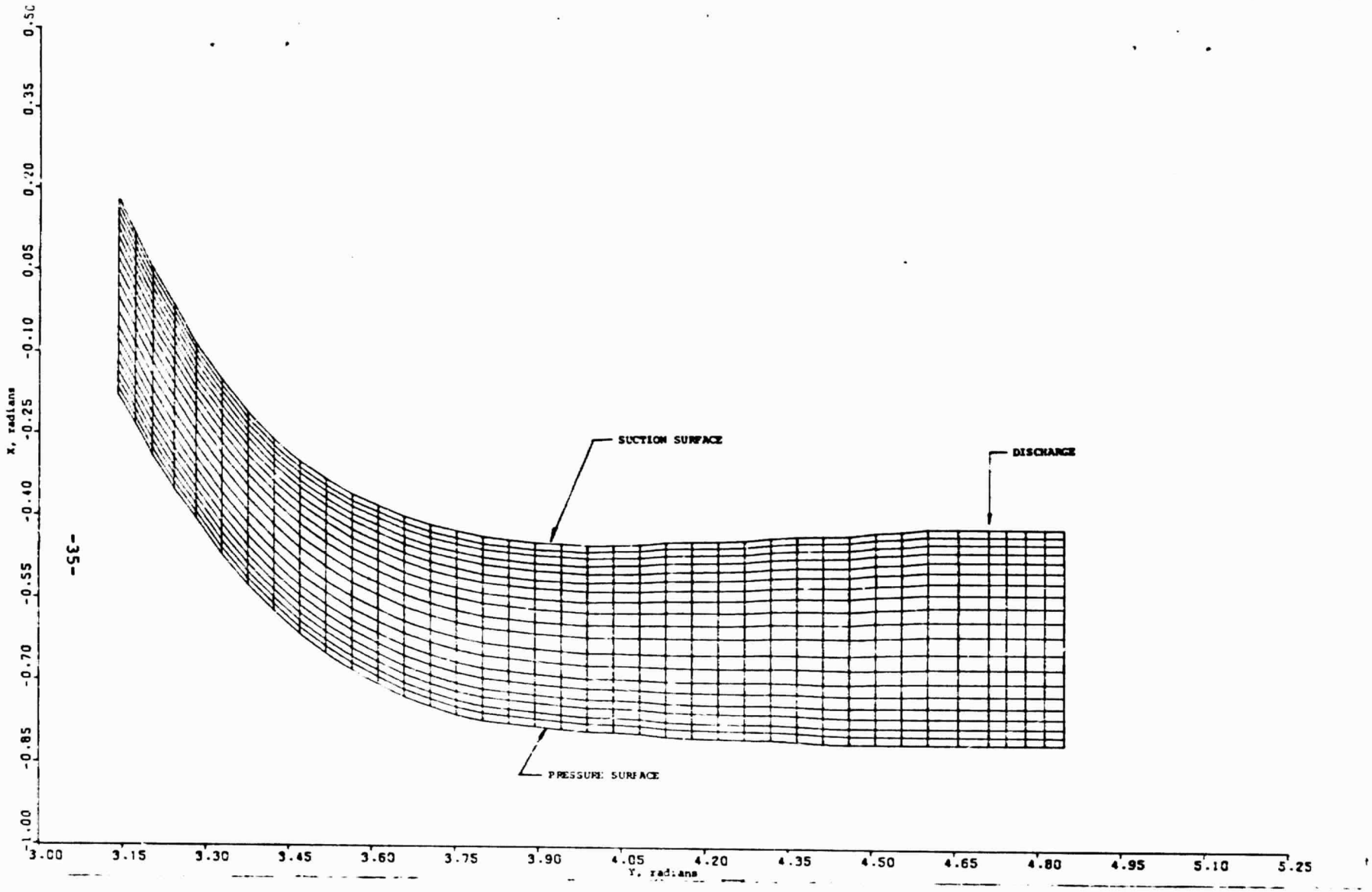

FIGURE 13 : FINITE DIFFERENCE MESH FOR THE IMPELLER HUB BLADE-TO-BLADE SURFACE OF CALCULATION; z = -1.22524 RADIANS; MESH IS COMPOSED OF 20 x 39 POINTS.

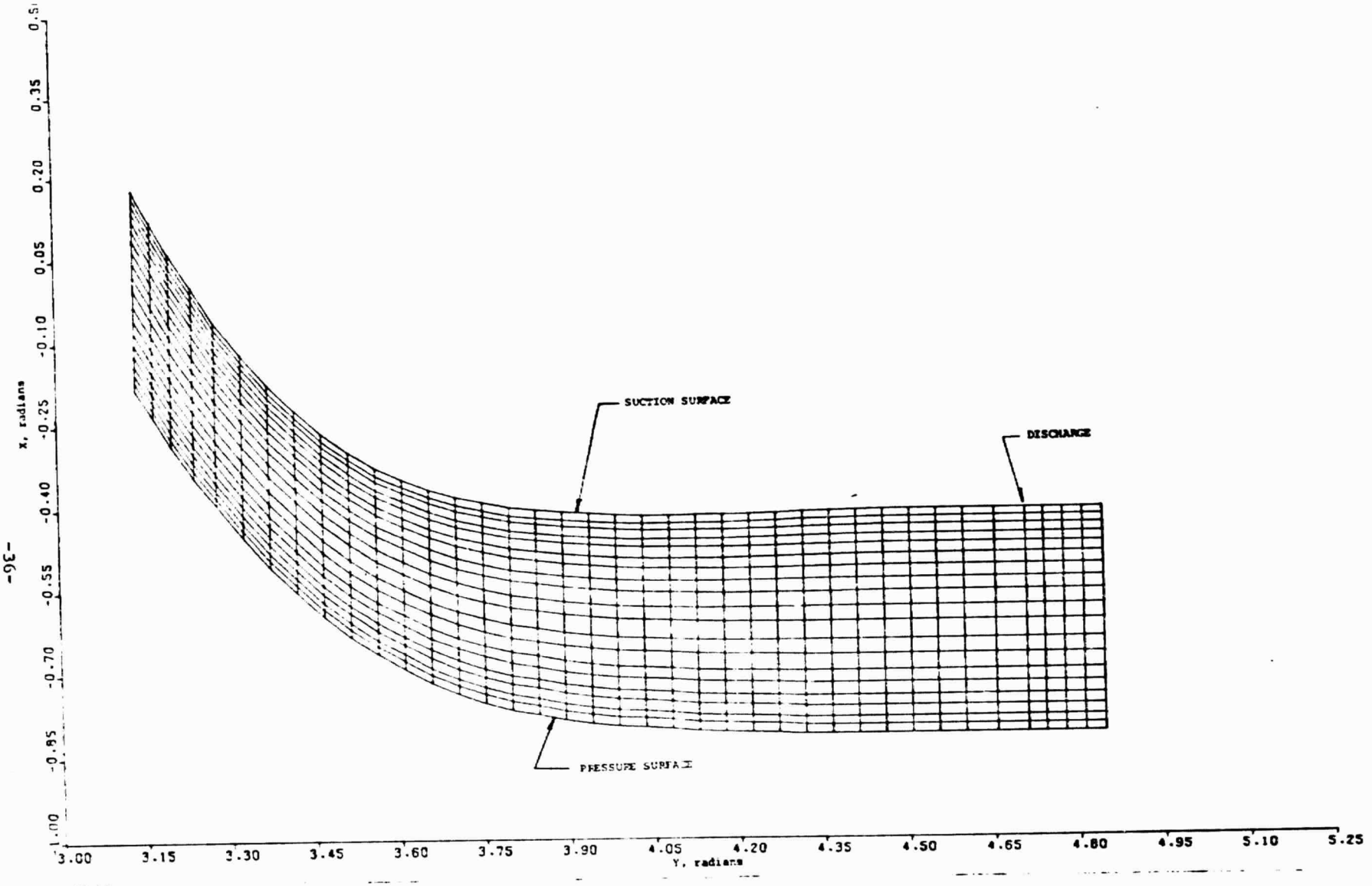

FIGURE 14 FINITE DIFFERENCE MESH FOR THE IMPELLER BLADE-TO-BLADE SURFACE OF CALCULATION AT z = -1.14 RADIANS; MESH COMPOSED OF 20 x 39 POINTS.

The flow field above the discharge was computed from relations governing flow in a vaneless diffuser. The mass, angular momentum in a laboratory frame, and rothalpy were conserved. The viscous mixing above the discharge was partially accounted for through an entropy gain; the density at the downstream boundary was reduced to 95% of it's isentropic value.

The inviscid relative velocity field at the hub, z = - 1.22524 radians, is shown in Fig.15. These vectors have magnitudes proportional to the particle velocities in the (x,y) plane; their tails emanate from the mesh points of Figure 13. The * symbols indicate the pressure and suction blade surfaces. A value of $\pi/2$ was added to the angular x values of Figure 13 to produce positive ordinate values. The locations of the pressure and suction blade surfaces are reversed between Figures 13 and 15 because the abscissa of Figure 15 is located on the top of the page, while the abscissa of Figure 13 is located on the bottom of the page. It is seen from Figure 15 that the velocity profile is linear between the pressure and suction blades. Furthermore, Mach number calculations in the vicinity of the inducer indicate transonic flow. For example, at the upstream boundary of the region of calculation, i.e., the inducer, the suction blade Mach number is .95.

7.7 Medium Viscosity

The meshes of Figures 13 and 14 have zone widths in the neighborhood of the suction and pressure blades which are too coarse to define a thin boundary layer. For example consider the inviscid field at the hub shown in Figure 15. At the inducer the suction blade Reynolds number per foot for Argon is 2.09×10^6. The hub ellipse is .26 feet in arc length, so based on this dimension the exit Reynolds number for Argon is about 545,000. This Reynolds number would probably produce a turbulent boundary layer thinner than the width of the first layer of zones adjacent to the suction blade surface. Therefore, to resolve the boundary layer with the meshes of Figures 13 and 14, a Reynolds number reduction is required.

Flat plate analysis indicated that for an inducer suction blade Reynolds number of 20,000 per foot, the laminar boundary layer at discharge

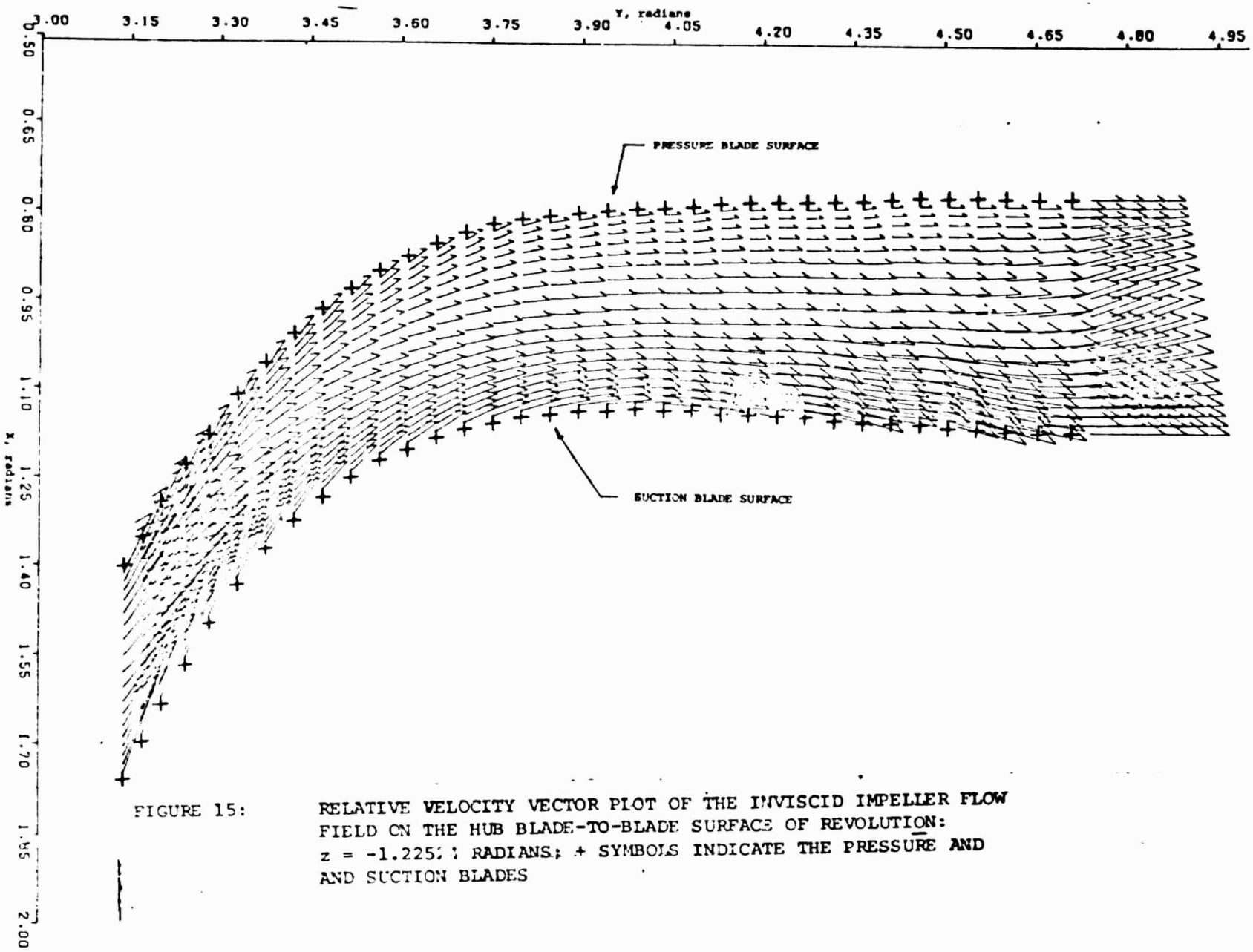

FIGURE 15: RELATIVE VELOCITY VECTOR PLOT OF THE INVISCID IMPELLER FLOW FIELD ON THE HUB BLADE-TO-BLADE SURFACE OF REVOLUTION: z = -1.225 ; RADIANS; + SYMBOLS INDICATE THE PRESSURE AND AND SUCTION BLADES

is contained in about five zones of the mesh. Based on the arc length of .26 feet of the hub ellipse, the discharge Reynolds number is then 5000.

Therefore, in order to get meaningful results with the meshes of Figures 13 and 14 it was necessary to invent a fictious medium having the compressibility properties of Argon and the viscous properties appropriate to a Reynolds number of 5000. Thus, the flow field of debug problem 1.0 is quite far from actual impeller flows and can only be considered in a qualitative sense.

7.8 Specification of U_∞ ; Speed at which Blade to Blade Surfaces of Calculation Move from Hub-to-Shroud

To run debug Problem 1.0, the speed U_∞ at which the (x,y) blade-to-blade planes move from the hub to the shroud must be specified. The final steady solution will be independent of U_∞ ; however, intermediate solutions will depend on the magnitude of U_∞ . The speed U_∞ must be small enough to permit viscous diffusion effects at the blade surfaces to build up boundary layers which subsequently separate. The time it takes a particle at the inducer to travel to the discharge is the characteristic time, t , for boundary layer build-up (Reference 3).

The speed U_∞ was determined in terms of the characteristic time t in the following manner. Consider flow along the suction blade at the hub. The average velocity is about 583 fps and the hub arc length is .26 feet. Therefore, the characteristic time is .444 ms. Since the time it takes the boundary layer to develop is t, let us assume that another characteristic time is necessary to permit the boundary layer to separate. Hence, approximately $2t$ characteristic times are required for the (x,y) blade-to-blade plane to go from the hub to the shroud. If 1.9 characteristic time passes in the time period that the (x,y) blade-to-blade surface moves from the hub to the shroud, then the appropriate speed is U_∞ = 21.8 fps.

7.9 Radial Impeller Numerical Results

Problem 1.0 was run 750 cycles*, or long enough in time for the z parameter to increase from z = -1.22524 radians at the hub to z = -1.194 radians; the (x,y) blade-to-blade plane moved approximately 37% of the total increment in z between the hub and the shroud at discharge. This partial solution of Problem 1.0 required 23 minutes on the CDC 7600 computer.

Shortly after the calculation commenced, it was found that there was a mass imbalance in the initial conditions. The elliptic formula approximation to the hub geometry (see Section 7.2) increased the inducer flow area by 9% from the actual flow area. Vanco's inviscid solution was not corrected for this geometry change. Therefore, a mass imbalance was produced in the initial conditions of Figure 15; more mass flux entered the system than exited from the system.

The mass imbalance is indicated in pressure distributions along the blade surfaces. In Figure 16 pressure distributions on the pressure blade surface are shown for three values of the z parameter. The abscissa of Figure 16 represents the angular coordinate y, while the ordinate is the ratio of the local to inlet stagnation pressure, i.e., p/p_o . Curve 1 represents the initial pressure blade distribution at z = -1.22524 radians; the initial exit pressure ratio is 1.635. Curve 2 represents the distribution 100 cycles after the start of calculation, i.e., z = -1.2189 radians. There is a pressure peak in the center of the channel followed by a deep rarefaction in the radial portion of the impeller. The deep rarefaction and fixed high exit pressure induced back flow at the downstream boundary, a condition of impeller surge. To prevent surge the back pressure was lowered to a ratio of 1.47. At the lower back pressure level outflow was maintained at the downstream boundary and the problem was continued.

*A cycle of calculation consists of updating the dependent variables of motion through one timestep over all the mesh points.

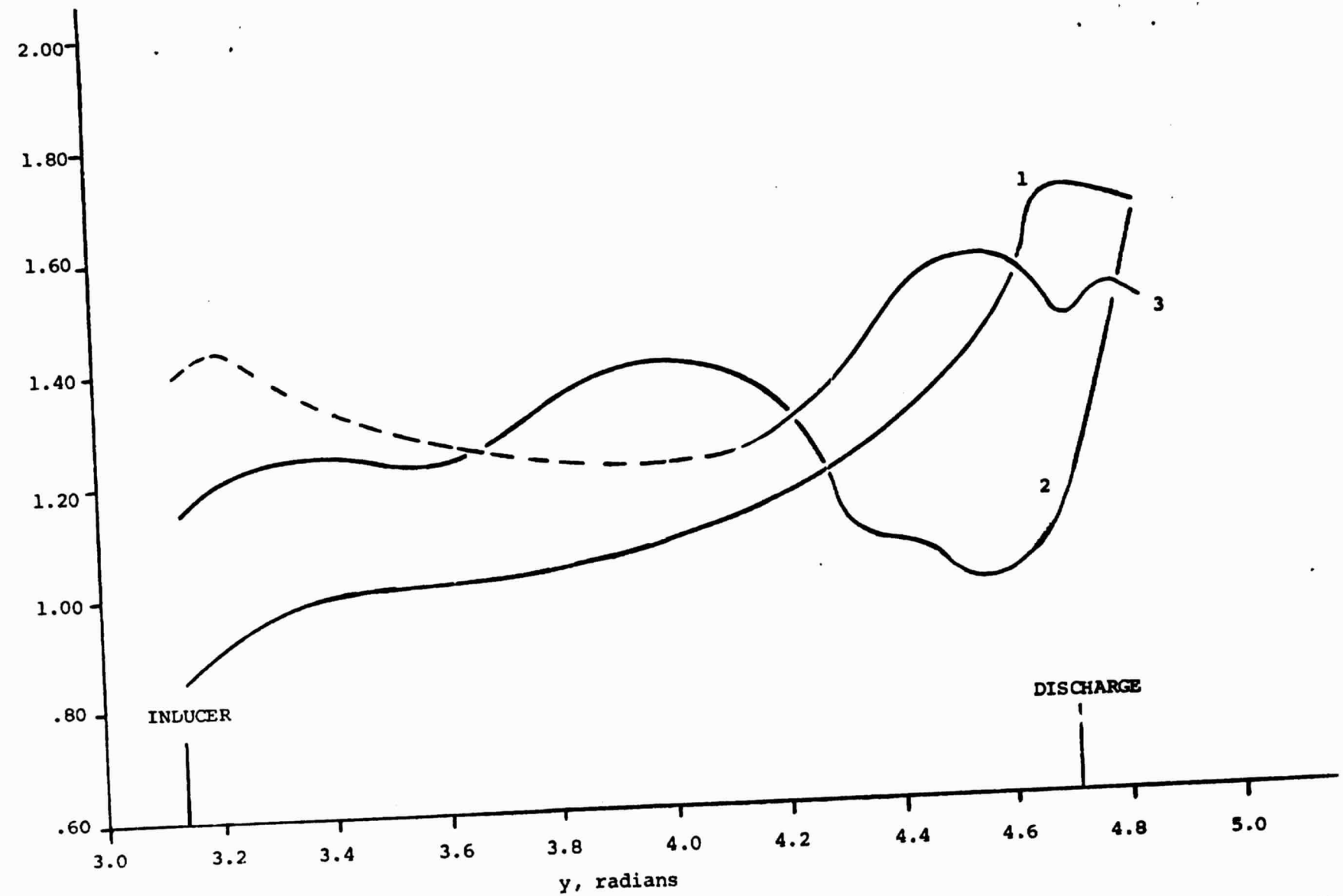

FIGURE16 : PRESSURE DISTRIBUTIONS ON THE PRESSURE BLADE SURFACE ALONG VARIOUS SURFACES OF REVOLUTION; CURVE 1 DENOTES THE INITIAL PRESSURE DISTRIBUTION AT z = -1.22524; CURVE 2 DENOTES THE PRESSURE DISTRIBUTION SHORTLY AFTER THE START OF THE CALCULATION AT z = -1.21892; CURVE 3 DENOTES THE PARTIALLY CONVERGED DISTRIBUTION AT z = -1.1960; THE UNCONVERGED PORTION OF CURVE 3 IS DASHED.

The pressure wave and trailing rarefaction calculated at cycle 100 started moving towards the inducer and the solution in the radial portion of the impeller converged. Convergence was demonstrated by inspection of the flow field over a small change in the z coordinate. For a given small change in z the flow field in the radial portion of the impeller changed slightly, while flow near the inducer changed markedly. Curve 3 of Figure 16, which corresponds to cycle 550 or z =-1.196 radians, is converged in the radial portion of the impeller. The solid line represents the converged region of the flow and the dashed line represents the unconverged region.

The upstream moving pressure wave finally impacts the upstream boundary, reflects from it, and amplifies. The inviscid conditions prescribed at the upstream boundary cause reflection and amplification of the pressure wave. This same phenomenon was observed in previous cylinder calculations started from impulsive initial conditions (Ref.2). Problem 1.0 could not be continued beyond this point without moving the upstream boundary upstream of the inducer.

The three-dimensional flow field in the radial portion of the impeller has converged and is very interesting. Results are presented for the radial portion of the impeller in the remainder of this section.

The sequence of events as the flow develops in the impeller channel is illustrated in the velocity vector plots of Figures 17 and 18. Figure 17 shows a velocity vector plot at cycle 100 (z = -1.2189 radians) and Figure 18 shows the velocity field at cycle 450 (z = -1.991 radians). In Figure 17 boundary layers are seen on both the pressure and suction blade surfaces. A flow instability is beginning to occur at the downstream end of the suction blade surface. At cycle 450 (z = -1.991 radians) the flow has converged in the radial portion of the impeller. A thicker pressure blade surface boundary layer than present at cycle 100 is clearly indicated in Figure 18. Furthermore, the suction blade boundary layer has separated and a large vortex is in evidence on the suction blade surface near discharge. The vortex takes up almost half the channel width between blades. The reduced channel flow area causes an acceleration of the flow about the vortex; large vectors are in evidence just above the vortex. This large vortex is consistent with the size of vortices previously

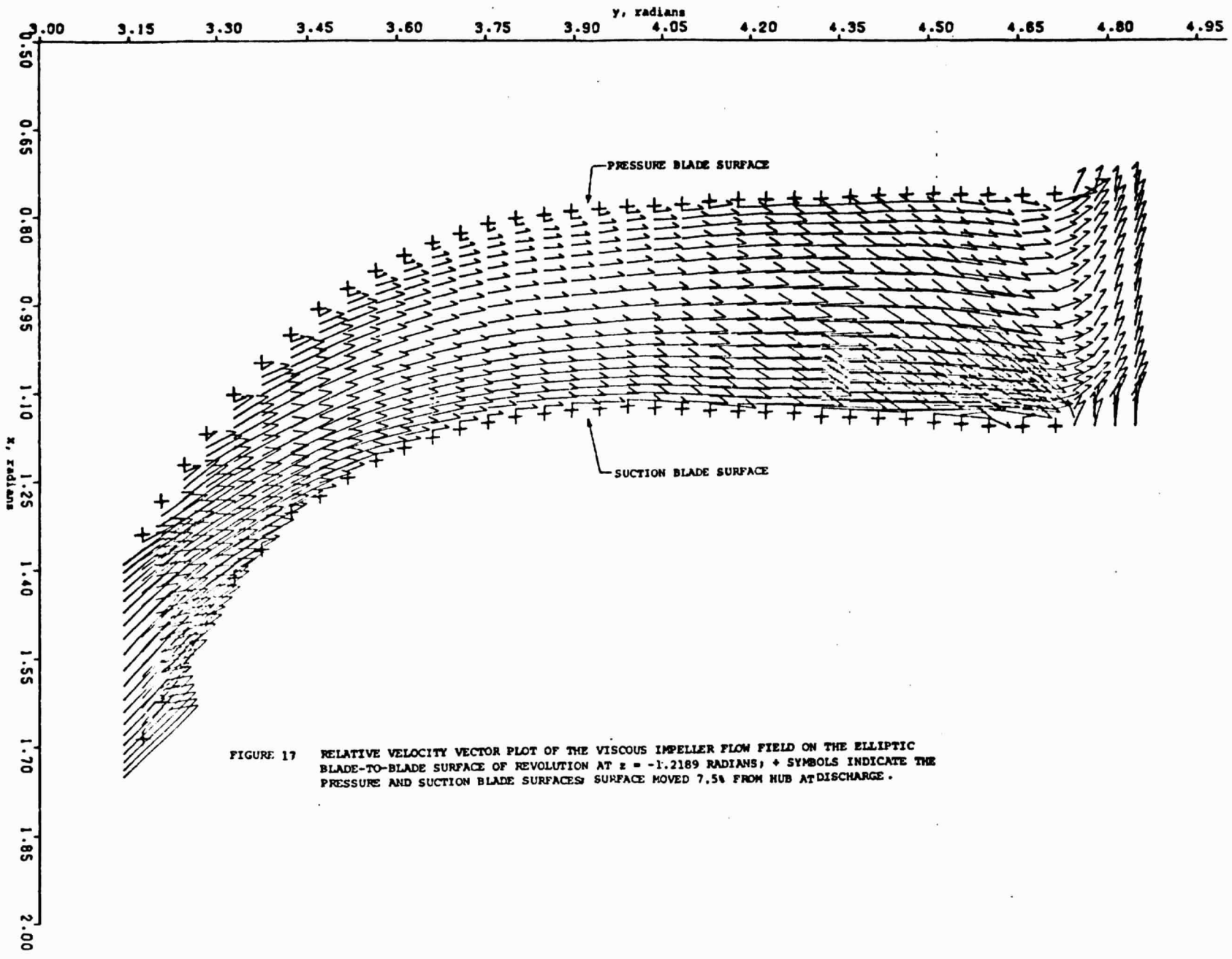

FIGURE 17 RELATIVE VELOCITY VECTOR PLOT OF THE VISCOUS IMPELLER FLOW FIELD ON THE ELLIPTIC BLADE-TO-BLADE SURFACE OF REVOLUTION AT z = -1.2189 RADIANS; + SYMBOLS INDICATE THE PRESSURE AND SUCTION BLADE SURFACES; SURFACE MOVED 7.5% FROM HUB AT DISCHARGE.

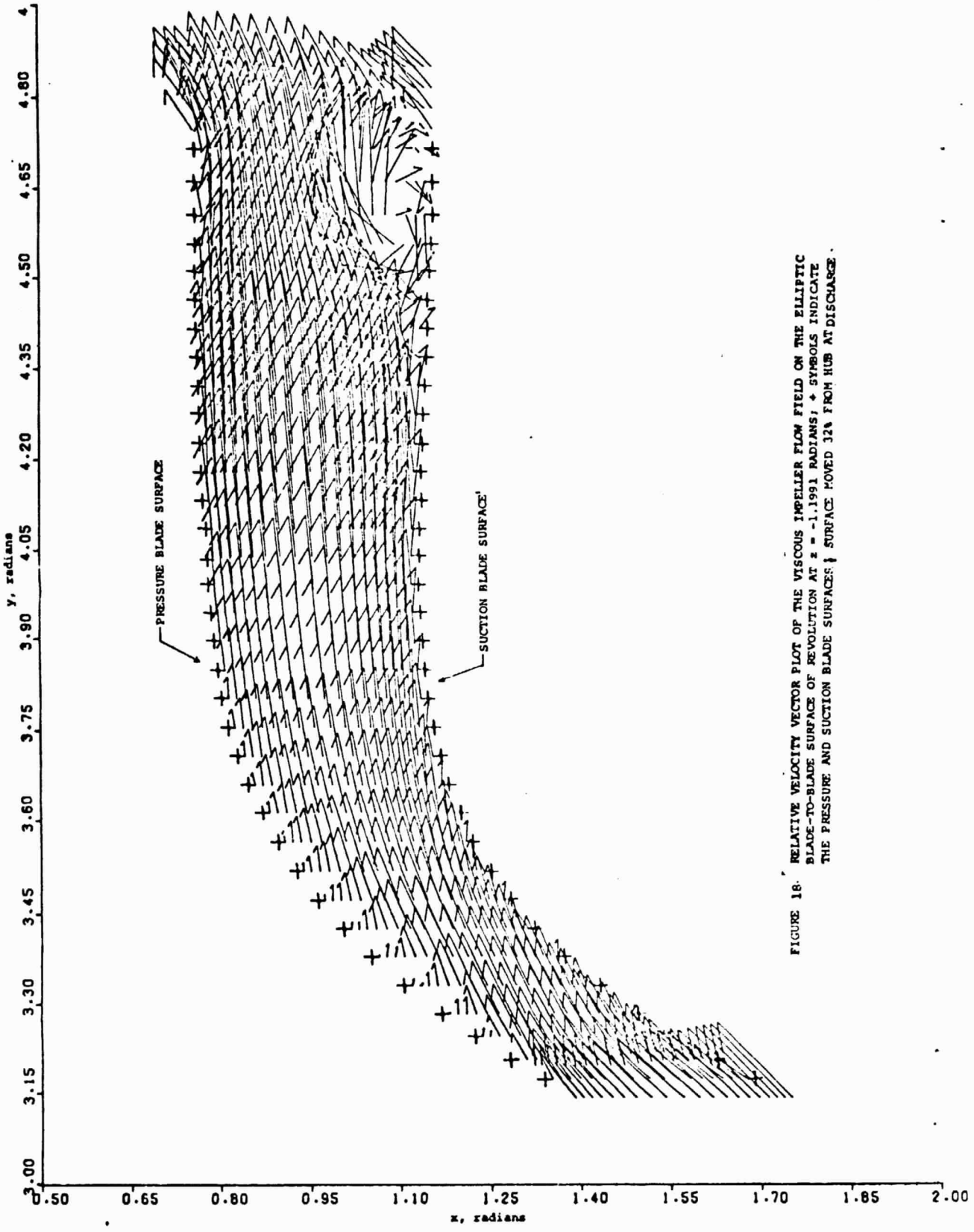

FIGURE 18. RELATIVE VELOCITY VECTOR PLOT OF THE VISCOUS IMPELLER FLOW FIELD ON THE ELLIPTIC BLADE-TO-BLADE SURFACE OF REVOLUTION AT z = -1.1991 RADIANS; + SYMBOLS INDICATE THE PRESSURE AND SUCTION BLADE SURFACES; SURFACE MOVED 32% FROM HUB AT DISCHARGE.

determined about cylinders at low Reynolds number (References 1 and 2).

A comparison of viscous and inviscid velocity fields is presented in Figures 19 and 20 on an (x,y) plane of calculation which has moved about 33% of the total increment in z at the discharge. In the viscous flow field of Figure 19, which corresponds to cycle 550 (z = -1.196 radians), the separated region has grown larger and feeds into the boundary layer on the suction surface. The subsonic nature of the flow causes the suction blade velocity vectors upstream of the separation to adjust to the vortex. Figure 20 shows the corresponding inviscid flow field at z = -1.1960 radians. Due to the absence of viscosity, the inviscid suction blade flow does not separate.

The velocity field in the radial portion of the impeller at the final cycle calculated, i.e., cycle 750, is shown in Figure 21. A well formed vortex is seen in Figure 21 which extends aft of the discharge. A reversed flow profile is clearly seen in Figure 21. The results of Figure 21 indicate that the velocity field is highly non-uniform above the discharge plane.

A comparison of the viscous and inviscid pressure distributions in the radial portion of the impeller is presented in Figure 22. These data correspond to z = - 1.196 radians or on an (x,y) blade-to-blade plane of calculation which has moved 33% of the total z increment between the hub and shroud at discharge. The pressure surface comparison (Figure 22b) indicates that the viscous pressures are no more than 8% high than the inviscid pressures upstream of the station in the channel where the back-pressure influences the discharge flow. The lower back-pressure in the viscous suction blade surface pressure of Figure 22a drops off at the separation point to nearly coincide with the inviscid solution. The rapid drop in pressure in the viscous case is consistent with the increase in the flow velocity just above the vortex (see figure 21).

Although the flow field in the inducer region has not yet converged, it is clear that the IFFC computer code has duplicated, at least qualitatively, the flow phenomena that have been observed to occur in the radial portion of an impeller (Ref. 37). We therefore conclude that the IFFC computer code works for laminar flows.

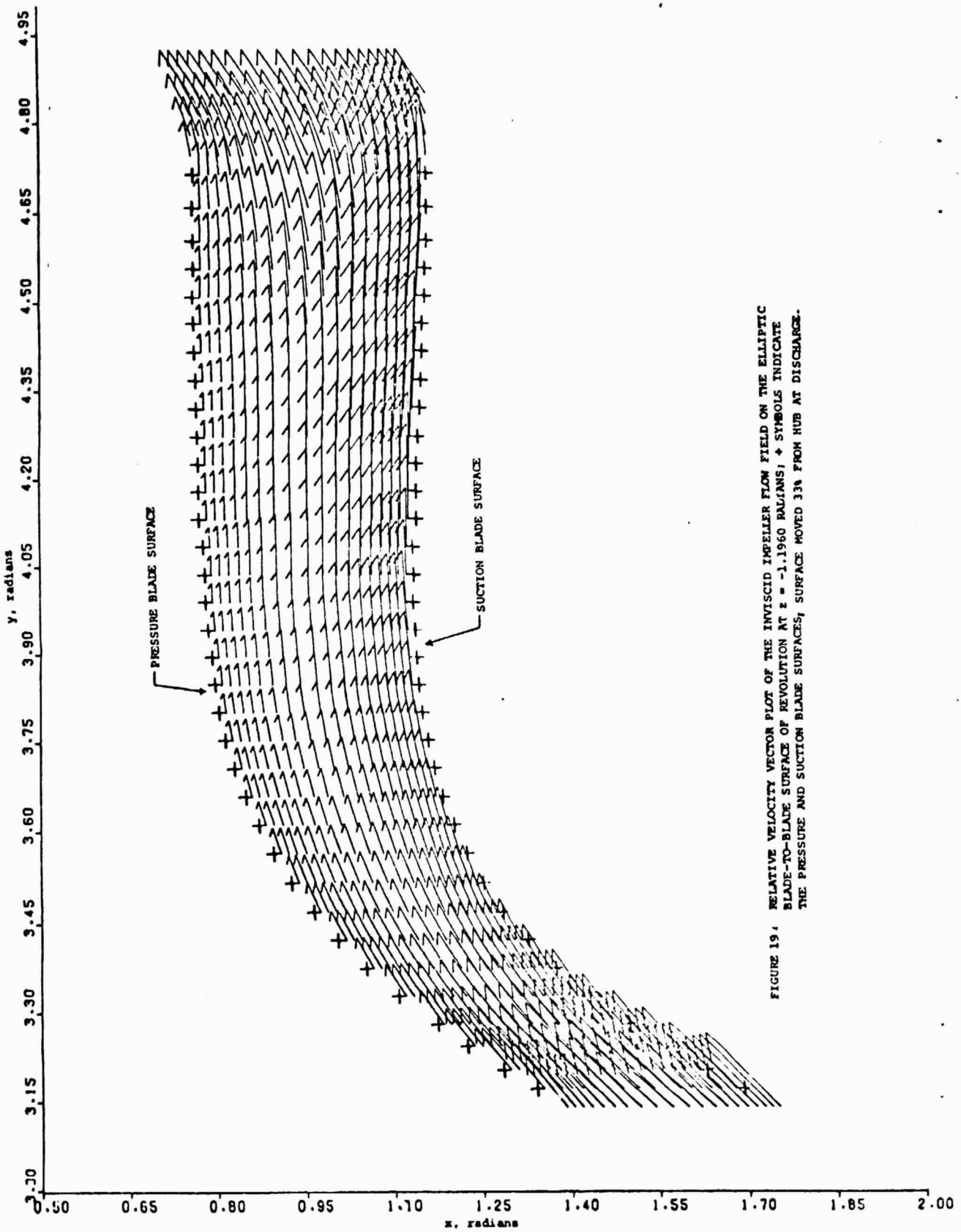

FIGURE 19: RELATIVE VELOCITY VECTOR PLOT OF THE INVISCID IMPELLER FLOW FIELD ON THE ELLIPTIC BLADE-TO-BLADE SURFACE OF REVOLUTION AT z = -1.1960 RADIANS; + SYMBOLS INDICATE THE PRESSURE AND SUCTION BLADE SURFACES, SURFACE MOVED 33% FROM HUB AT DISCHARGE.

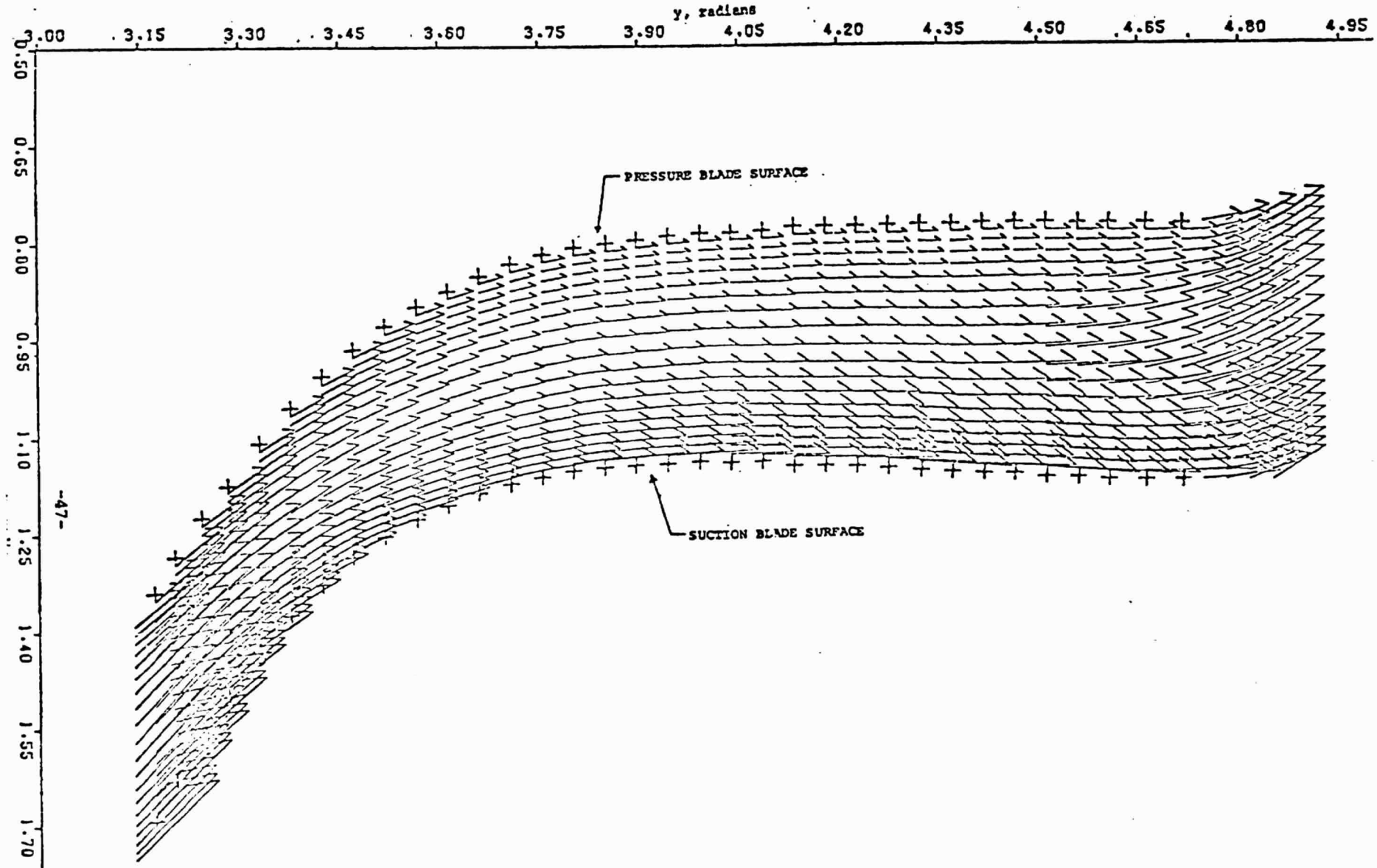

FIGURE 20: RELATIVE VELOCITY VECTOR PLOT OF THE INVISCID IMPELLER FLOW FIELD ON THE ELLIPTIC BLADE-TO-BLADE SURFACE OF REVOLUTION AT z = -1.1960 RADIANS; + SYMBOLS INDICATE THE PRESSURE AND SUCTION BLADE SURFACES; BLADE-TO-BLADE SURFACE HAS MOVED 33% OF THE DISTANCE BETWEEN THE HUB AND SHROUD AT DISCHARGE

-47-

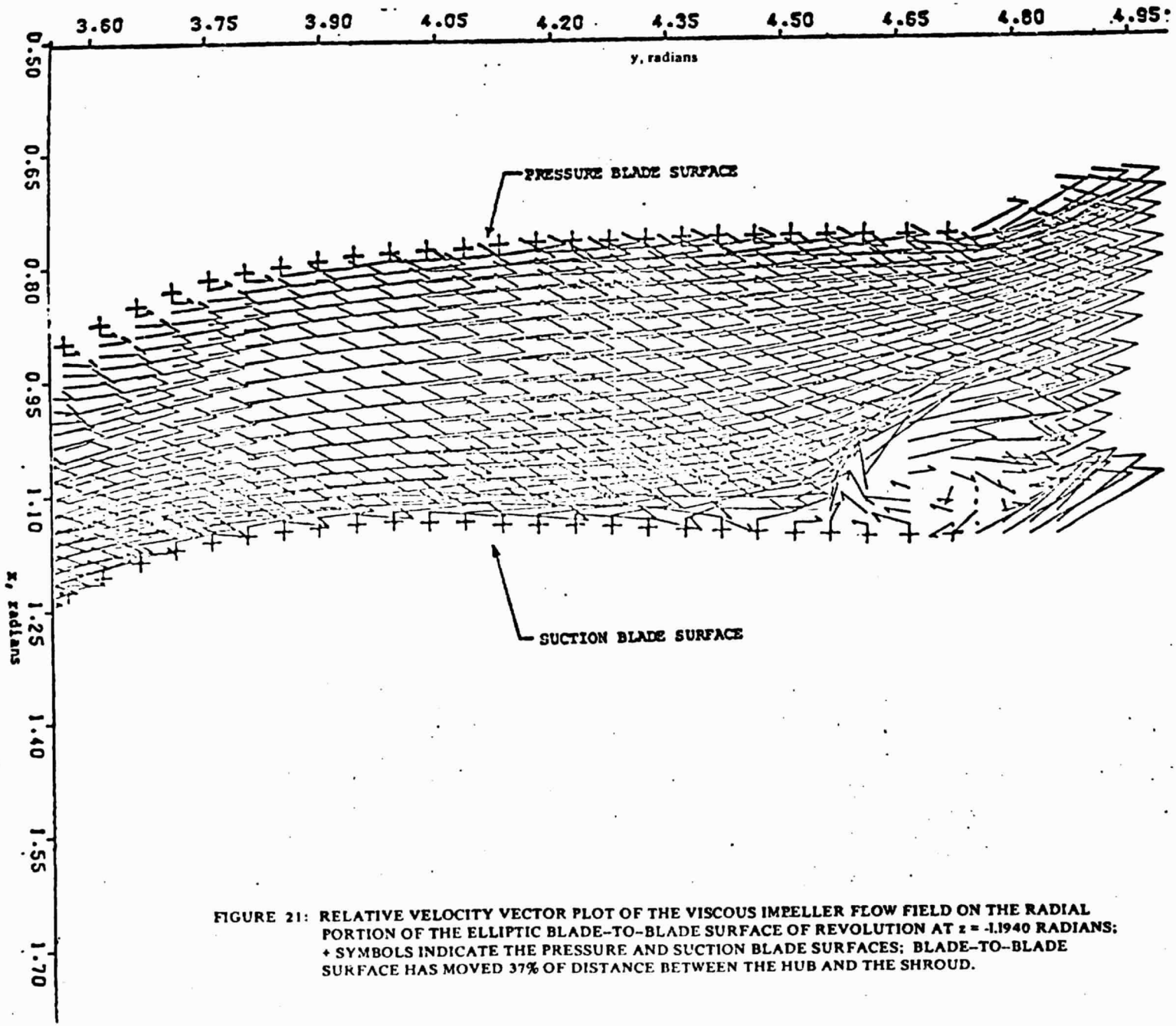

FIGURE 21: RELATIVE VELOCITY VECTOR PLOT OF THE VISCOUS IMPELLER FLOW FIELD ON THE RADIAL PORTION OF THE ELLIPTIC BLADE-TO-BLADE SURFACE OF REVOLUTION AT z = -1.1940 RADIANS; + SYMBOLS INDICATE THE PRESSURE AND SUCTION BLADE SURFACES; BLADE-TO-BLADE SURFACE HAS MOVED 37% OF DISTANCE BETWEEN THE HUB AND THE SHROUD.

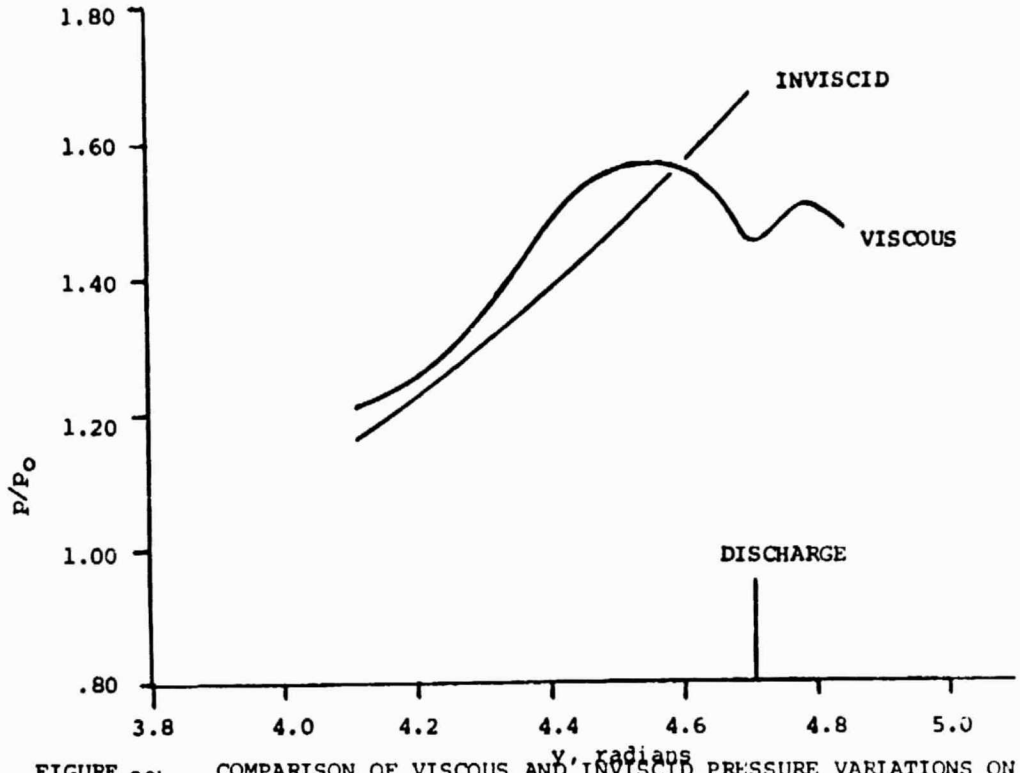

FIGURE 22b COMPARISON OF VISCOUS AND INVISCID PRESSURE VARIATIONS ON THE RADIAL PORTION OF THE IMPELLER; z = -1.1960; PRESSURE SURFACE.

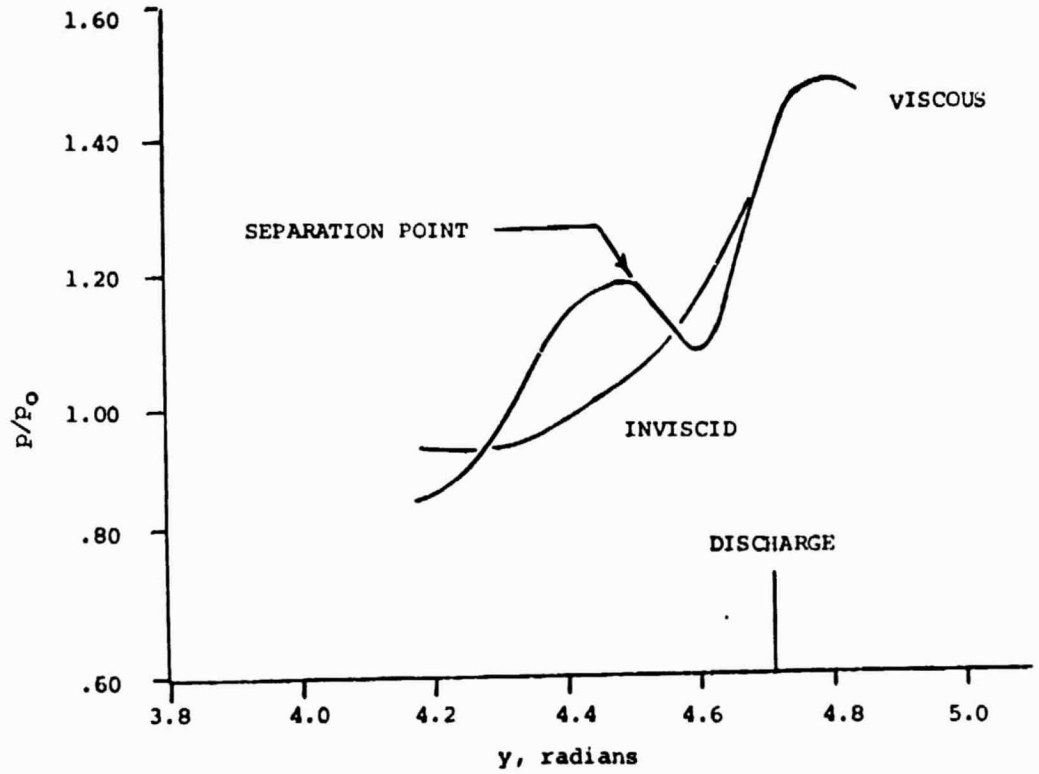

FIGURE 22a COMPARISON OF VISCOUS AND INVISCID PRESSURE VARIATIONS ON THE RADIAL PORTION OF THE IMPELLER; z = -1.1960; SUCTION SURFACE.

8.0 BACKSWEPT IMPELLER PROBLEM

A proof of principle impeller problem was run to check out the turbulence model which had been incorporated in the IFFC code. The impeller geometry, which was selected by Dr. T. Katsanis of the NASA Lewis Research Center, was that of an advanced backswept compressor developed by CREARE, Inc. The basic geometry and design operating conditions of the backswept impeller problem were as follows:

Rotational speed	75000 RPM
Tip diameter	15.95 Cm. (6.28 in)
Design pressure ratio	8:1
Inlet total pressure	2117 lb/ft ^{2}
Inlet total temperature	519 $^\circ$ R
Impeller tip speed	2055 ft/sec
Discharge Reynolds Number*	1.43×10^6

The rotor geometry is presented in the cylindrical coordinates r, θ, X_3 in Figures 23 and 24. Figure 23 presents traces of the hub and shroud lines in a half-plane through the axis of the impeller, i.e., a meridional plane. The hub and shroud radial coordinates are presented as a function of axial distance. The hub and shroud lines extend upstream of the inducer and above the discharge so that the region of calculation contains them both. The angular coordinates of the pressure and suction blade surfaces are shown in Figure 24 as functions of axial distance X_3. The solid lines indicate traces of the blades on the hub, while the dashed lines indicate shroud blade traces. The regions upstream of the inducer and downstream of the hub are also indicated in Figure 24.

A fine finite difference mesh was incorporated in order to adequately define the boundary layer. The mesh consisted of 30 J-lines (streamline-line) and 101 K-lines (potential-like). A grating factor (g) of 1.06 was used to space the J-lines. The hub plane mesh is illustrated in Figure 25 and the blade-to-blade surface 23% of the distance between hub and shroud is shown in Figure 26.

The invicid flow solution for the backswept impeller was solved using the meridional finite difference method of Reference 39. The hub inviscid flow field, which serves as the zeroth iterate for the viscous calculation, is shown in Figure 27. It is noted that at the inducer inlet the relative velocity is roughly the same on both the blade pressure and suction surfaces. The velocity profile remains relatively

*Reynolds number based on an average inviscid relative velocity along the hub and distance along the hub.

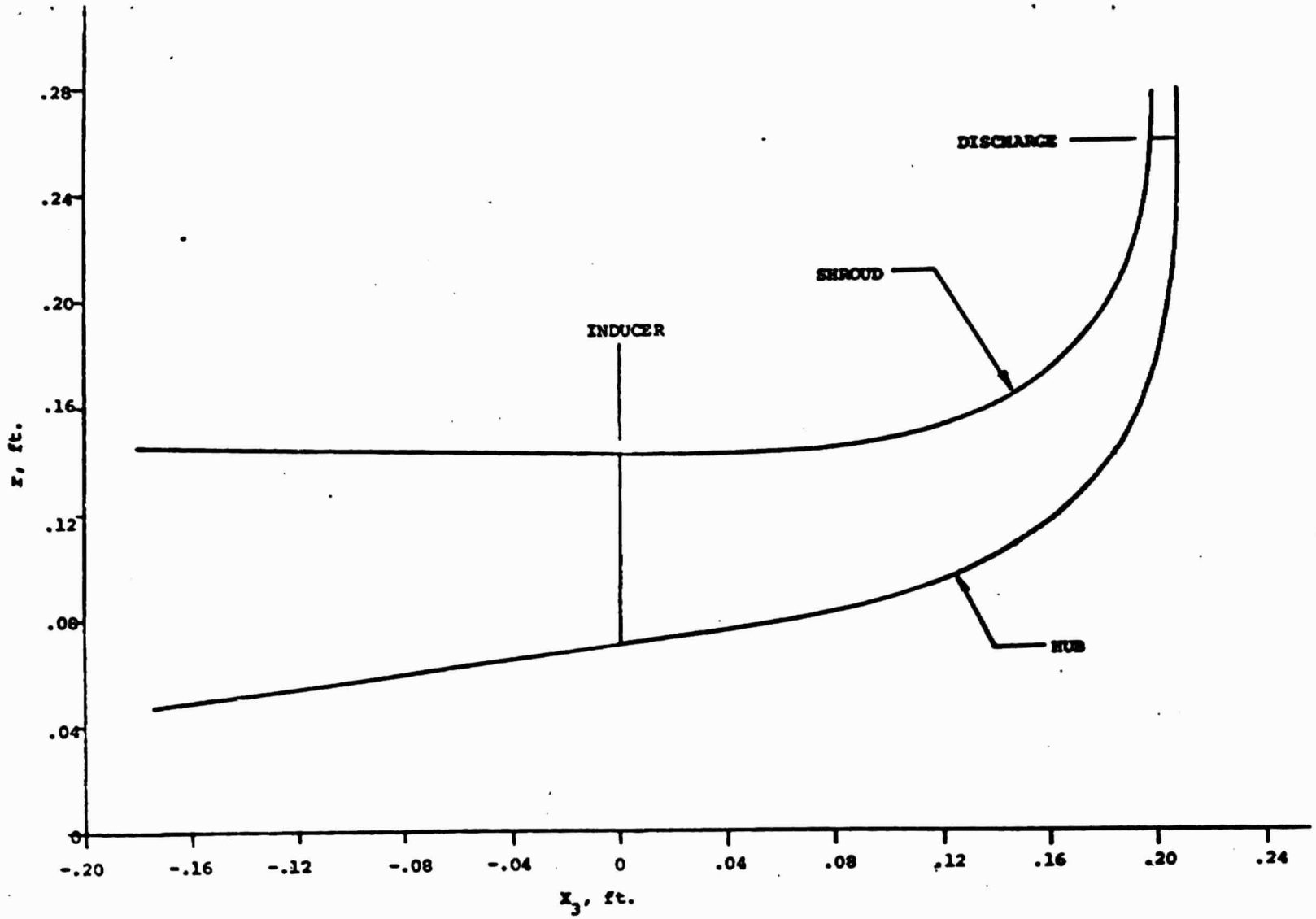

FIGURE 23: RADIAL AND AXIAL COORDINATES OF THE HUB AND SHROUD LINES OF THE IMPELLER.

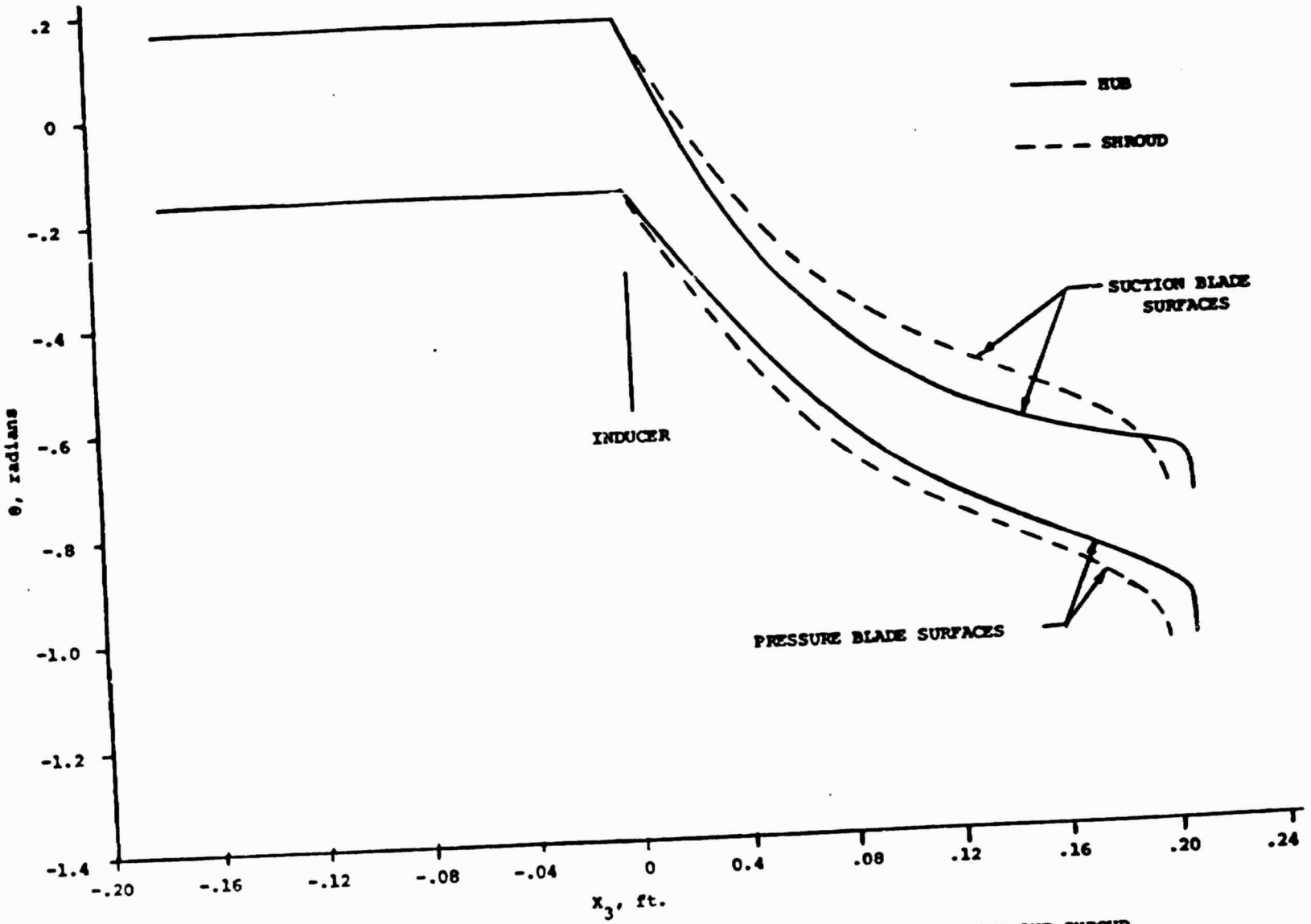

FIGURE 24: ANGULAR AND AXIAL COORDINATES OF THE TRACES OF THE BLADING SURFACES ON THE HUB AND SHROUD.

ORIGINAL PAGE IS
OF POOR QUALITY

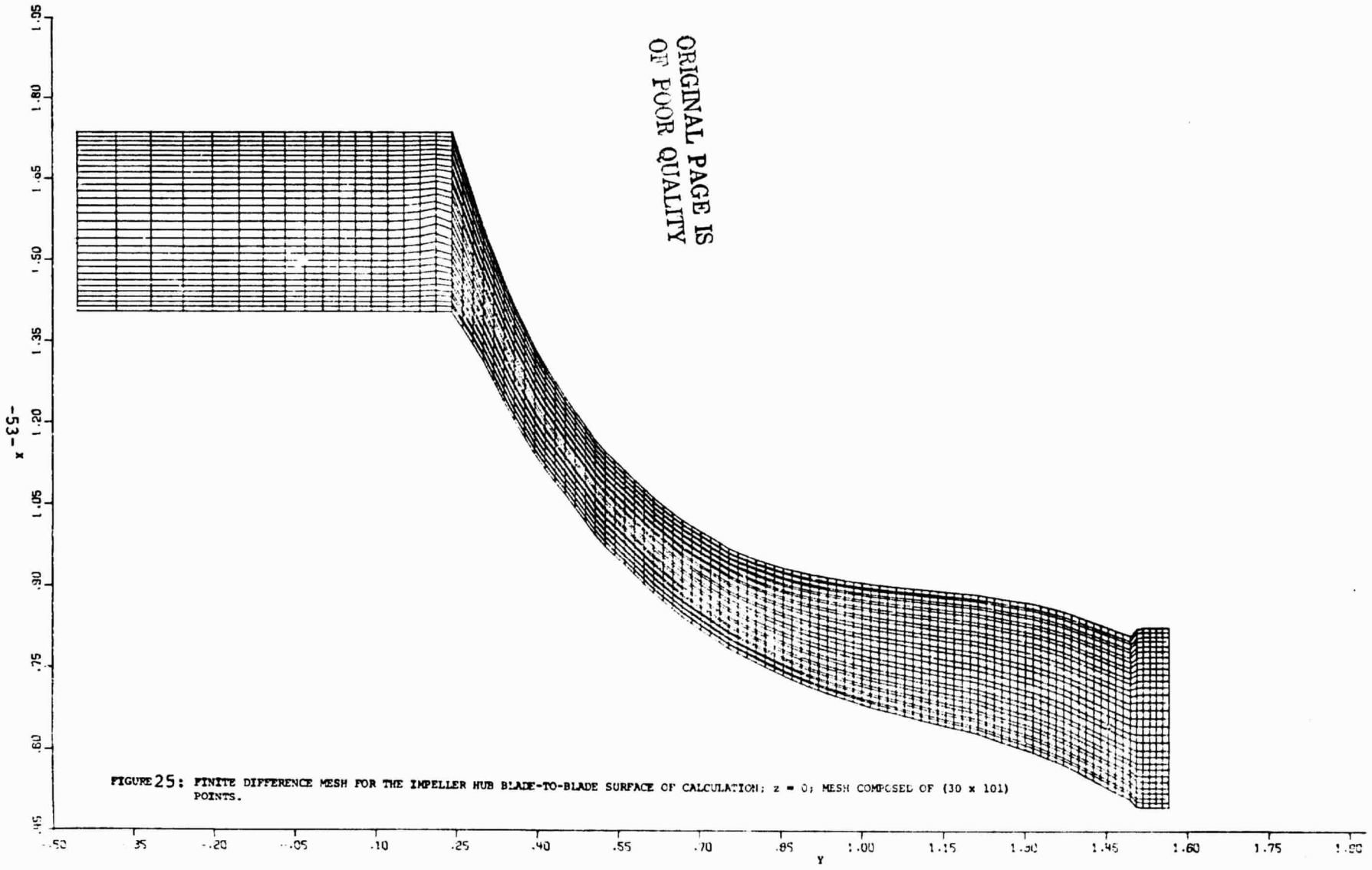

FIGURE 25: FINITE DIFFERENCE MESH FOR THE IMPELLER HUB BLADE-TO-BLADE SURFACE OF CALCULATION; z = 0; MESH COMPOSED OF (30 x 101) POINTS.

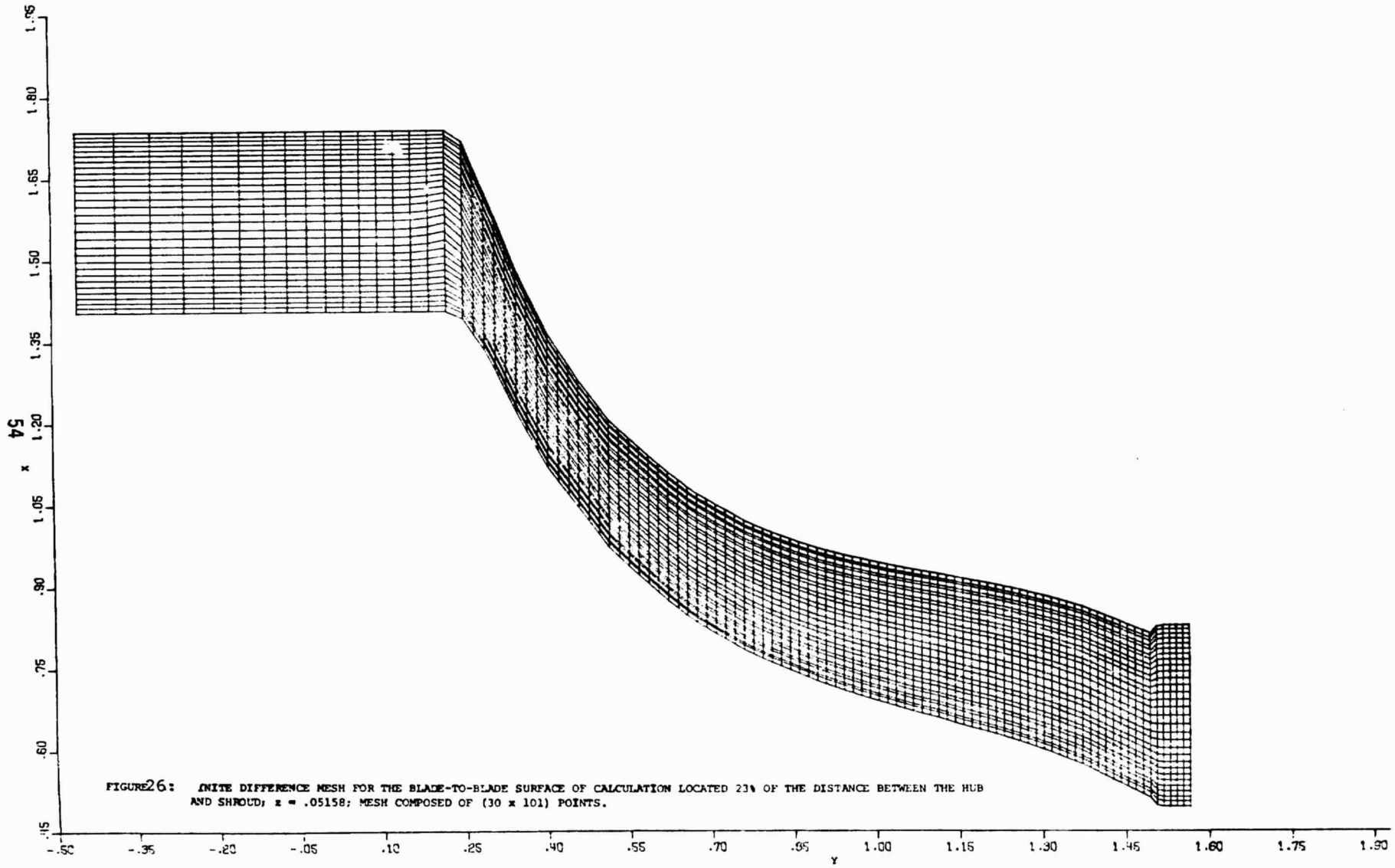

FIGURE 26: FINITE DIFFERENCE MESH FOR THE BLADE-TO-BLADE SURFACE OF CALCULATION LOCATED 23% OF THE DISTANCE BETWEEN THE HUB AND SHROUD; z = .05158; MESH COMPOSED OF (30 x 101) POINTS.

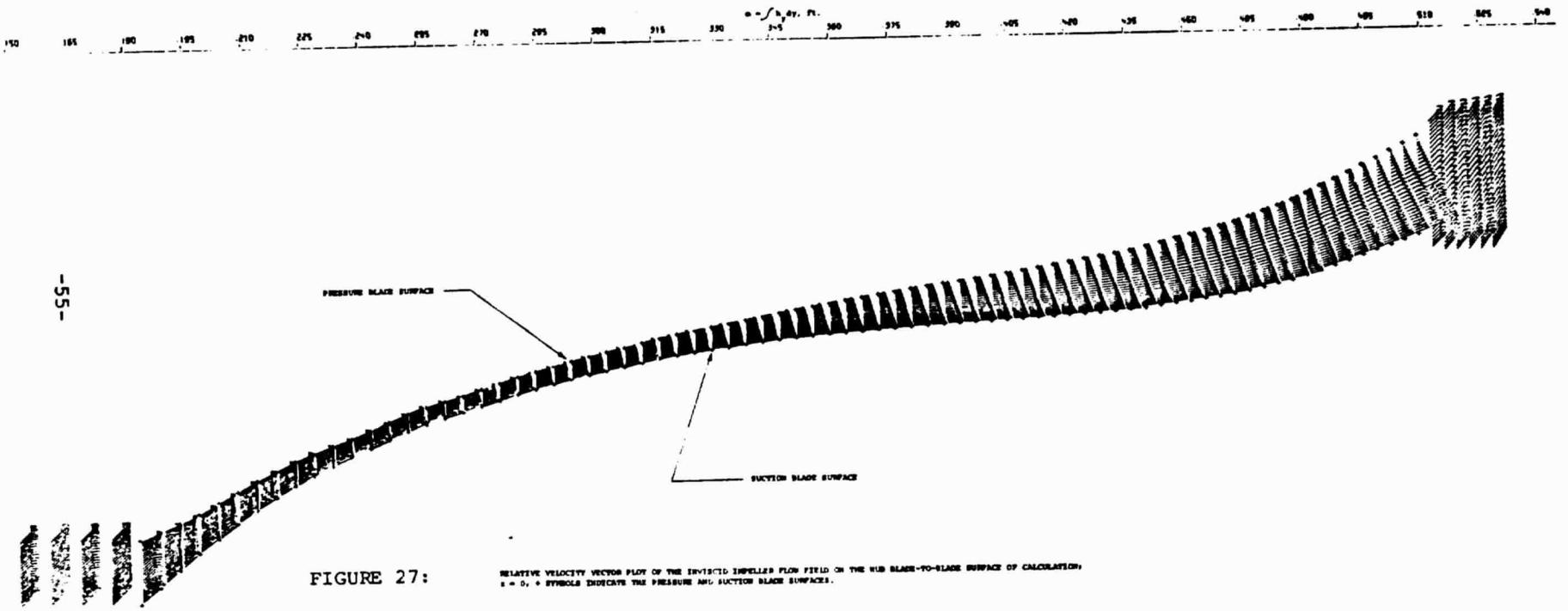

FIGURE 27: RELATIVE VELOCITY VECTOR PLOT OF THE INVISCID IMPELLER FLOW FIELD ON THE HUB BLADE-TO-BLADE SURFACE OF CALCULATION; s = 0, + SYMBOLS INDICATE THE PRESSURE AND SUCTION BLADE SURFACES.

constant until approximately half way through the channel, when the suction blade velocity becomes significantly larger than the pressure surface velocity. This result is not in agreement with observed flow phenomena for centrifugal impellers. That is, the low-flow region is observed to occur at the suction blade surface near the discharge.

Substantially different results were obtained for the viscous solution to the backswept impeller problem. Relative velocity plots for the blade-to-blade surface 19% of the distance from the hub to shroud are shown in Figures 28-30. The inducer region, which is shown in Figure 29, has a slight separation on the blade suction surface near the inlet. At the discharge the flow velocities near the suction and pressure surfaces and across the channel are nearly equal, whereas the inviscid calculation (Figure 27) predicted very low velocities on the pressure surface. There is no indication of a suction surface separation at the discharge like that obtained in the radial impeller problem. No conclusion can be drawn with regard to the effectiveness of backsweep in reducing or eliminating flow separation because the radial impeller was calculated for a very low Reynolds number (5000) with laminar flow, whereas the backswept impeller was calculated at a high Reynolds number (1.43×10^6) with the turbulence model operational.

The viscous solution for the surface 72% of the distance between hub and shroud produced relative velocity profiles shown in Figures 31-33. The results were similar to the 19% surface except that the velocity gradient near the suction blade surface was not so pronounced. Also, except at the inlet, the velocity profiles were relatively uniform from blade-to-blade and continued to be so all the way to the discharge.

The solution for the 98% surface, shown in Figures 34 and 35 produced results which were similar to the 72% surface calculation. Likewise, the 99.95% surface, which is shown in Figure 36, looks much like the 98% surface, although the 99.95% surface is located in the tip clearance region. There is no blade to influence flow at this surface, but the relative velocity plot shows that the blade viscous effects are felt despite this fact. Indeed, the relative velocity (boundary layer) profile near the hypothetical blade surface is much like one would expect if a blade were present.

The static pressure contour plot for the 98% blade-to-blade surface (z = .22451 radians) is shown in Figure 37. The static pressure ratio shown is referenced to the inlet stagnation pressure (P_o). There is a region of low static pressure near the inducer inlet ($P/P_o = .8$) on the suction side of the channel, which indicates a region of accelerated

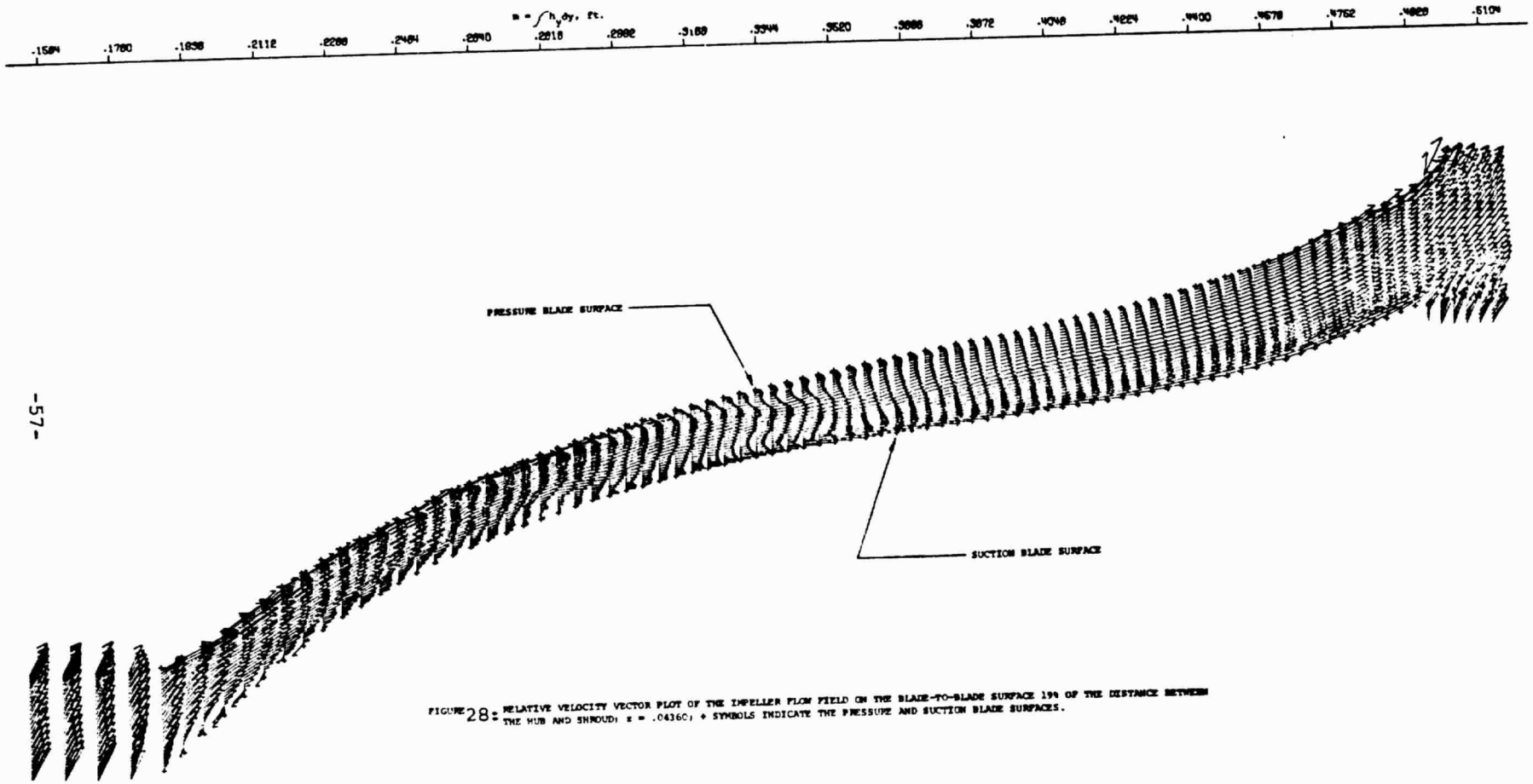

FIGURE 28: RELATIVE VELOCITY VECTOR PLOT OF THE IMPELLER FLOW FIELD ON THE BLADE-TO-BLADE SURFACE 19% OF THE DISTANCE BETWEEN THE HUB AND SHROUD; z = .04360; + SYMBOLS INDICATE THE PRESSURE AND SUCTION BLADE SURFACES.

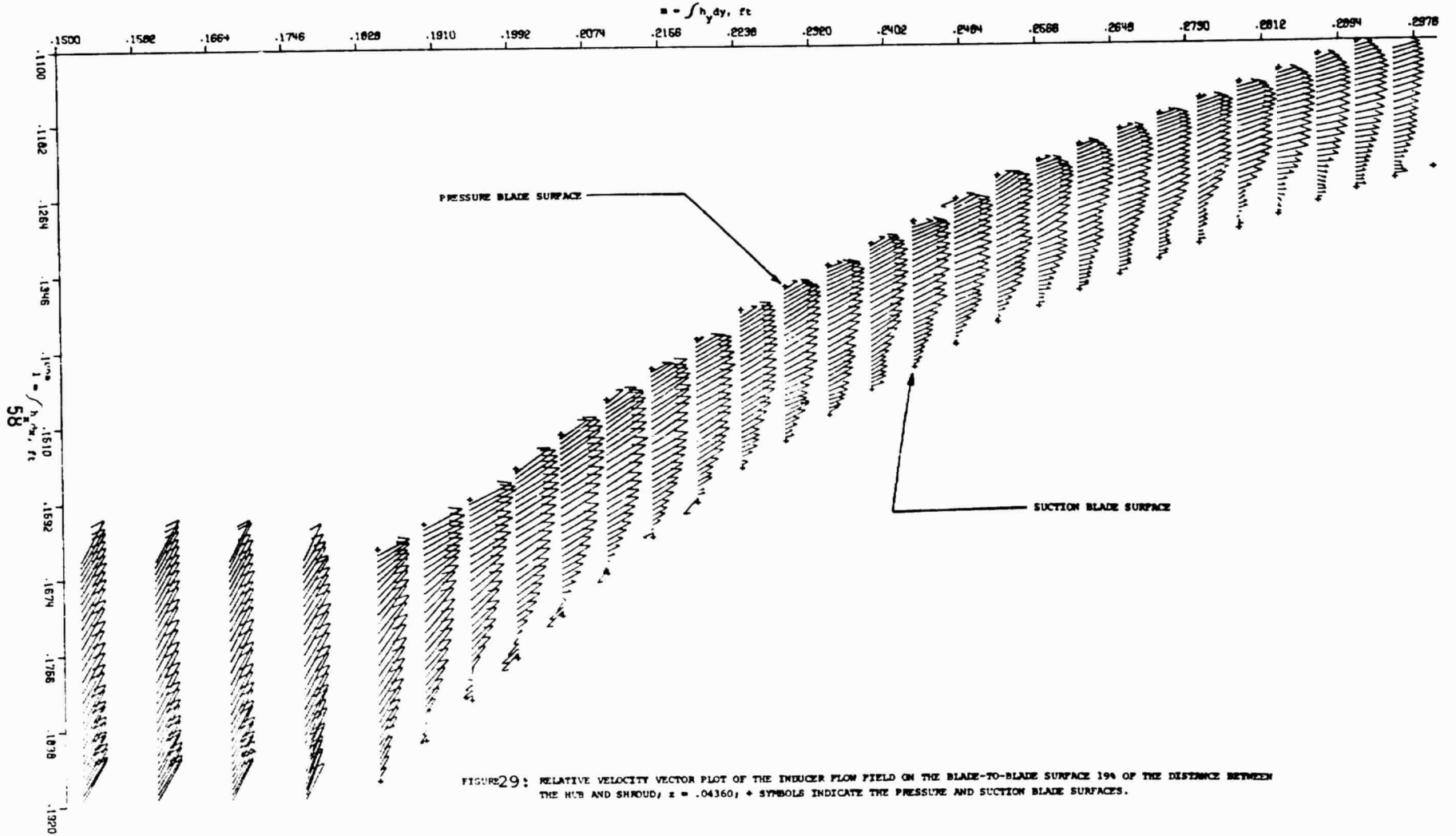

FIGURE 29: RELATIVE VELOCITY VECTOR PLOT OF THE INDUCER FLOW FIELD ON THE BLADE-TO-BLADE SURFACE 19% OF THE DISTANCE BETWEEN THE HUB AND SHROUD; z = .04360; + SYMBOLS INDICATE THE PRESSURE AND SUCTION BLADE SURFACES.

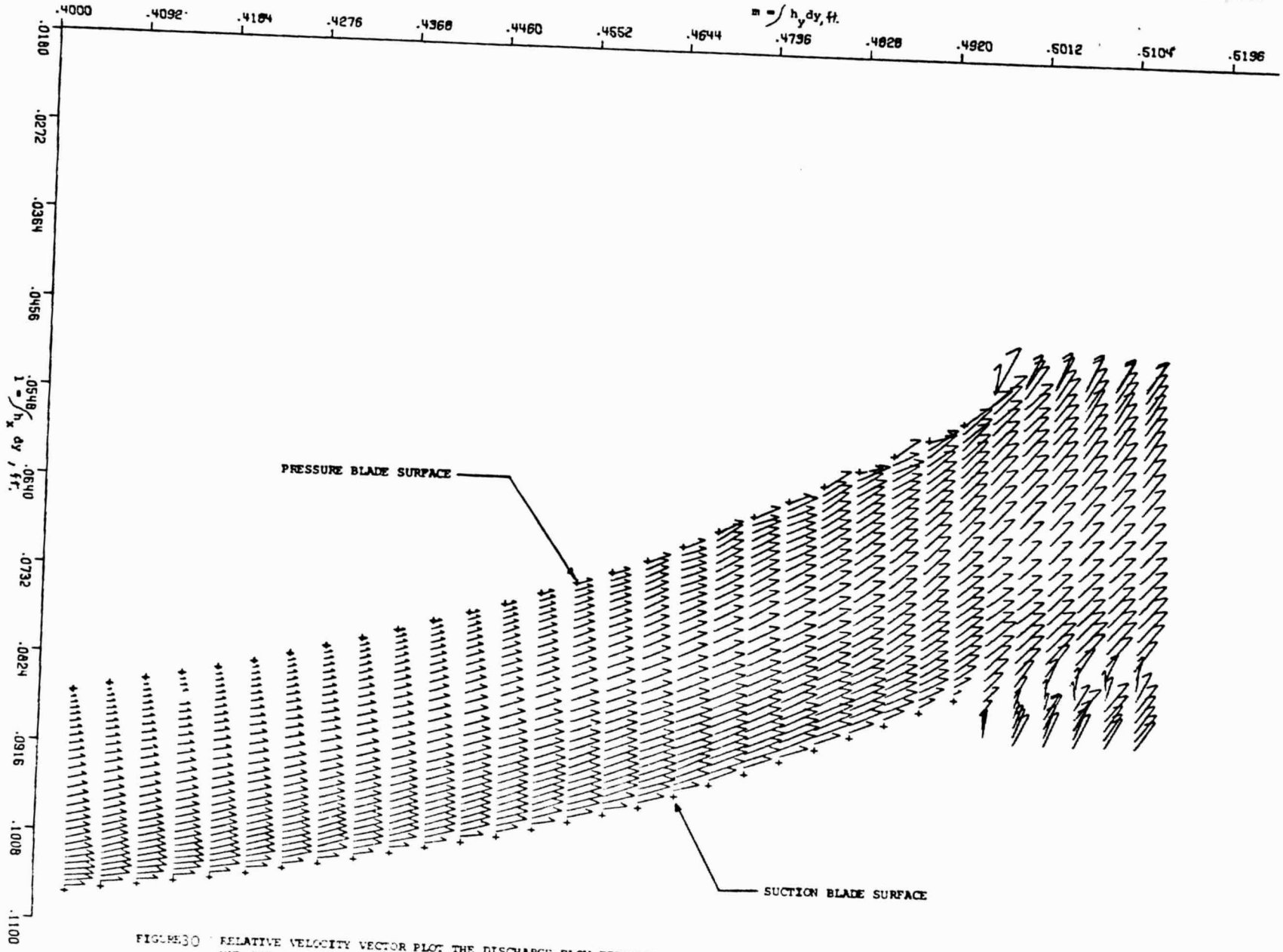

FIGURE 30 RELATIVE VELOCITY VECTOR PLOT THE DISCHARGE FLOW FIELD ON THE BLADE-TO-BLADE SURFACE 19% OF THE DISTANCE BETWEEN THE HUB AND THE SHROUD; z = .04760; + SYMBOLS INDICATE THE PRESSURE AND SUCTION BLADE SURFACES.

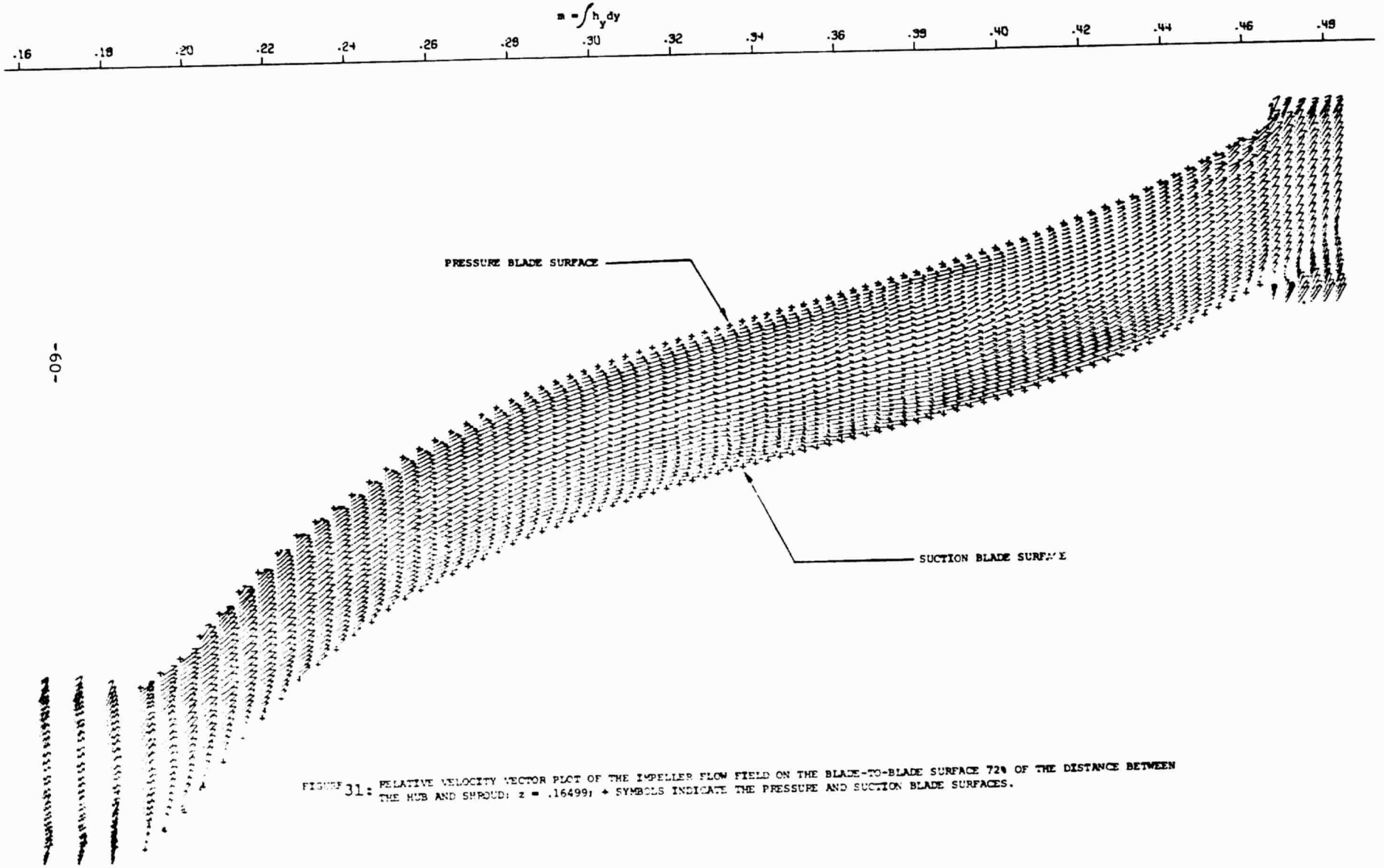

FIGURE 31: RELATIVE VELOCITY VECTOR PLOT OF THE IMPELLER FLOW FIELD ON THE BLADE-TO-BLADE SURFACE 72% OF THE DISTANCE BETWEEN THE HUB AND SHROUD; z = .16499; + SYMBOLS INDICATE THE PRESSURE AND SUCTION BLADE SURFACES.

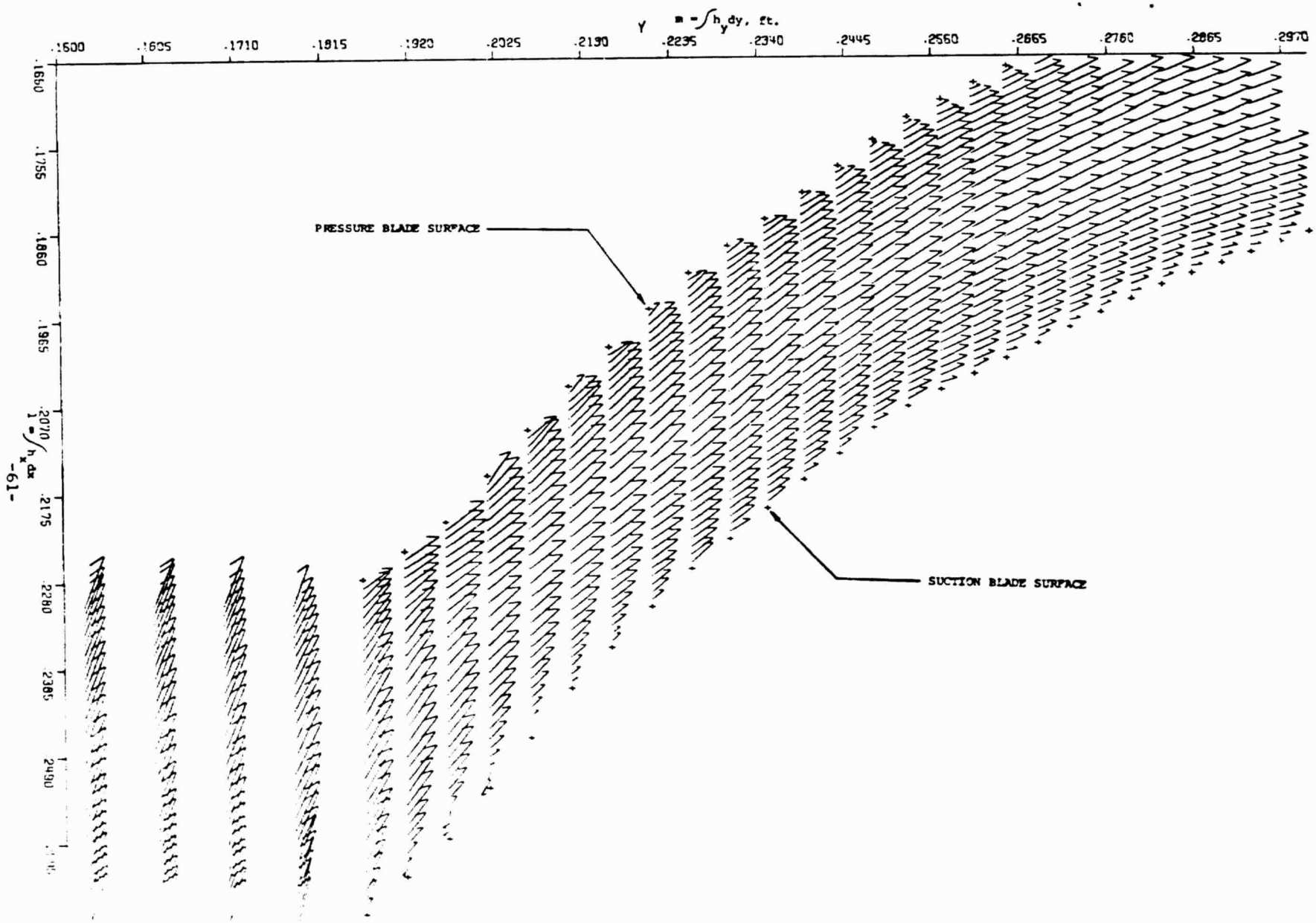

FIGURE 5.1: RELATIVE VELOCITY VECTOR PLOT OF THE INVISCID FLOW FIELD ON THE BLADE-TO-BLADE SURFACE 70% OF THE DISTANCE BETWEEN THE HUB AND SHROUD. Z = .116439". + SYMBOLS INDICATE THE PRESSURE AND SUCTION BLADE SURFACES.

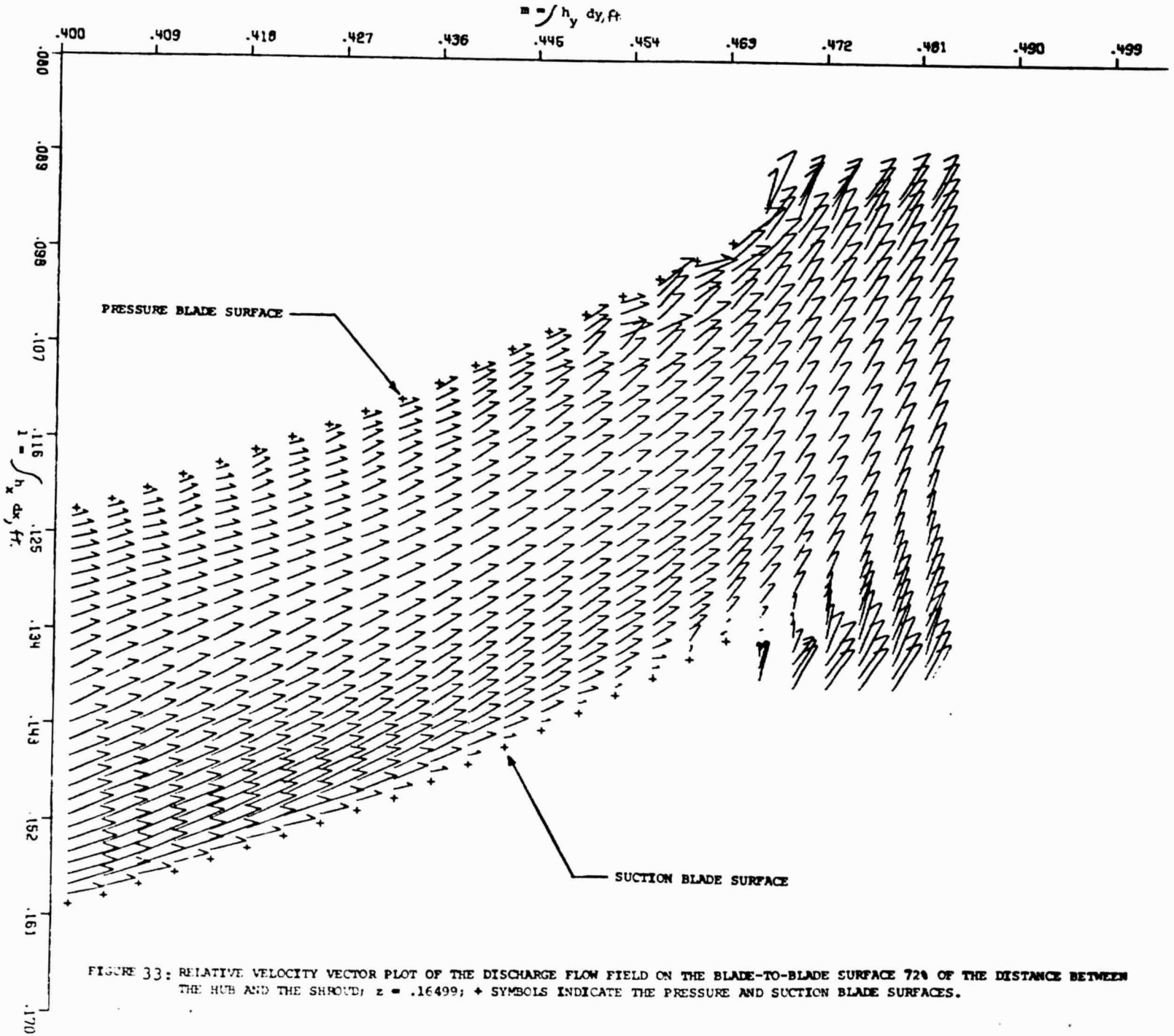

FIGURE 33: RELATIVE VELOCITY VECTOR PLOT OF THE DISCHARGE FLOW FIELD ON THE BLADE-TO-BLADE SURFACE 72% OF THE DISTANCE BETWEEN THE HUB AND THE SHROUD; z = .16499; + SYMBOLS INDICATE THE PRESSURE AND SUCTION BLADE SURFACES.

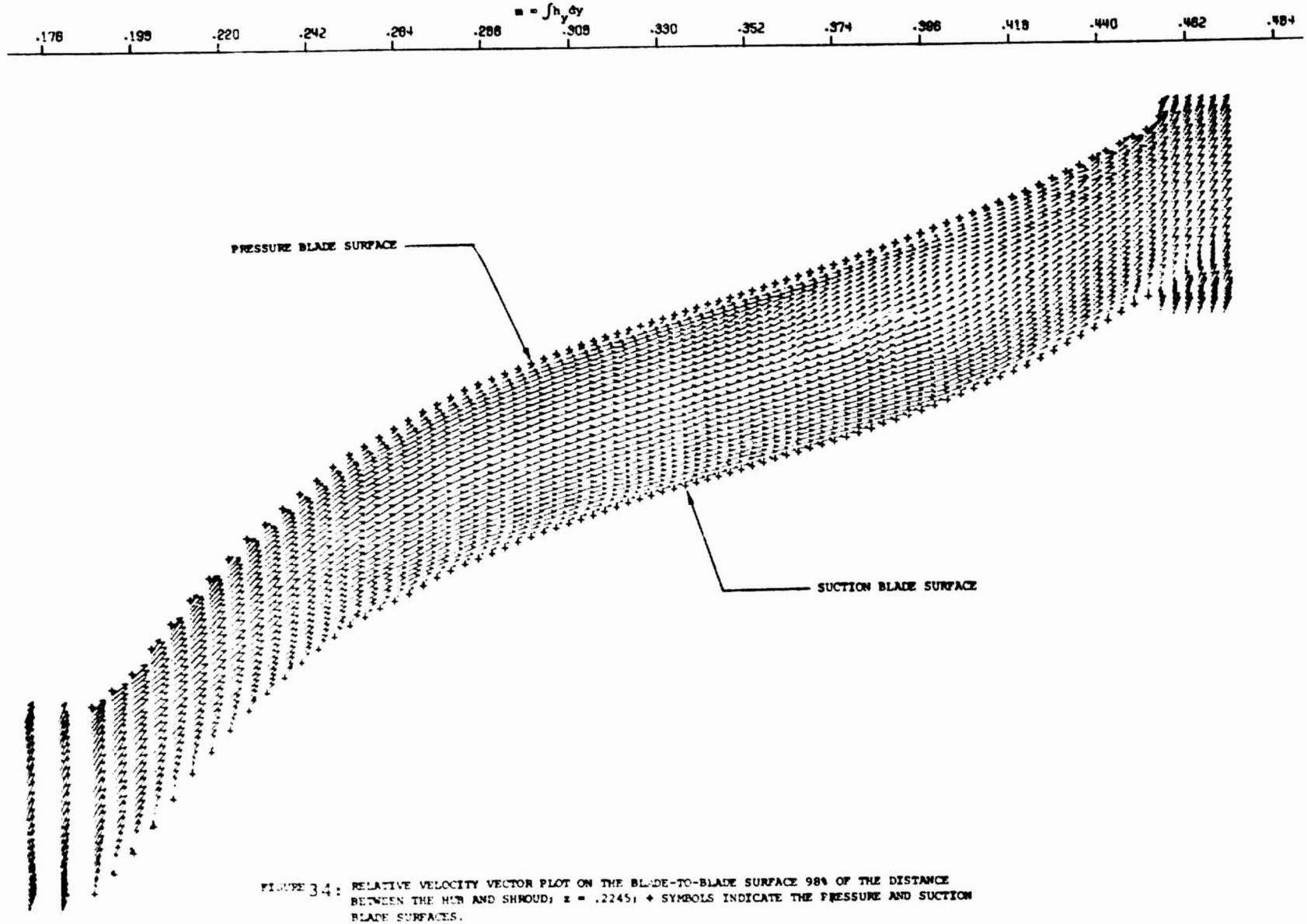

FIGURE 3.4: RELATIVE VELOCITY VECTOR PLOT ON THE BLADE-TO-BLADE SURFACE 98% OF THE DISTANCE BETWEEN THE HUB AND SHROUD; z = .2245; + SYMBOLS INDICATE THE PRESSURE AND SUCTION BLADE SURFACES.

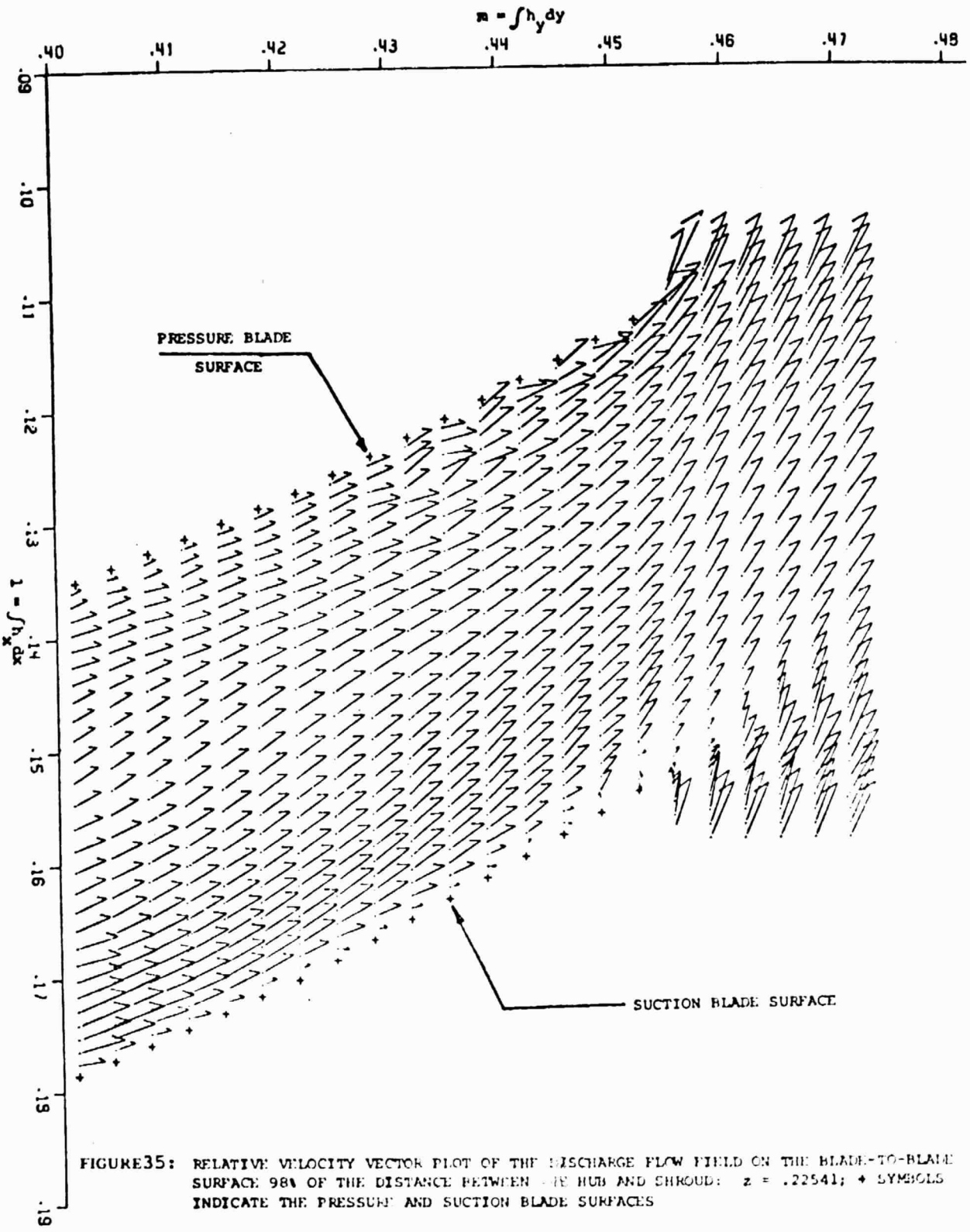

FIGURE35: RELATIVE VELOCITY VECTOR PLOT OF THE DISCHARGE FLOW FIELD ON THE BLADE-TO-BLADE SURFACE 98% OF THE DISTANCE BETWEEN THE HUB AND SHROUD: z = .22541; + SYMBOLS INDICATE THE PRESSURE AND SUCTION BLADE SURFACES

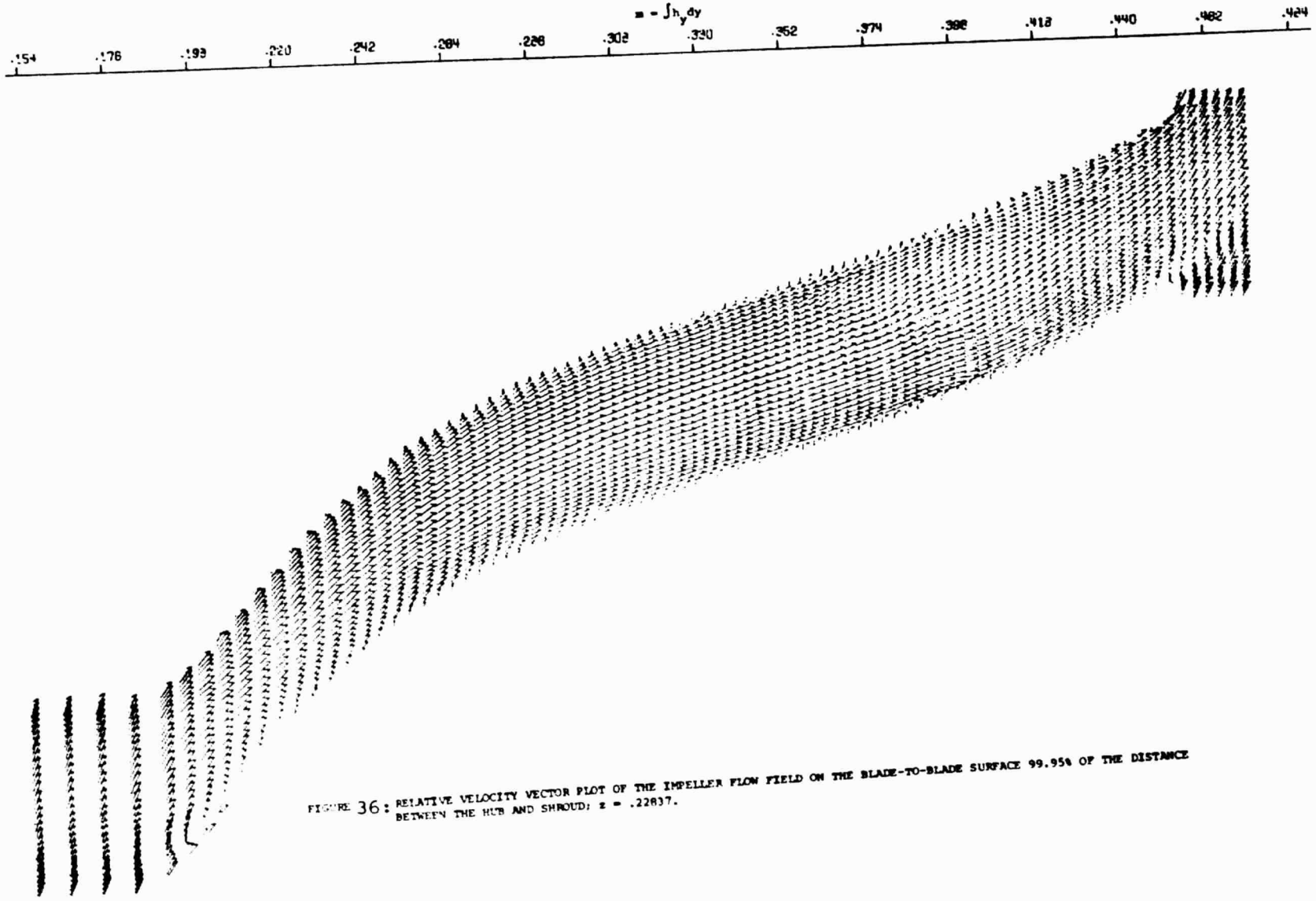

FIGURE 36: RELATIVE VELOCITY VECTOR PLOT OF THE IMPELLER FLOW FIELD ON THE BLADE-TO-BLADE SURFACE 99.95% OF THE DISTANCE BETWEEN THE HUB AND SHROUD; z = .22837.

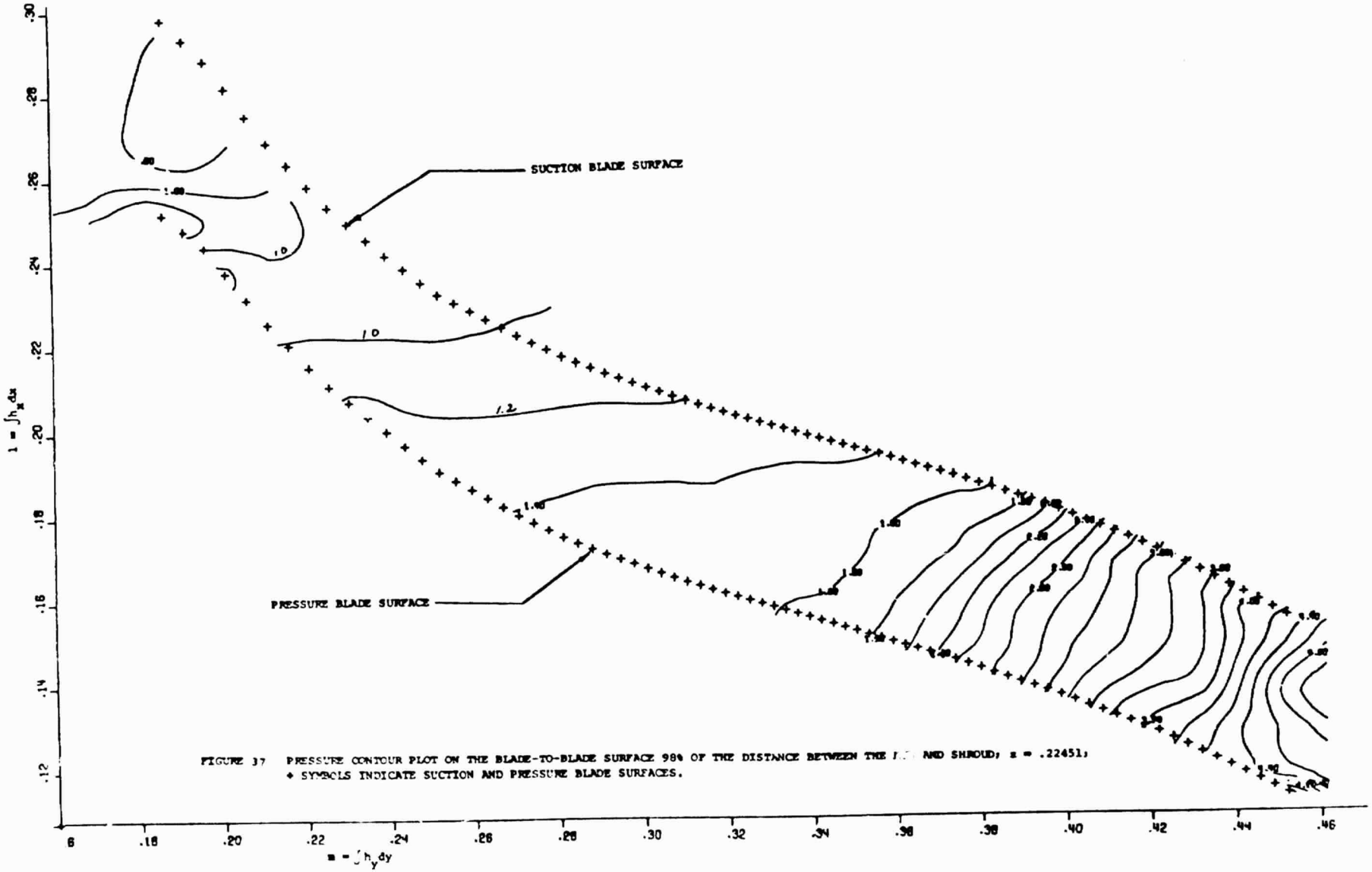

FIGURE 37 PRESSURE CONTOUR PLOT ON THE BLADE-TO-BLADE SURFACE 98% OF THE DISTANCE BETWEEN THE [illegible] AND SHROUD; z = .22451; + SYMBOLS INDICATE SUCTION AND PRESSURE BLADE SURFACES.

flow due to the airfoil. The inducer or axial-flow portion of the channel decelerates the flow steadily until there is a static pressure ratio of about 1.4 as flow begins to enter the radial portion of the rotor. The rate of static pressure rise thereafter is increased rapidly because of the rotor centrifugal energy input. Finally, at the discharge an average channel static pressure ratio of about 4.6:1 is achieved and there is a relatively uniform profile across the channel. There is no separation indicated because the static pressure rise continues throughout the radial portion of the flowpath. This is attributed to the stabilizing influence of the backswept blading.

Very similar results are illustrated for the 99.95% surface (Figure 38), which is located in the tip clearance region at the shroud. In Figure 39, hub, 19% and 77% surface calculations of suction surface static pressure ratio (P/P_o) as a function of Y (axial coordinate) are shown. These results also indicate the absence of separated flow because diffusion continues all the way to the discharge.

Relative velocity ratio contour plots are presented in Figures 40-43 for the blade-to-blade surfaces located 19%, 72%, 92%, and 99.95% of the distance from the hub to the shroud. The relative velocity ratio V/V*, is the ratio of flow velocity to critical flow velocity according to the following*:

$$V/V^* = M \left[\frac{\gamma+1}{2+(\gamma-1)M^2}\right]^{0.5}$$

At the 19% surface (Figure 40) the contour plot indicates roughly sonic relative velocities at the inducer inlet with diffusion down to a velocity ratio of .4 - .6 at the impeller discharge. The contour plot for the 92% surface, which is shown in Figure 42, suggests that most of the flow at the inducer tip is at a relative velocity ratio of 1.2 or higher. A smooth, even diffusion rate is indicated, and a relative velocity ratio of roughly .6 is obtained at the discharge.

Contour plots of relative total pressure ratio are shown in Figures 44-46. Relative total pressure ratio is defined as the stagnation pressure calculated at a given point divided by the ideal stagnation pressure which would have occured if the process were isentropic.

*Where M is defined as the ratio of the local relative velocity and the local sound speed.

The contour plot of the 19% surface, shown in Figure 44, indicates that for most of the flow the relative total pressure begins to deviate from ideal conditions at about 40% of the meridional distance through the passage. At the discharge a value of the relative total pressure ratio of roughly .92 - .96 is calculated for flow in the mid-passage. The regions of low total pressure are observed to be near the suction and pressure blade surfaces. Similar results are indicated for the 72% and 92% surfaces shown in Figures 45 and 46. At the 98% surface it is observed that a region of relatively high (.96 - .98) total pressure ratio occurs at the discharge in the mid passage region. Again the main flow losses are calculated to occur near the blade boundaries.

An independent boundary layer computation, using Mager's integral turbulent boundary layer analysis [40], was performed to verify the numerical separation characteristic. The calculated suction blade momentum thickness Ⓗ in the boundary layer for the 19% and 77% surface calculations is shown in Figures 47 and 48. Since the ratio of Ⓗ to the initial value $Ⓗ_i$ stays relatively constant downstream of the initial inducer portion of the channel, there is no separation and no reduction of static pressure rise capability. Nowhere does the suction blade momuntum thickness go below its initial value; hence, turbulent boundary layer theory indicates that the suction blade flow should not separate.

Distributions of the ratio of eddy viscosity to the molecular viscosity along the suction blade surface are presented in Figure 49. The boundary layer turbulence is generally increasing along the blade, especially in the radial flow region prior to discharge.

The viscous calculation of the backswept impeller flow field with the IFFC blade-to-blade computer program ran 8073 cycles or surfaces from hub to shroud. The 30 x 101 mesh consisted of 3030 zones and required 9.3 hours of computer time on the CDC 7600 computer to complete the problem. It is recommended that additional efforts be made to reduce the computational time requirement to make this solution a practical tool for utilization by the compressor aerodynamicist.

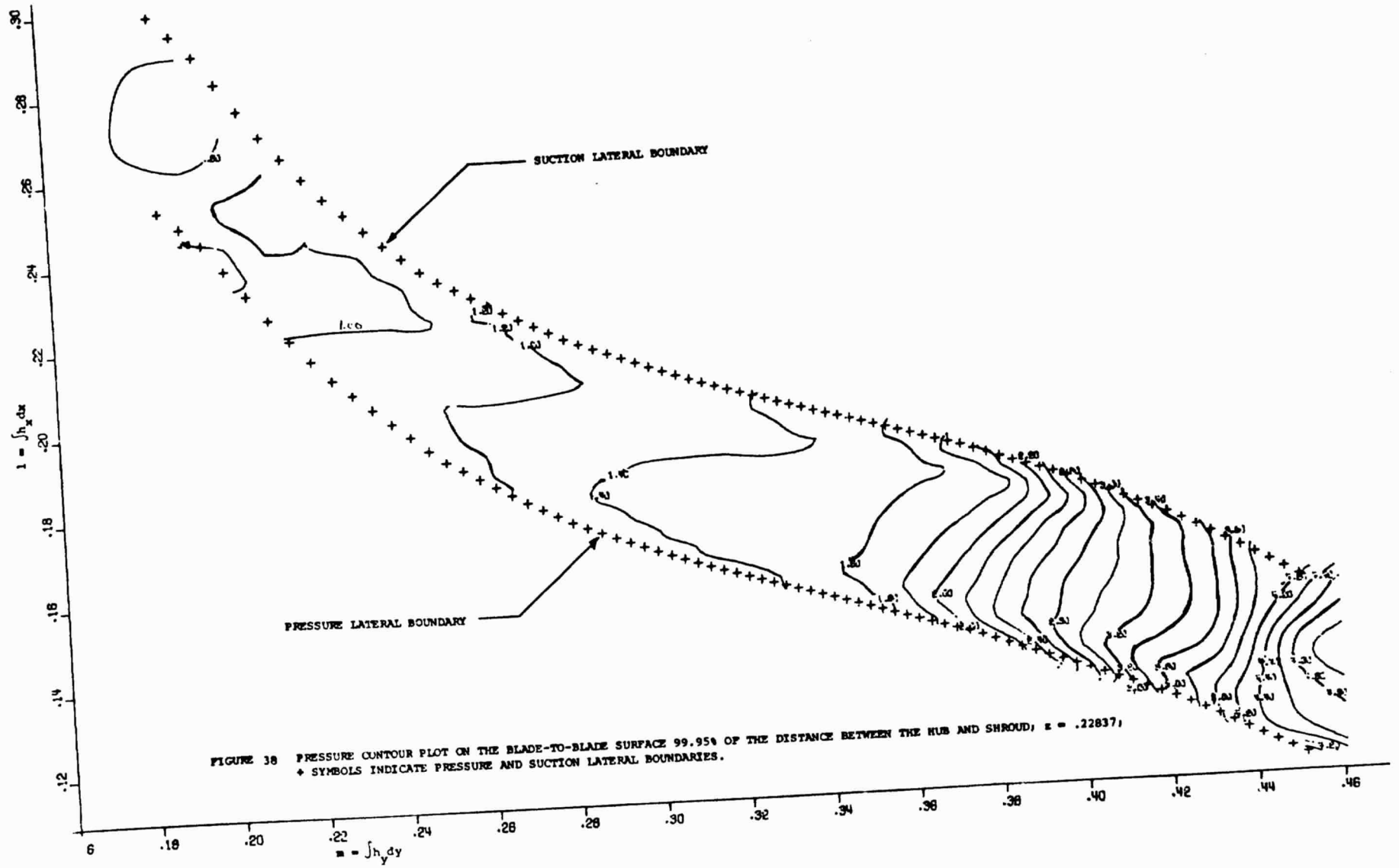

FIGURE 38 PRESSURE CONTOUR PLOT ON THE BLADE-TO-BLADE SURFACE 99.95% OF THE DISTANCE BETWEEN THE HUB AND SHROUD; z = .22837; + SYMBOLS INDICATE PRESSURE AND SUCTION LATERAL BOUNDARIES.

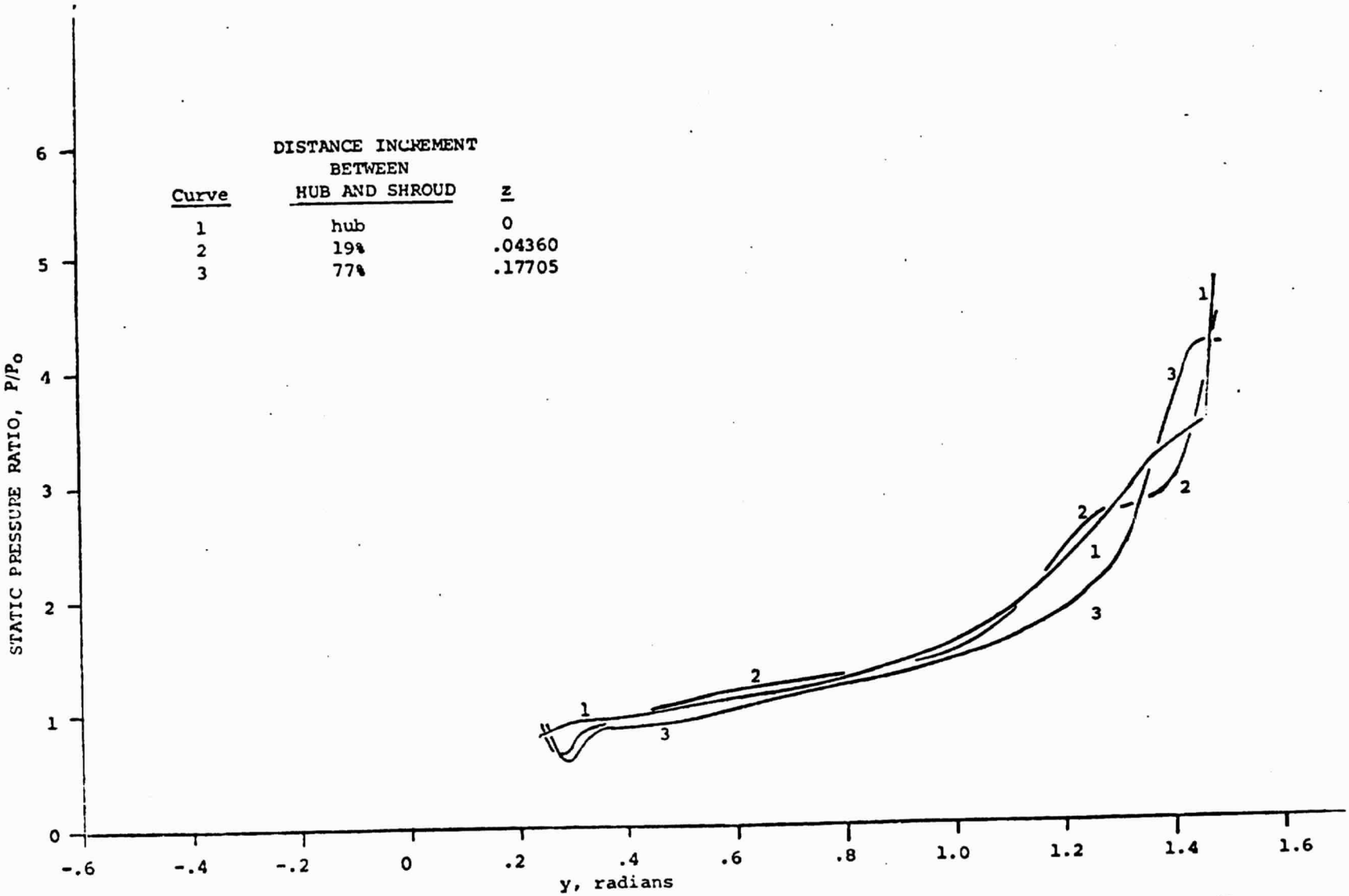

FIGURE 39: STATIC PRESSURE DISTRIBUTIONS ALONG THE SUCTION BLADE SURFACE; P_o REPRESENTS THE AMBIENT STAGNATION PRESSURE IN A LABORATORY FRAME

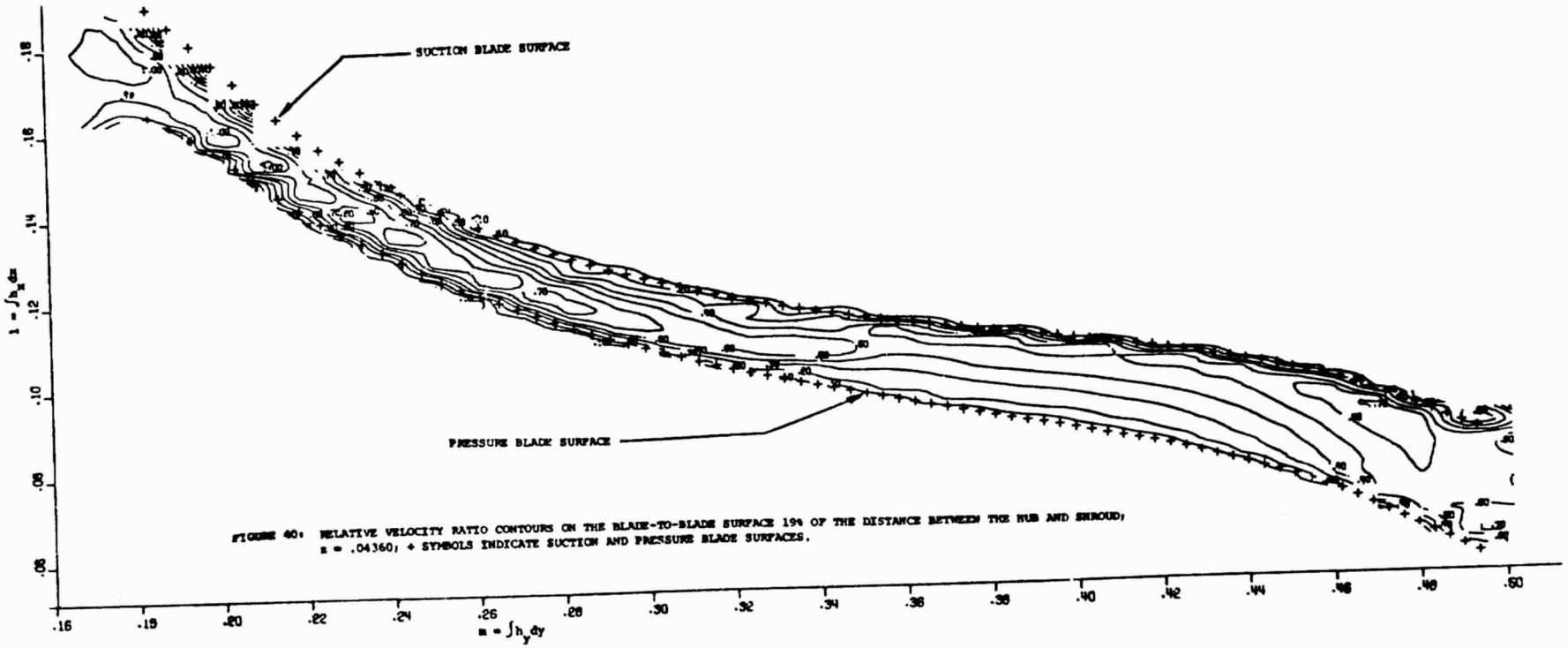

FIGURE 40: RELATIVE VELOCITY RATIO CONTOURS ON THE BLADE-TO-BLADE SURFACE 19% OF THE DISTANCE BETWEEN THE HUB AND SHROUD; z = .04360; + SYMBOLS INDICATE SUCTION AND PRESSURE BLADE SURFACES.

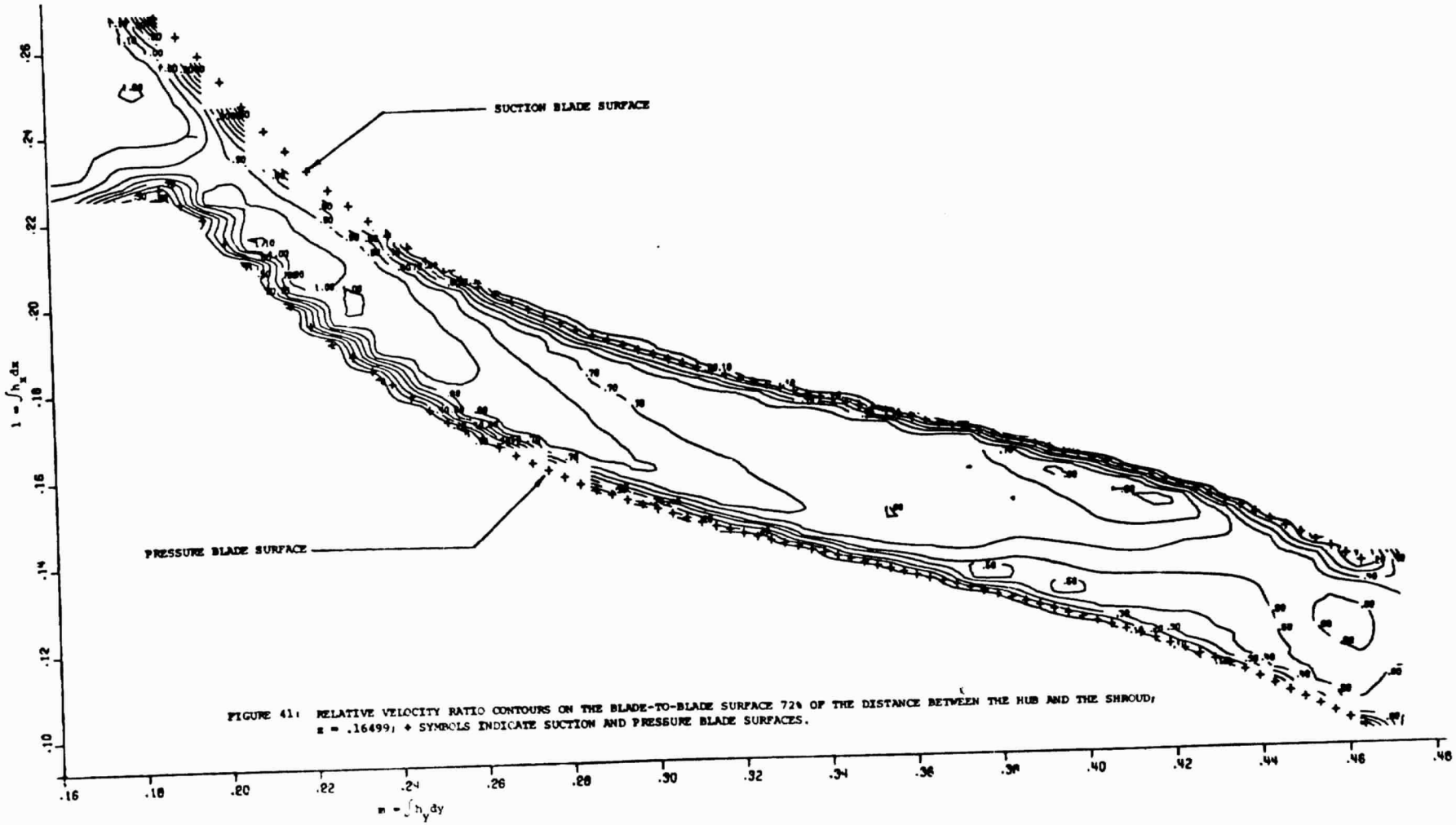

FIGURE 41: RELATIVE VELOCITY RATIO CONTOURS ON THE BLADE-TO-BLADE SURFACE 72% OF THE DISTANCE BETWEEN THE HUB AND THE SHROUD; z = .16499; + SYMBOLS INDICATE SUCTION AND PRESSURE BLADE SURFACES.

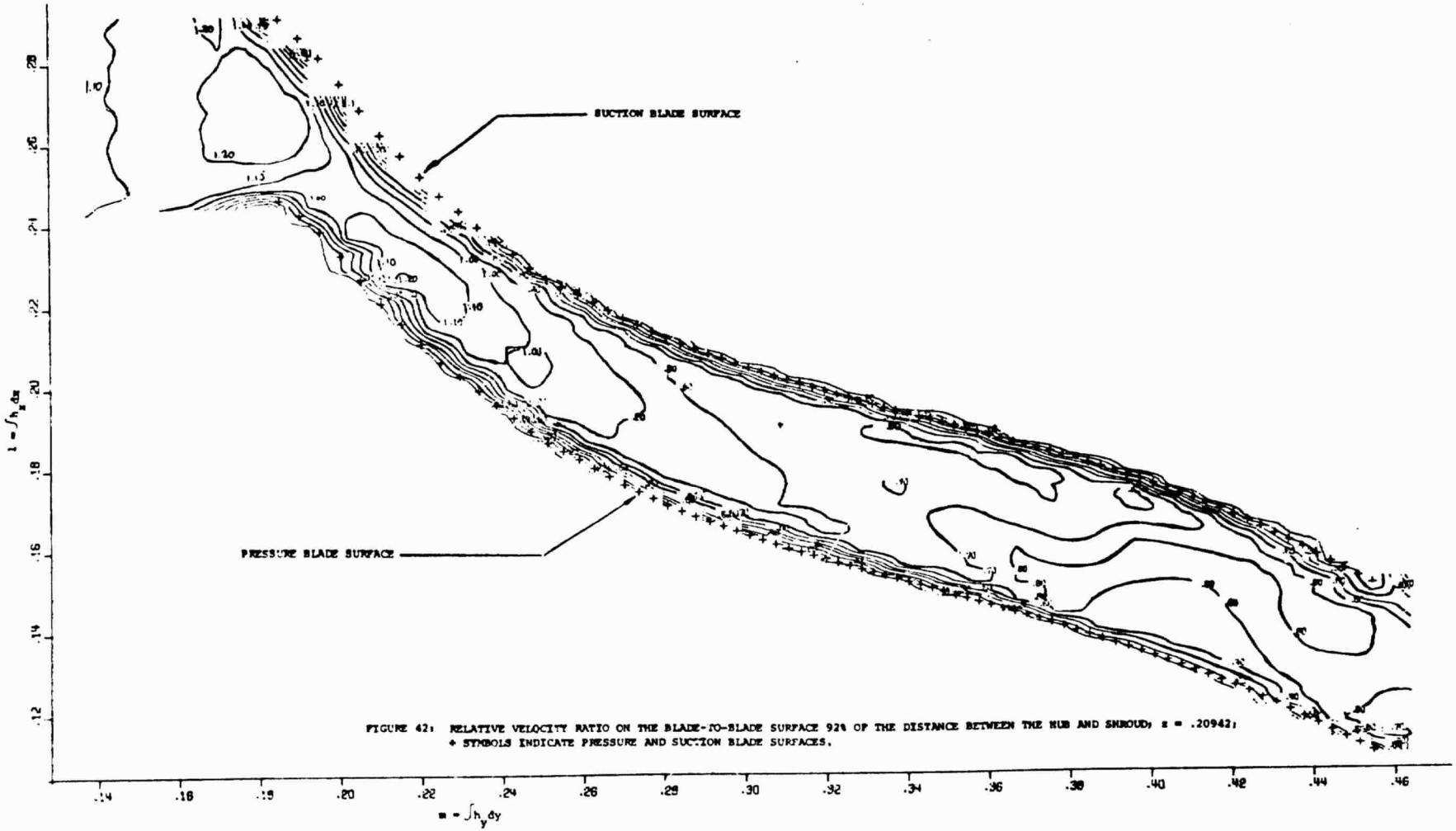

FIGURE 42: RELATIVE VELOCITY RATIO ON THE BLADE-TO-BLADE SURFACE 92% OF THE DISTANCE BETWEEN THE HUB AND SHROUD; z = .20942; + SYMBOLS INDICATE PRESSURE AND SUCTION BLADE SURFACES.

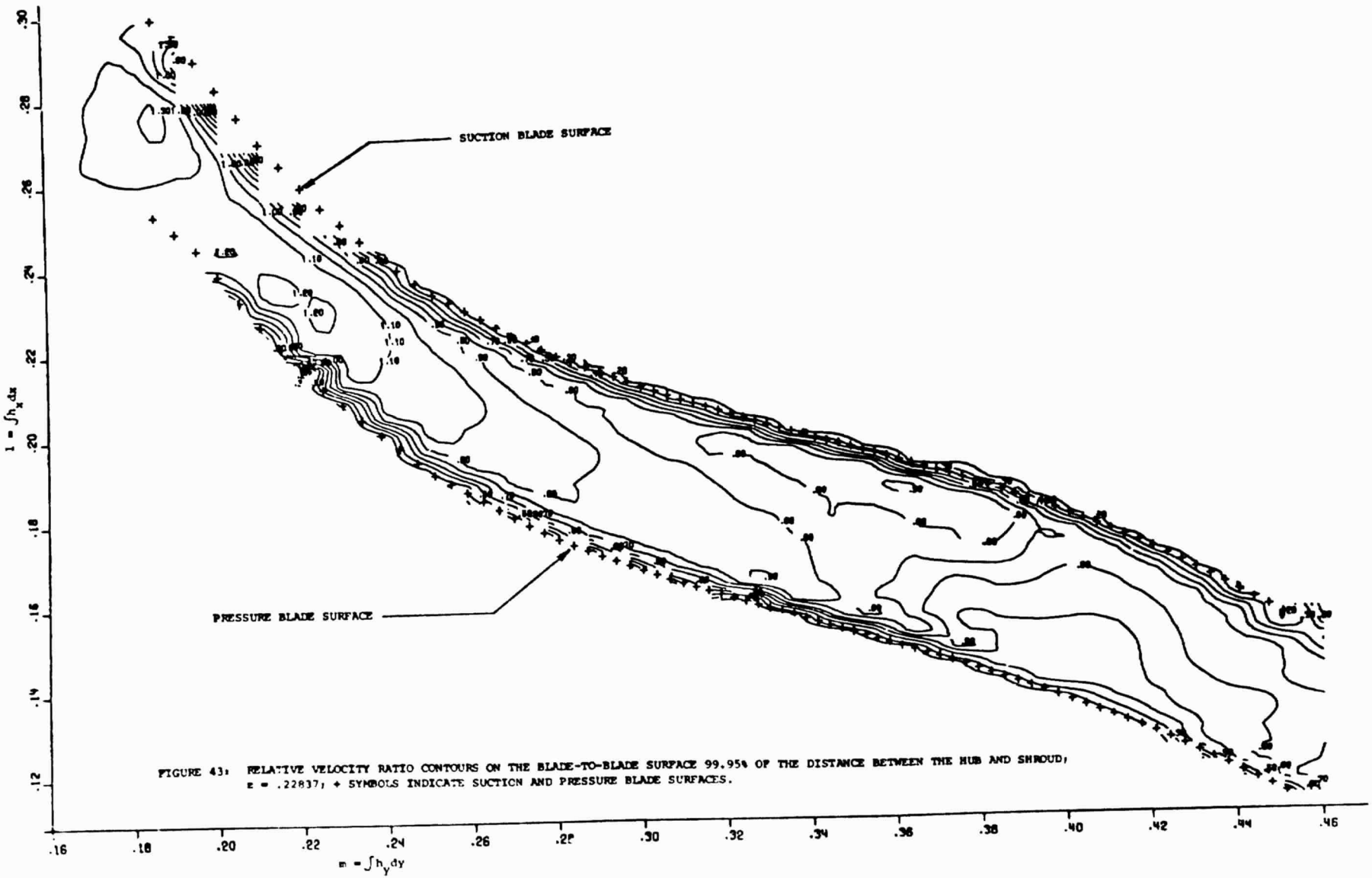

FIGURE 43: RELATIVE VELOCITY RATIO CONTOURS ON THE BLADE-TO-BLADE SURFACE 99.95% OF THE DISTANCE BETWEEN THE HUB AND SHROUD; ε = .22837; + SYMBOLS INDICATE SUCTION AND PRESSURE BLADE SURFACES.

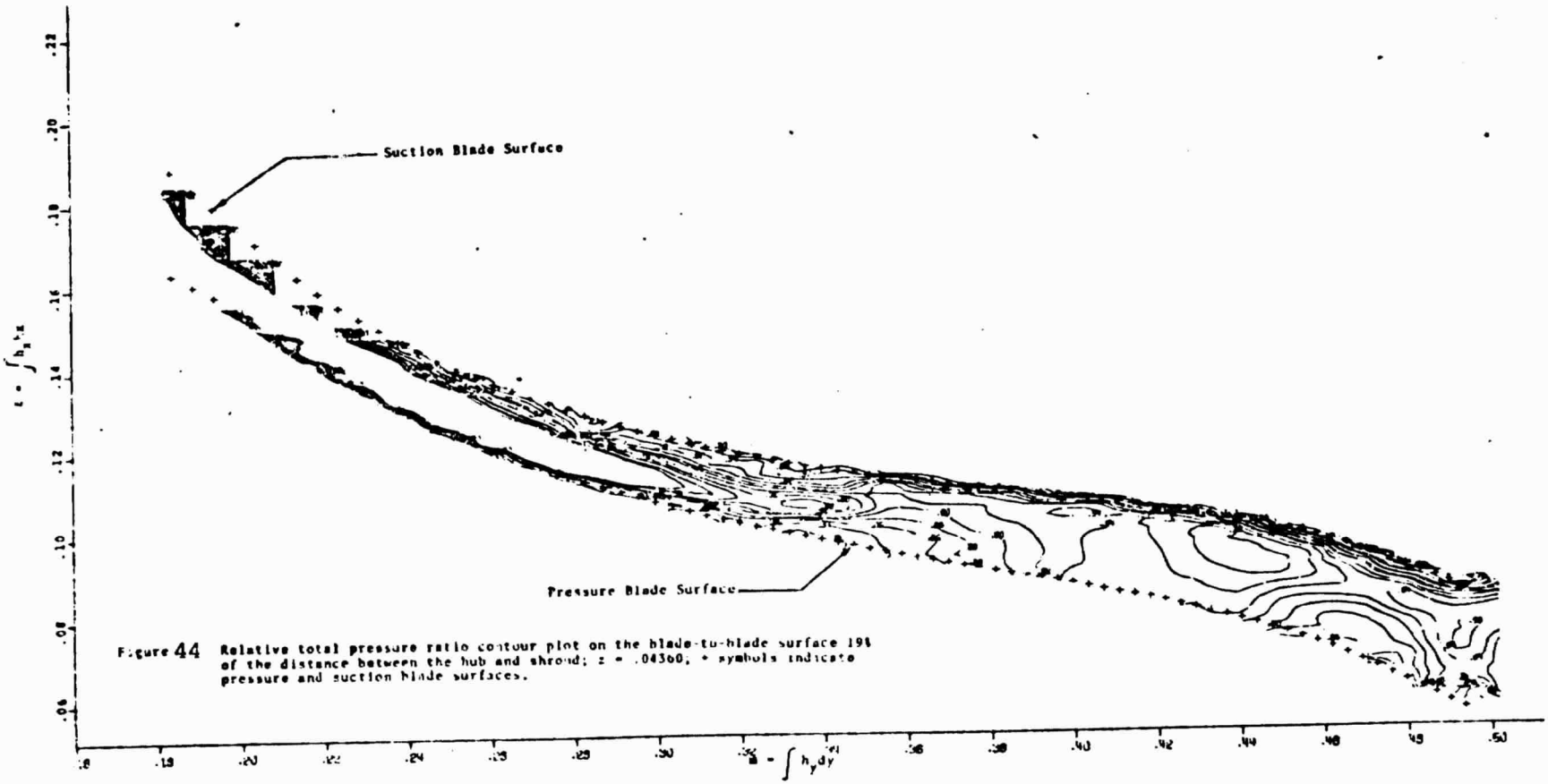

Figure 44 Relative total pressure ratio contour plot on the blade-to-blade surface 19% of the distance between the hub and shroud; z = .04360, + symbols indicate pressure and suction blade surfaces.

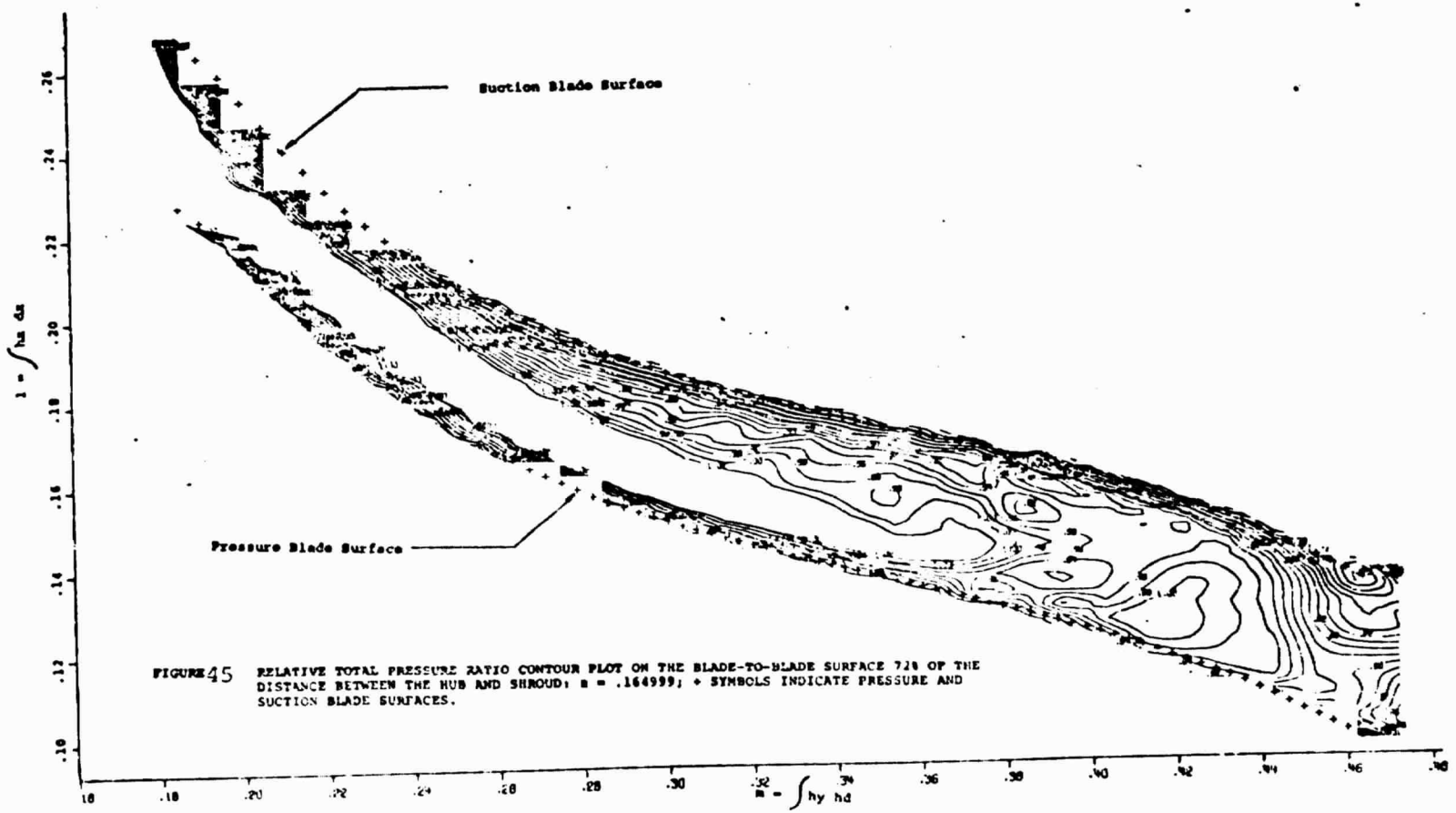

FIGURE 45 RELATIVE TOTAL PRESSURE RATIO CONTOUR PLOT ON THE BLADE-TO-BLADE SURFACE 72% OF THE DISTANCE BETWEEN THE HUB AND SHROUD; s = .164999; + SYMBOLS INDICATE PRESSURE AND SUCTION BLADE SURFACES.

ORIGINAL PAGE IS
OF POOR QUALITY

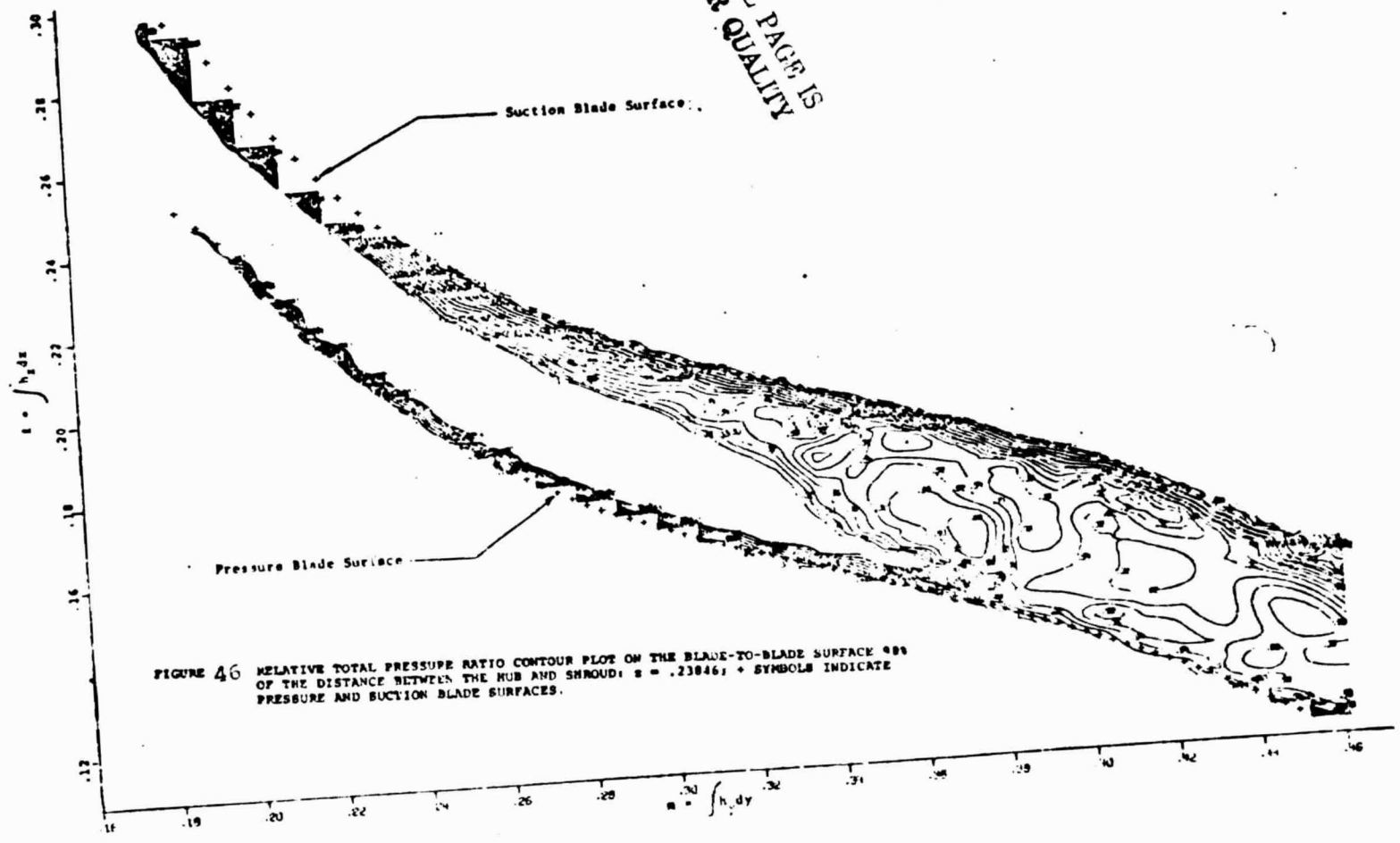

FIGURE 46 RELATIVE TOTAL PRESSURE RATIO CONTOUR PLOT ON THE BLADE-TO-BLADE SURFACE 98% OF THE DISTANCE BETWEEN THE HUB AND SHROUD; s = .23846; + SYMBOLS INDICATE PRESSURE AND SUCTION BLADE SURFACES.

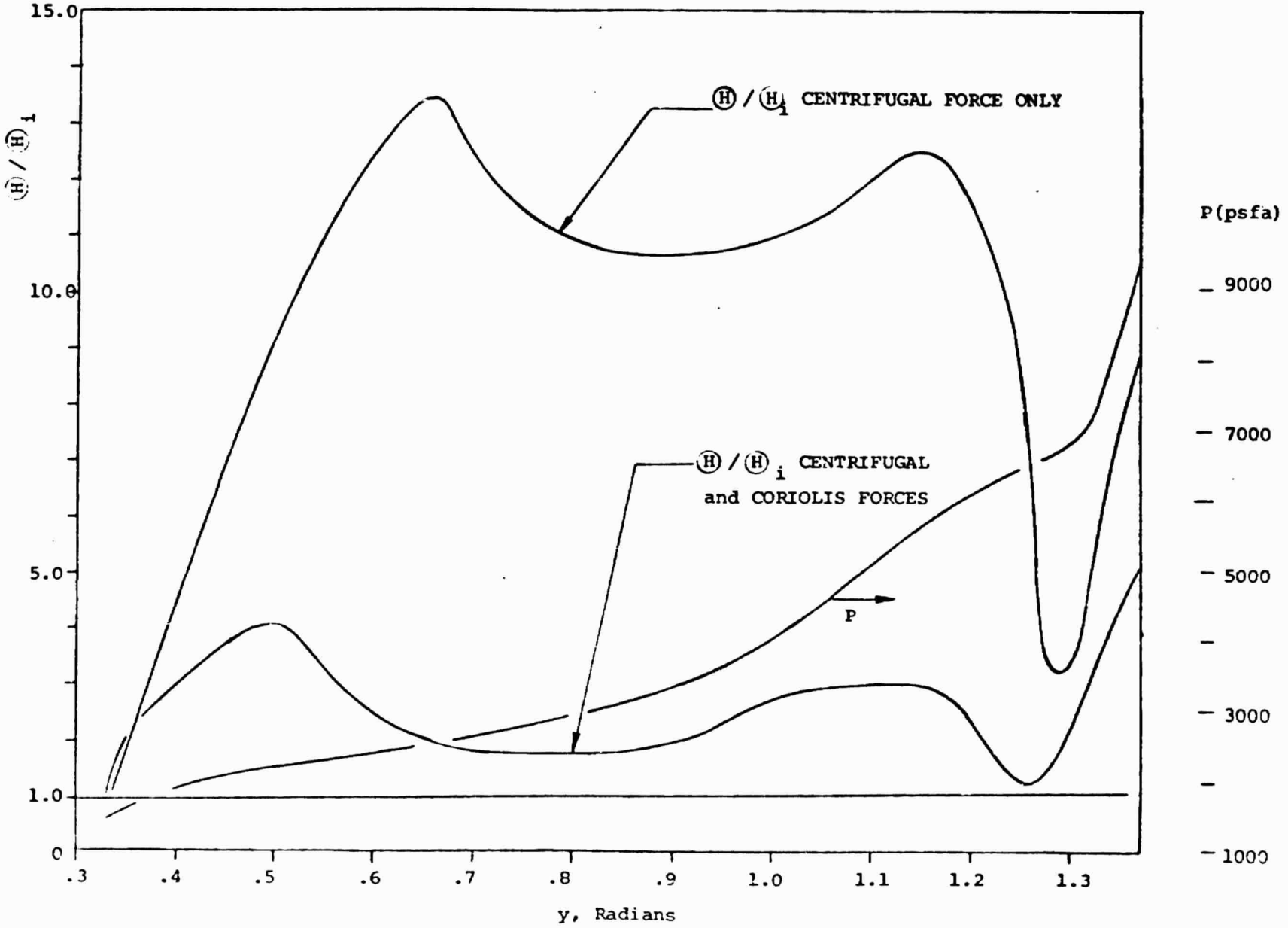

FIGURE 47: SUCTION BLADE MOMENTUM THICKNESS AND PRESSURE DISTRIBUTION ON A BLADE-TO-BLADE SURFACE 19% OF THE DISTANCE BETWEEN HUB AND SHROUD; z = .04360

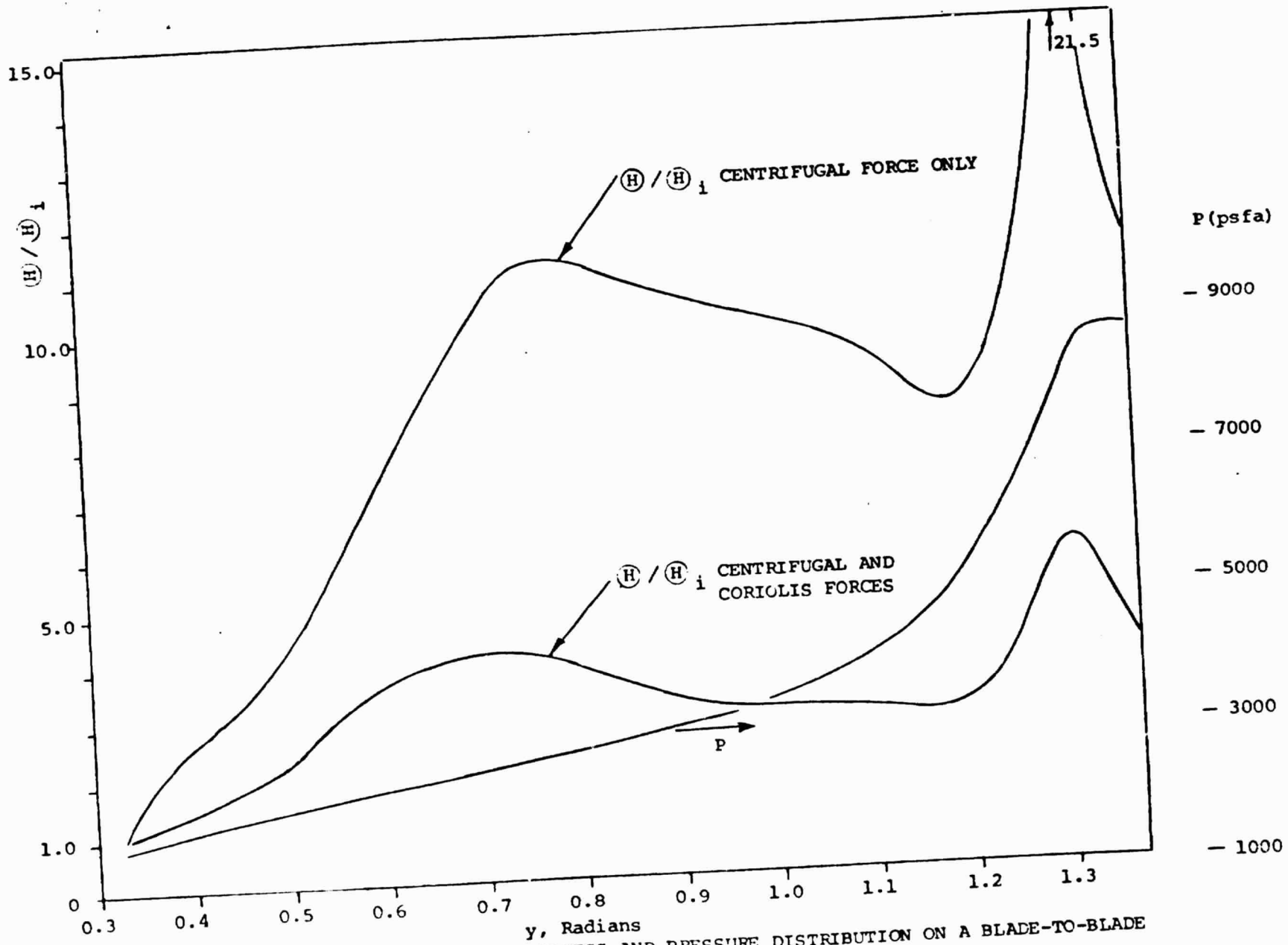

FIGURE 48: SUCTION BLADE MOMENTUM THICKNESS AND PRESSURE DISTRIBUTION ON A BLADE-TO-BLADE SURFACE [illegible] OF THE DISTANCE BETWEEN HUB AND SHROUD; z = .20230

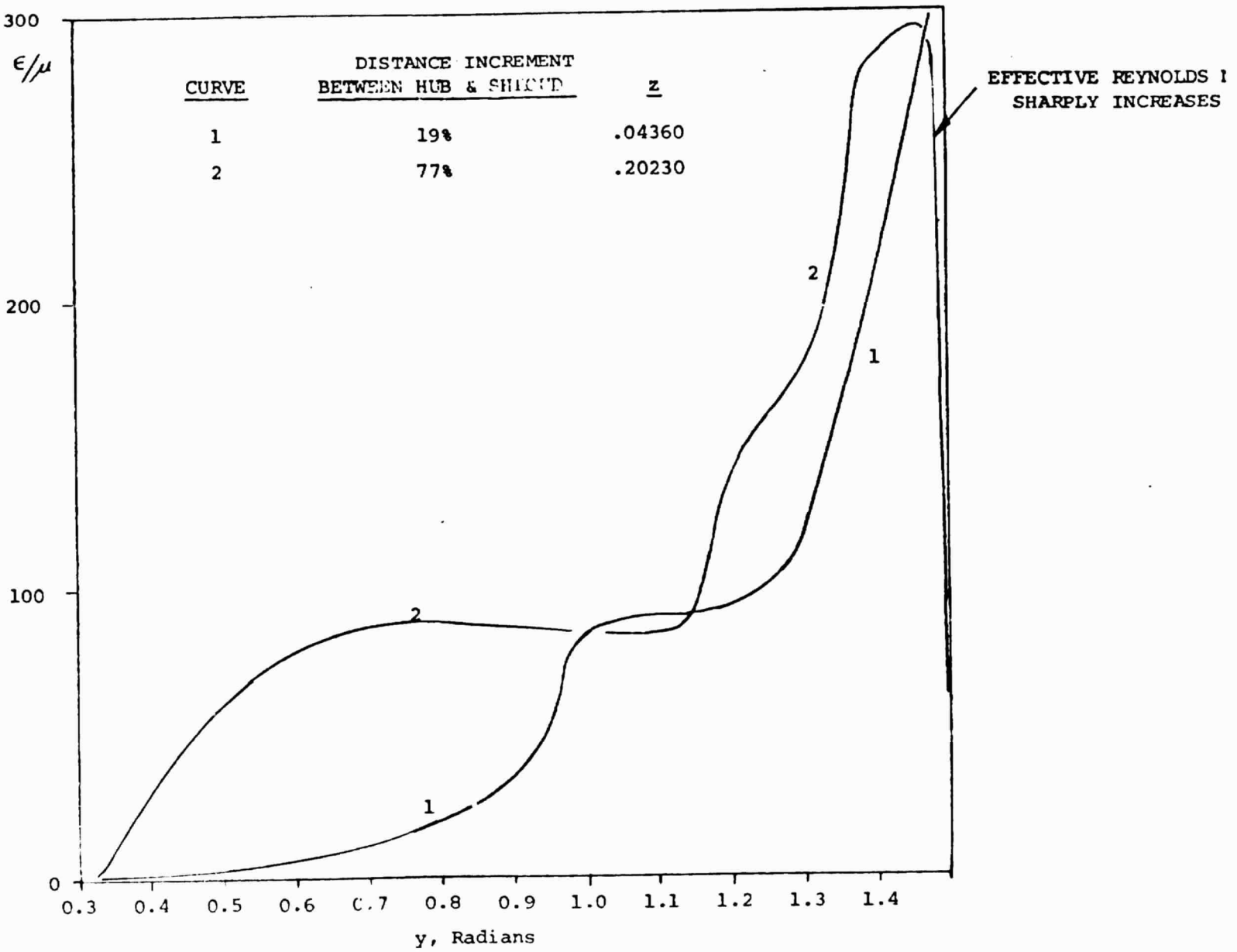

FIGURE 49: DISTRIBUTIONS OF THE RATIO OF EDDY VISCOSITY TO MOLECULAR VISCOSITY ALONG THE SUCTION BLADE SURFACE.

9.0 CONCLUDING REMARKS

A viscous blade-to-blade computer code for computing the flow field in centrifugal impellers has been sucessfully developed. The program was used to calculate the flow field of both a radial and backswept compressor impeller. Whereas the radial impeller problem indicated a large separation region on the suction blade surface near the discharge, the backswept impeller calculation, which included the mixing length turbulence model, did not separate. No conclusions can be drawn with regard to the effectiveness of backswept blading in reducing or eliminating flow separation, because the radial impeller was calculated for laminar flow at very low Reynolds number (5000), and the backswept impeller was calculated at a high Reynolds number (1.43×10^6) with the turbulence model included.

The backswept impeller problem requires 9.3 hours of computer time on the CDC 7600. It is recommended that an effort be made to improve calculation efficiency to reduce the costs associated with the blade-to-blade solution. Also, it is recommended that the IFFC code be modified to provide the additional capability of calculating the flow in cross-section computational planes. This modification will enable the program to calculate shroud viscous effects, tip clearance effects, and corner vortices.

10.0 REFERENCES

1. Trulio, J.G. and Walitt, L., "Numerical Calculations of Viscous Compressible Fluid Flow Around an Oscillating Rigid Cylinder", NASA CR-1467(1969)
2. Trulio, J.G. and Walitt, L., "Numerical Calculations of Viscous Compressible Fluid Flow Around a Stationary Cylinder", NASA CR-1465 (1970)
3. Trulio, J.G. , Walitt, L., and Niles, W.J. "Numerical Calculations of Viscous Compressible Fluid Flow Over a Flat Plate and Step Geometry", NASA CR-1466 (1970)
4. Walitt, L., "Numerical Studies of Supersonic Near Wakes". Ph.D. Dissertation, UCLA (1969)
5. Trulio, J.G., Walitt, L., and Liu, C.Y., "Numerical Calculations of Separated Flow", Proceedings of Symposium on Viscous Interaction Phenomea in Supersonic and Hypersonic Flow, 1969, Areospace Research Laboratories, University of Dayton Press
6. Walitt, L., Wilcox, D.C. and Liu, C.Y., "Numerical Study of Plume Induced Flow Separation", paper presented at the Symposium on Application of Computer to Fluid Dynamic Analysis and Design at Polytechnic Institute of Brooklyn Graduate Center, Farmingdale, Long Island, New York, (January 1967) to be published in the Journal Computer and Fluids.
7. Trulio, J.G., "Theory and Structure of the AFTON Codes," Air Force Weapons Laboratory Technical Report NO. AFWL-TR-66-19 (1966)
8. Hayes, W.D., "On Hypersonic Simulitude" Quarterly of Applied Mathematics, Vol. 5, pp 105-106 (1947)
9. Walitt, L., and Trulio, J.G., "A Numerical Method for Computing Three-Dimensional Viscous Supersonic Flow Fields About Slender Bodies". NASA CR-1963 (1971)
10. Kastanis, T., "Use of Abitary Quasi-Orthegonals for Calculating Flow Distribution in the Meridonal Plane of a Turbomachine", NASA TN D-2546 (1964)

10.0 CONTINUED

11. Kolmogorov, A.N., "Equations of Turbulent Motion of an Incompressible Fluid", Izv. Akad. Nauk SSR Seria Fizichiska, VI. NO. 1-2, P. 56 (1942)
12. Saffman, P.G., "A Model for Inhomogeneous Turbulent Flow", Proc. Roy Soc., A 317, P. 417 (1970)
13. Chou, P.Y. "On the Velocity Correlations and the Solution of the Equations of Turbulent Fluctuations", Q. Appl. Math, Vol 3, p. 38. (1945)
14. Harlow, F.H. and Nakayama, P.I., "Transport of Turbulent Energy Decay Rate", Los Alamos Sci. Lab., University of California, Rep. LA 3854 (1968)
15. Jones, W.P. and Launder, B.E., "The Prediction of Laminarization with 2 Equation Model of Turbulence", Int. J. Heat and Mass Transfer, Vol. 15, p. 301 (1972)
16. Ng. K.H. and Spalding, D.B., "Some Applications of a Model of Turbulence to Boundary Layer Near Walls", Phys. of Fluids, Vol. 15 (1972)
17. Wilcox, D.C., "Calculation of Turbulent Boundary-Layer Shock-Wave Interaction", AIAA J. Vol II, NO. 11 P 1592 (1973)
18. Prandtl, L., "Bericht Über Untersuchongen Zur Ausgebildeten Turbulenz", ZAMM, Vol. 5, p. 136 (1925)
19. Van Driest, E.R., "On Turbulent Flow Near a Wall", J. Aerospace Science, Vol. 23, No. 11, P. 1007 (1956)
20. Cebeci, T., "Calculation of Compressible Turbulent Boundary Layers with Heat and Mass Transfer", AIAA J., Vol 9., No. 6, p. 1091 (1971)
21. Klebanoff, P.S., "Characteristics of Turbulence in a Boundary Layer with Zero Pressure Gradiant", NACA TN 3178, July (1954)
22. Cebeci, T.,Smith, A.M.O., and Mosinskis, G., "Calculations of Compressible Adiabatic Turbulent Boundary Layers", AIAA J., Vol. 8, No. 11 P. 1974 (1970)
23. Cebeci, T.,Mosinskis, G.J., and Smith, A.M.O., "Calculation of Separation Points in Incompressible Turbulent Flows" J. of Aircraft, Vol. 9, p. 618 (1972)

10.0 CONTINUED

24. Cebeci, T., "Eddy-Viscosity Distribution in Thick Axisymmetric Turbulent Boundary Layers," J. Fluid Engr., Trans. ASME, p. 319, June (1973)

25. Cebeci, T., "Kinematic Eddy Viscosity at low Reynolds Numbers", AIAA J., Vol II. No. 1, P. 102 (1973)

26. Baldwin, B.S. and MacCormack, R.W., "Numerical Solution of the Interaction of a Strong Shock Wave with a Hypersonic Turbulent Boundary Layer", AIAA paper 74-558, AIAA 7th Fluid and Plasma Dynamics Conference, June (1974)

27. Launder, B.E., and Spalding, D.B., Lecture in Mathematical Models of Turbulence, Academic press, N.Y., (1972)

28. Proceedings of Computation of Turbulent Boundaries-1968, AFOSR-IFP-Stanford Conference, Stanford University (1969)

29. Thwaites, B., "On the Momentum Equation in Laminar Boundary Layer Flow. A New Method of Uniparametic Calculation", ARC R & M, 2587 (1952)

30. Stratford, B.S., "The Prediction of Separation of Turbulent Boundary Layers, J. Fluid Mech., Vol. 5, p.1 (1959)

31. McNally, W.D., "Fortan Program for Calculating Compressible Laminar and Turbulent Boundary Layers in Arbitary Pressure Gradients," NASA TN D-5681 (1970)

32. Von Neumann, J., and Richtmeyer, R.D., "A Method for the Numerical Calculation of Hydrodynamic Shocks", J. App. Phys., 21, 232 (1950)

33. Richtmeyer, R.D.,"Difference Methods for Initial Value Problems", Wiley (Interscience) N.Y. (1957)

34. Trulio, J.G., and Trigger, K., "Numerical Solution of the One Dimensional Hydrodynamic Equations", UCRL 6267 (1961)

35. Trulio, J.G., "The Strip Code and the Jetting of Gas Between Plates, Methods in Computational Physics, Edited by B. Alder, S. Fernbach, M. Rotenberg, Vol. 3, Acad. Press, N.Y., p. 69. (1964)

10.0 CONTINUED

36. Vanco, M.R., "Fortran Program for Calculating Velocities in the Meridional Plane of a Turbomachine", NASA TN D-6701 (1972)

37. Dean, R.C., Jr., "On the Unresolved Fluid Dynamics of the Centrifugal Compressor", Advanced Centrifugal Compressors ASME Publication, New York (1971)

38. Pai, S. Viscous Flow Theory, I-Laminar Flow , pp 28-31 and pp. 44-47, Van Nostrand (1956)

39. Katsanis, T., and McNally, W.D., "Fortran Program for Calculating Velocities and Streamlines on the Hub-Shroud Mid-Channel Flow Surface of an Axial or Mixed-Flow Turbomachine", NASA TN D-7343

40. Mager, A. "Generalization of Boundary-Layer Momentum Integral Equations to Three-Dimensional Flows Including Those of Rotating System" NACA TN 2310 (1951)

Appendix A

DEVELOPMENT OF EQUATIONS OF MOTION IN ROTATING ORTHOGONAL CURVILINEAR COORDINATES

The coordinate system upon which the iteration takes place controls convergence of the calculational procedure. Since flow is confined to an impeller blade channel, a generalized coordinate system, whose axis follows the channel geometry, will be utilized to converge the iteration as rapidly as possible. Consider the generalized coordinates (x,y,z) shown in Figure A1; the surface x = constant is a mid-channel surface, surface y = constant is a blade-to-blade surface, and the surface z = constant is an orthogonal channel surface. The transformation of cartesian equations in coordinates, X_1, X_2, X_3 to the generalized curvilinear coordinates x,y,z is presented in the following paragraphs. The development takes place in the following three steps:

(1) The metrics and generalized basis vectors are derived.

(2) Coriolis and centrifugal acceleration terms are developed in generalized coordinates.

(3) The generalized equations of motion are presented.

The rotating cartesian coordinates X_1, X_2, X_3 are related to the orthogonal generalized coordinates x, y, z as follows:

$$\left.\begin{aligned} X_1 &= f_1\ (x,y,z) \\ X_2 &= f_2\ (x,y,z) \\ X_3 &= f_3\ (x,y,z) \end{aligned}\right\} \qquad \text{(A1)}$$

The metrics and basis vectors of the transformation can be determined from Equations (A1). An element of a length, ds, in cartesian coordinates is expressed in generalized coordinates as follows:

$$ds^2 = h_x^2\ dx^2 + h_y^2\ dy^2 + h_z^2\ dz^2 \qquad \text{(A2)}$$

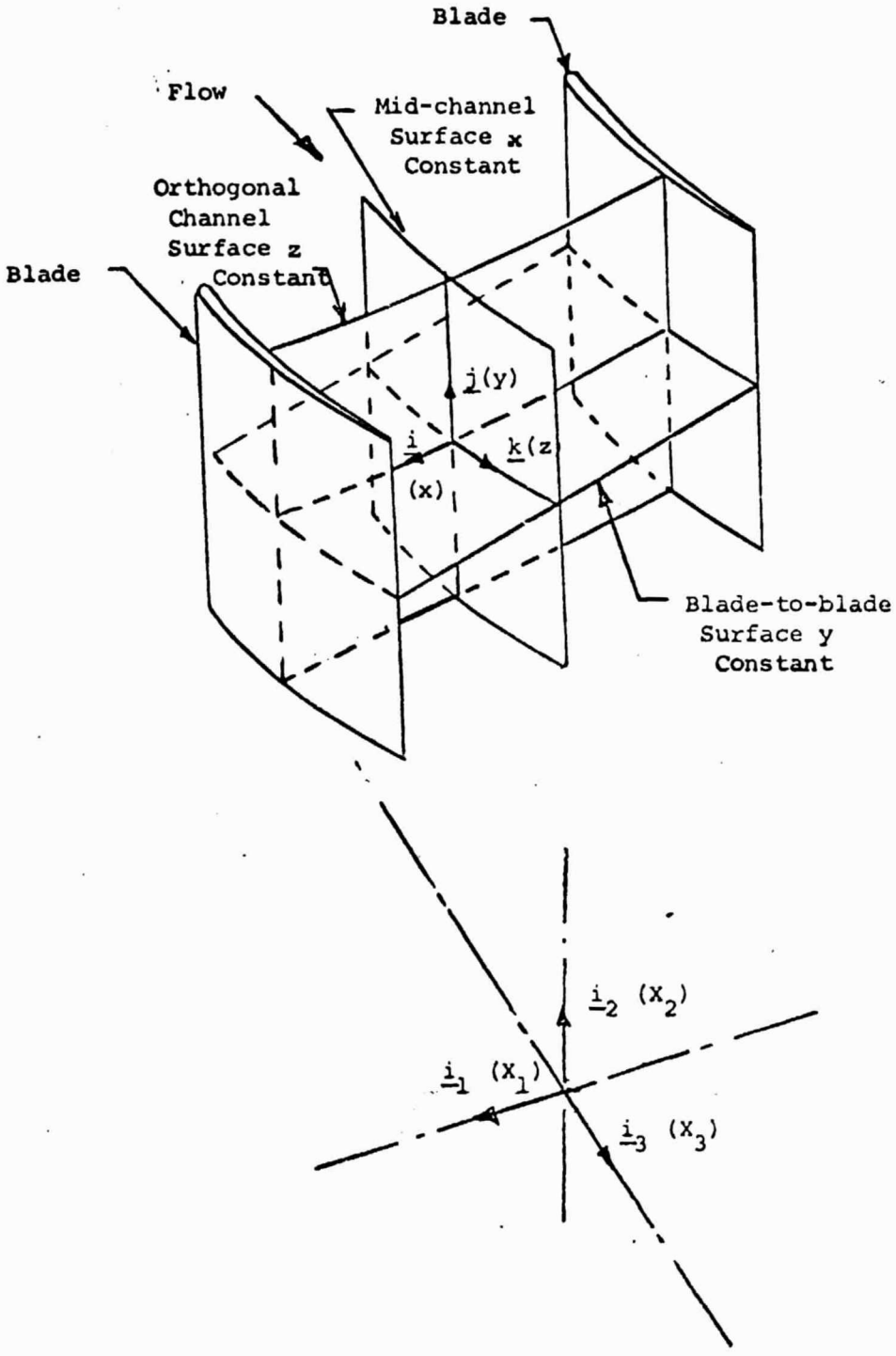

FIGURE A1: Orthogonal surfaces in the channel of a centrifugal impeller which define the curvilinear coordinates x, y, and z.

where: $h_x = \sqrt{\left(\frac{\partial X_1}{\partial x}\right)^2 + \left(\frac{\partial X_2}{\partial x}\right)^2 + \left(\frac{\partial X_3}{\partial x}\right)^2}$

$$h_2 = \sqrt{\left(\frac{\partial X_1}{\partial y}\right)^2 + \left(\frac{\partial X_2}{\partial y}\right)^2 + \left(\frac{\partial X_3}{\partial y}\right)^2}$$

$$h_z = \sqrt{\left(\frac{\partial X_1}{\partial z}\right)^2 + \left(\frac{\partial X_2}{\partial z}\right)^2 + \left(\frac{\partial X_3}{\partial z}\right)^2}$$

The parameters, h_x, h_y, and h_z are the metrics of the transformation. The unit basis vectors $\underline{i}$, $\underline{j}$, $\underline{k}$ of the generalized coordinates are related to the cartesian basis vectors $\underline{i}_1$, $\underline{i}_2$, and $\underline{i}_3$ as follows:

$$\left.\begin{aligned} \underline{i} &= h_x \left(\frac{\partial X}{\partial X_1} \underline{i}_1 + \frac{\partial X}{\partial X_2} \underline{i}_2 + \frac{\partial X}{\partial X_3} \underline{i}_3 \right) \\ \underline{j} &= h_y \left(\frac{\partial y}{\partial X_1} \underline{i}_1 + \frac{\partial y}{\partial X_2} \underline{i}_2 + \frac{\partial y}{\partial X_3} \underline{i}_3 \right) \\ \underline{k} &= h_z \left(\frac{\partial z}{\partial X_1} \underline{i}_1 + \frac{\partial z}{\partial X_2} \underline{i}_2 + \frac{\partial z}{\partial X_3} \underline{i}_3 \right) \end{aligned}\right\} \qquad \text{(A3)}$$

The Coriolis and centrifugal accelerations, in the directions, x,y and z can be determined from a scalar product of their cartesian components with the basis vectors of Equations (A3). The Coriolis accelerations in directions $\underline{i}$, $\underline{j}$, and $\underline{k}$, are, respectively

$$2(\underline{\omega} \times \underline{u}) \cdot \underline{i} = 2h_x \omega \left\{ v h_y \left(\frac{\partial x}{\partial x_2} \frac{\partial y}{\partial x_1} - \frac{\partial y}{\partial x_2} \frac{\partial x}{\partial x_1} \right) + w h_z \left(\frac{\partial x}{\partial x_2} \frac{\partial z}{\partial x_1} - \frac{\partial z}{\partial x_2} \frac{\partial x}{\partial x_1} \right) \right\} \qquad \text{(A4)}$$

$$2(\underline{\omega} \times \underline{u}) \cdot \underline{j} = 2h_y \omega \left\{ u h_x \left(\frac{\partial x}{\partial x_1} \frac{\partial y}{\partial x_2} - \frac{\partial y}{\partial x_1} \frac{\partial x}{\partial x_2} \right) + w h_z \left(\frac{\partial y}{\partial x_2} \frac{\partial z}{\partial x_1} - \frac{\partial y}{\partial x_1} \frac{\partial z}{\partial x_2} \right) \right\} \qquad \text{(A5)}$$

$$2(\underline{\omega} \times \underline{u}) \cdot \underline{k} = 2h_z \omega \left\{ u h_x \left(\frac{\partial z}{\partial x_2} \frac{\partial x}{\partial x_1} - \frac{\partial z}{\partial x_1} \frac{\partial x}{\partial x_2} \right) + v h_y \left(\frac{\partial z}{\partial x_2} \frac{\partial y}{\partial x_1} - \frac{\partial z}{\partial x_1} \frac{\partial y}{\partial x_2} \right) \right\} \qquad \text{(A6)}$$

where u, v, and w are the components of velocity vector $\underline{u}$ in the $\underline{i}$, $\underline{j}$, and $\underline{k}$ directions, respectively, ω is the angular frequency, and $\underline{\omega}$ is the angular frequency vector pointing in the X_3 direction.

The centrifugal accelerations in directions $\underline{i}$, $\underline{j}$, and $\underline{k}$, are, respectively

$$(\underline{\omega} \times \underline{\omega} \times \underline{r}) \cdot \underline{i} = -\omega^2 h_x \left(x_1 \frac{\partial x}{\partial x_1} + x_2 \frac{\partial x}{\partial x_2} \right) \tag{A7}$$

$$(\underline{\omega} \times \underline{\omega} \times \underline{r}) \cdot \underline{j} = -\omega^2 h_y \left(x_1 \frac{\partial y}{\partial x_1} + x_2 \frac{\partial y}{\partial x_2} \right) \tag{A8}$$

$$(\underline{\omega} \times \underline{\omega} \times \underline{r}) \cdot \underline{k} = -\omega^2 h_z \left(x_1 \frac{\partial z}{\partial x_1} + x_2 \frac{\partial z}{\partial x_2} \right) \tag{A9}$$

where $\underline{r}$ is the position vector in cartesian rotating coordinates X_1, X_2, and X_3.

The Coriolis and centrifugal acceleration components of Equations (A4) to (A9) are added to the Eulerian set of equations of motion in generalized orthogonal coordinates (Ref. 38). The final relations are as follows:

Continuity

$$\operatorname{div}(\rho \underline{u}) = 0 \tag{A10}$$

where:

$$\operatorname{div}(\rho \underline{u}) = \frac{1}{h_x h_y h_z} \left\{ \frac{\partial}{\partial x}(\rho u h_y h_z) + \frac{\partial}{\partial y}(\rho v h_z h_x) + \frac{\partial}{\partial z}(\rho w h_x h_y) \right\}$$

$$\underline{u} = u \underline{i} + v \underline{j} + w \underline{k}$$

and ρ is the density.

x - Momentum

$$\operatorname{div}(\rho u \underline{u}) + \frac{\rho u}{h_x}\left[\frac{u}{h_x}\frac{\partial h_x}{\partial x} + \frac{v}{h_y}\frac{\partial h_x}{\partial y} + \frac{w}{h_z}\frac{\partial h_x}{\partial z}\right] - \frac{\rho}{h_x}\left[\frac{u^2}{h_x}\frac{\partial h_x}{\partial x} + \frac{v^2}{h_y}\frac{\partial h_y}{\partial x} + \frac{w^2}{h_z}\frac{\partial h_z}{\partial x}\right] + 2 h_x \rho \omega \left[v h_y \left(\frac{\partial x}{\partial x_2}\frac{\partial z}{\partial x_1} - \frac{\partial z}{\partial x_2}\frac{\partial x}{\partial x_1} \right) + w h_z \left(\frac{\partial x}{\partial x_1}\frac{\partial z}{\partial x_1} - \frac{\partial z}{\partial x_2}\frac{\partial x}{\partial x_1} \right) \right] - \rho \omega^2 h_x \left[x_1 \frac{\partial x}{\partial x_1} + x_2 \frac{\partial x}{\partial x_2} \right] = \operatorname{div}(\underline{\underline{D}}_x) + \frac{\tau_{xy}}{h_x h_y}\frac{\partial h_y}{\partial x} + \frac{\tau_{zx}}{h_x h_z}\frac{\partial h_x}{\partial z} - \frac{\sigma_y}{h_y h_x}\frac{\partial h_y}{\partial x} - \frac{\sigma_z}{h_z h_x}\frac{\partial h_z}{\partial x} \tag{A11}$$

where:

$$\underline{\Phi}_x = \sigma_{xx}\,\underline{i} + \tau_{yx}\,\underline{j} + \tau_{zx}\,\underline{k}$$

y - Momentum

$$\mathrm{div}(\rho v \underline{U}) + \frac{\rho v}{h_y}\left[\frac{u}{h_x}\frac{\partial h_y}{\partial x} + \frac{v}{h_y}\frac{\partial h_y}{\partial y} + \frac{w}{h_z}\frac{\partial h_y}{\partial z}\right] - \frac{\rho}{h_y}\left[\frac{u^2}{h_x}\frac{\partial h_x}{\partial y} + \frac{v^2}{h_y}\frac{\partial h_y}{\partial y} + \frac{w^2}{h_z}\frac{\partial h_z}{\partial y}\right] + 2h_y\rho\omega\left[uh_x\left(\frac{\partial x}{\partial x_1}\frac{\partial y}{\partial x_2} - \frac{\partial y}{\partial x_1}\frac{\partial x}{\partial x_2}\right)\right.$$

$$\left. + wh_z\left(\frac{\partial y}{\partial x_1}\frac{\partial z}{\partial x_2} - \frac{\partial y}{\partial x_1}\frac{\partial z}{\partial x_2}\right)\right] - \rho\omega^2 h_y\left[x_1\frac{\partial y}{\partial x_1} + x_2\frac{\partial y}{\partial x_2}\right] = \mathrm{div}(\underline{\Phi}_y) + \frac{\tau_{yz}}{h_y h_z}\frac{\partial h_y}{\partial z} + \frac{\tau_{yy}}{h_y h_x}\frac{\partial h_y}{\partial x} - \frac{\tau_{zz}}{h_y h_z}\frac{\partial h_z}{\partial y} - \frac{\tau_{xx}}{h_x h_y}\frac{\partial h_x}{\partial y} \quad \text{(A12)}$$

where:

$$\underline{\Phi}_y = \tau_{xy}\,\underline{i} + \sigma_{yy}\,\underline{j} + \tau_{zy}\,\underline{k}$$

z - Momentum

$$\mathrm{div}(\rho w \underline{U}) + \frac{\rho w}{h_z}\left[\frac{u}{h_x}\frac{\partial h_z}{\partial x} + \frac{v}{h_y}\frac{\partial h_z}{\partial y} + \frac{w}{h_z}\frac{\partial h_z}{\partial z}\right] - \frac{\rho}{h_z}\left[\frac{u^2}{h_x}\frac{\partial h_x}{\partial z} + \frac{v^2}{h_y}\frac{\partial h_y}{\partial z} + \frac{w^2}{h_z}\frac{\partial h_z}{\partial z}\right] + 2h_z\rho\omega\left[uh_x\left(\frac{\partial x}{\partial x_1}\frac{\partial x}{\partial x_2} - \frac{\partial z}{\partial x_1}\frac{\partial x}{\partial x_2}\right)\right.$$

$$\left. + vh_y\left(\frac{\partial z}{\partial x_1}\frac{\partial y}{\partial x_2} - \frac{\partial z}{\partial x_1}\frac{\partial y}{\partial x_2}\right)\right] + \omega^2 h_z\rho\left(x_1\frac{\partial z}{\partial x_1} + x_2\frac{\partial z}{\partial x_2}\right) = \mathrm{div}(\underline{\Phi}_z) + \frac{\tau_{zx}}{h_x h_z}\frac{\partial h_z}{\partial x} + \frac{\tau_{yz}}{h_z h_y}\frac{\partial h_z}{\partial y} - \frac{\sigma_{xx}}{h_z h_x}\frac{\partial h_x}{\partial z} - \frac{\sigma_{yy}}{h_z h_y}\frac{\partial h_y}{\partial z} \quad \text{(A13)}$$

where:

$$\underline{\Phi}_z = \tau_{xz}\,\underline{i} + \tau_{yz}\,\underline{j} + \sigma_{zz}\,\underline{k}$$

Internal Energy Equation

$$\mathrm{div}(\rho E \underline{U}) = \sigma_{xx}\left[\frac{1}{h_x}\frac{\partial u}{\partial x} + \frac{v}{h_x h_y}\frac{\partial h_x}{\partial y} + \frac{w}{h_x h_z}\frac{\partial h_x}{\partial z}\right] + \sigma_{yy}\left[\frac{1}{h_y}\frac{\partial v}{\partial y} + \frac{w}{h_y h_z}\frac{\partial h_y}{\partial z} + \frac{u}{h_x h_y}\frac{\partial h_y}{\partial x}\right]$$

$$\sigma_{zz}\left[\frac{1}{h_z}\frac{\partial w}{\partial z} + \frac{u}{h_z h_x}\frac{\partial h_z}{\partial x} + \frac{v}{h_y h_z}\frac{\partial h_z}{\partial y}\right] + \tau_{yz}\left[\left(\frac{h_z}{h_y}\right)\frac{\partial}{\partial y}\left(\frac{w}{h_z}\right) + \left(\frac{h_y}{h_z}\right)\frac{\partial}{\partial z}\left(\frac{v}{h_y}\right)\right]$$

$$+ \tau_{zx}\left[\left(\frac{h_x}{h_z}\right)\frac{\partial}{\partial z}\left(\frac{u}{h_x}\right) + \left(\frac{h_z}{h_x}\right)\frac{\partial}{\partial x}\left(\frac{w}{h_z}\right)\right] + \tau_{xy}\left[\left(\frac{h_y}{h_x}\right)\frac{\partial}{\partial x}\left(\frac{v}{h_y}\right) + \left(\frac{h_x}{h_y}\right)\frac{\partial}{\partial y}\left(\frac{u}{h_x}\right)\right] \quad \text{(A14)}$$

where E is the specific internal energy, σ_{xx}, σ_{yy}, σ_{zz} are the normal stress components, and τ_{xy}, τ_{xz}, τ_{zy} are the shear stress components.

Appendix B

CONTINUITY EQUATION IN GENERALIZED COORDINATES

In this appendix continuity Equation (4), in (x,y,t) space, is transformed to generalized coordinates (ξ, η, τ). The transformation equations between x, y, t space and the generalized coordinates (ξ, η, τ) are presented, and from these relations the integral equation for mass conservation is derived.

Equation (4) is written in terms of the Eulerian coordinates (x,y,t). In the calculation the trace of the boundary of the impeller channel in the blade-to-blade surface must distort with time. Therefore, the continuity equation must be formulated in a generalized coordinate system ξ, η, τ. The generalized coordinates are defined as follows:

$$t = \tau \tag{B1}$$

$$x = f(\xi, \eta, \tau) \tag{B2}$$

$$y = g(\xi, \eta, \tau) \tag{B3}$$

and $f(\xi, \eta, 0) = \xi$, $g(\xi, \eta, 0) = \eta$, where $f_{\xi_{\tau=0}} = \left(\frac{\partial f}{\partial \xi}\right)_{\tau=0} = 1$, $g_{\eta_{t=0}} = \left(\frac{\partial g}{\partial \eta}\right)_{\tau=0} = 1$.

Equation (B1) is differentiated with respect to t, x, and y, respectively. The result is as follows:

$$\left.\begin{aligned} \frac{\partial \tau}{\partial t} &= 1 \\ \frac{\partial \tau}{\partial x} &= 0 \\ \frac{\partial \tau}{\partial y} &= 0 \end{aligned}\right\} \tag{B4}$$

Differentiation of Equations (B2) and (B3) results in the following:

$$\left.\begin{aligned} \frac{\partial \xi}{\partial \tau} &= \frac{f_\eta g_\tau - g_\eta f_\tau}{[f_\xi g_\eta - g_\xi f_\eta]} \\ \frac{\partial \xi}{\partial x} &= \frac{g_\eta}{[f_\xi g_\eta - g_\xi f_\eta]} \\ \frac{\partial \xi}{\partial y} &= \frac{-f_\eta}{[f_\xi g_\eta - g_\xi f_\eta]} \end{aligned}\right\} \tag{B5}$$

$$\left.\begin{aligned} \frac{\partial \tau}{\partial \tau} &= \frac{f_\tau g_\xi - f_\xi g_\tau}{[f_\xi g_\eta - g_\xi f_\eta]} \\ \frac{\partial \eta}{\partial x} &= \frac{-g_\xi}{[f_\xi g_\eta - g_\xi f_\eta]} \\ \frac{\partial \eta}{\partial y} &= \frac{f_\xi}{[f_\xi g_\eta - g_\xi f_\eta]} \end{aligned}\right\} \qquad \text{(B6)}$$

Consider the function $G(\xi, \eta, \tau)$. The derivatives of this function are as follows:

$$\frac{\partial G}{\partial t} = G_\xi \frac{\partial \xi}{\partial t} + G_\eta \frac{\partial \eta}{\partial t} + G_\tau \frac{\partial \tau}{\partial t} =$$

$$\frac{G_\xi(f_\eta g_\tau - g_\eta f_\tau) + G_\eta(f_\tau g_\xi - f_\xi g_\tau) + G_\tau(f_\xi g_\eta - g_\xi f_\eta)}{(f_\xi g_\eta - g_\xi f_\eta)} \qquad \text{(B7)}$$

$$\frac{\partial G}{\partial x} = G_\xi \frac{\partial \xi}{\partial x} + G_\eta \frac{\partial \eta}{\partial x} + G_\tau \frac{\partial \tau}{\partial x} = \frac{G_\xi g_\eta - G_\eta g_\xi}{[f_\xi g_\eta - g_\xi f_\eta]} \qquad \text{(B8)}$$

$$\frac{\partial G}{\partial y} = G_\xi \frac{\partial \xi}{\partial y} + G_\eta \frac{\partial \eta}{\partial y} + G_\tau \frac{\partial \tau}{\partial y} = \frac{-G_\xi f_\eta + G_\eta f_\xi}{[f_\xi g_\eta - g_\xi f_\eta]} \qquad \text{(B9)}$$

Equations (B3) - (B6) produced Equations (B7), (B8), and (B9).

Using Equations (B7), (B8), and (B9), the continuity Equation (4) is transformed to the generalized coordinates (ξ, η, τ). The transformed relation is as follows:

$$\frac{\partial}{\partial \tau}(\rho h_x h_y J^{-1}) + \left[(\rho h_y (u - S_x))_x + (\rho h_x (v - S_y))_y\right] J^{-1} - \frac{1}{U_\infty}\left[(\rho w' h_y S_x)_x + (\rho w' h_x S_\eta)_y\right] J^{-1}$$

$$= -\frac{1}{U_\infty}\frac{\partial}{\partial \tau}(\rho w' h_x h_y J^{-1}) \qquad \text{(B10)}$$

where $(\ )_x$ and $(\ )_y$ define differentiation with respect to x and y, respectively, and the grid velocity components S_x and S_y are defined in terms of deviatives of the curvilinear coordinates x and y.

$$S_x = \frac{\partial x}{\partial \tau} = f_\tau$$
$$S_y = \frac{\partial y}{\partial \tau} = g_\tau \qquad \text{(B11)}$$

The symbol J represents the Jacobian of the transformation, i.e.,

$$J = \left| \frac{\partial(\xi, \eta, \tau)}{\partial(x, y, t)} \right| = \frac{1}{f_\xi\, g_\eta - g_\xi\, f_\eta} \qquad \text{(B12)}$$

where: $$dx\, dy = J^{-1}\, d\xi\, d\eta \qquad \text{(B13)}$$

Equation (B10) is multiplied by the area increment $d\xi\ d\eta$ and the resultant relation is the final continuity equation as follows:

$$\frac{\partial}{\partial \tau}\int_A \rho h_x h_y dA + \int_C \rho(\underline{q}-\underline{q}_s)\cdot\hat{n}\, dC - \frac{1}{U_\infty}\int_C \rho w' \underline{q}_s \cdot \hat{\underline{n}}\, dC = -\frac{1}{U_\infty}\frac{\partial}{\partial \tau}\int_A \rho w' h_x h_y dA \qquad \text{(B14)}$$

where dA = dx dy, A corresponds to the area in the x,y plane contained within the region bounded by the closed curve C, $\hat{\underline{n}}$ is the unit normal to the curve C, $\underline{q}$ is the particle velocity vector in the (x,y) plane as defined by Equation (7), and $\underline{q}_s$ is the coordinate velocity vector in the (x,y) plane as defined by Equation (8). In the integration process use was made of Equation (B13) to convert integrals in $d\xi\ d\eta$ to integrals in dxdy. Furthermore, Leibniz's rule was used to permute differentiation and integration and Gauss's theorem was used to convert area integrals to line integrals in the (x,y) plane.